Review article

Thierry Taliercio* and Paolo Biagioni

Semiconductor infrared plasmonics

https://doi.org/10.1515/nanoph-2019-0077
Received March 7, 2019; revised April 18, 2019; accepted April 26, 2019

Abstract: The coupling between light and collective oscillations of free carriers at metallic surfaces and nanostructures is at the origin of one of the main fields of nanophotonics: plasmonics. The potential applications offered by plasmonics range from biosensing to solar cell technologies and from nonlinear optics at the nanoscale to light harvesting and extraction in nanophotonic devices. Heavily doped semiconductors are particularly appealing for the infrared spectral window due to their compatibility with microelectronic technologies, which paves the way toward their integration in low-cost, mass-fabricated devices. In addition, their plasma frequency can be tuned chemically, optically, or electrically over a broad spectral range. This review covers the optical properties of the heavily doped conventional semiconductors such as Ge, Si, or III–V alloys and how they can be successfully employed in plasmonics. The modeling of their specific optical properties and the technological processes to realize nanoantennas, slits, or metasurfaces are presented. We also provide an overview of the applications of this young field of research, mainly focusing on biosensing and active devices, among the most recent developments in semiconductor plasmonics. Finally, an outlook of further research directions and the potential technological transfer is presented.

Keywords: plasmonics; heavily doped semiconductors; infrared spectroscopy; nanoantennas; biosensing; active plasmonics.

1 Introduction

The subwavelength control of electromagnetic waves is one of the main challenges of modern science and technology. This requires sculpting the matter at the nanoscale and finding materials with the required optical properties. Metals are a particularly exciting material for optics. Indeed, metal surfaces and nanostructures sustain peculiar quasi-particles, the surface plasmon polaritons (SPPs), which are the result of the coupling between light and collective oscillations of free carriers. SPPs are among the building blocks of one of the main fields of nanophotonics: plasmonics. Plasmonic applications benefit from the extreme field confinement and enhancement that is associated with resonant charge oscillations and the development of this exciting field has relied mainly on Au so far. However, although Au has represented an excellent platform for the design and exploitation of plasmonic devices in the visible and near-infrared (IR) range of the spectrum, the recent extension of plasmonics to new spectral ranges has fostered the search for novel plasmonic materials with improved crystalline quality, integrability, tunability, and possibly lower losses [1].

The relevance of the spectral range spanning the terahertz (THz) [2] and mid-IR [3] frequencies is related to a broad range of potential applications such as high-speed wireless communication (from 0.1 to 10 THz) [4], medical sciences, chemical and biological sensing [5], homeland security, imaging [6–8], nondestructive evaluation [9], and quality control of food and agricultural products, among others. In particular, biosensing applications represent a crucial goal for IR plasmonics as, in this spectral range, molecular and macromolecular vibrations occur, with THz frequencies allowing one to access the overall molecular conformation and mid-IR frequencies addressing the so-called “molecular fingerprint”, which is associated with the resonant excitation of individual bond vibrations.

In this framework, heavily doped semiconductors represent a promising alternative to metals, as their plasma frequency (i.e. the frequency marking the onset of “metallic” behavior) can be controlled by doping and/or carrier injection to cover the IR region; therefore, they represent a class of tunable, high-quality materials for plasmonics. In addition, crystalline group-IV and III–V materials benefit from fabrication technologies that have been developed over the last 50 years by the microelectronics industry, which paves the way toward their integration in low-cost, mass-fabricated devices.

***Corresponding author: Thierry Taliercio,** Institute of Electronics and Systems, University of Montpellier, Montpellier, France, e-mail: thierry.taliercio@umontpellier.fr. https://orcid.org/0000-0002-6425-9981
Paolo Biagioni: Department of Physics, Politecnico di Milano, 20133 Milano, Italy

In this review, we do not address the case of plasmonics in noncrystalline materials, 2D materials, and nanocrystals, which are still relatively far from the possibility of integration on devices in the context of mass production. We invite the readers to refer to the excellent available literature if they are interested in the plasmonic properties of 2D semiconductors [10], graphene [11–19], semiconductor nanowires [20], and semiconductor nanocrystals [21–23]. The specific case of phonon-polaritons, which allow for a plasmon-like behavior in the mid-IR, will also not be thoroughly discussed because they intrinsically lack tunability, even if they present certain advantages, notably the low internal losses [24–27]. We will focus instead on the optical properties of the heavily doped conventional semiconductors such as Ge, Si, or III–V alloys because of the already established crucial role that they play in integrated optical devices and then discuss how they can be successfully employed in plasmonics and integrated on a Si platform [28].

The review is organized into three main parts. Section 2 addresses the fundamental building blocks to develop semiconductor plasmonics, the growth techniques, and the technological processes. Section 3 is dedicated to the optical properties of semiconductor nanoantennas. The modeling of their specific optical properties and how to characterize bulk material and nanoantennas are presented. Particular attention is paid to the analysis of losses, and in this context, we will argue that it is not always easy to make a fair comparison between heavily doped semiconductors and standard metals, as many different factors need to be considered. In the last section, we provide an overview of the applications of this fledgling field of research, mainly focusing on biosensing and active devices, among the most recent developments in semiconductor plasmonics. The exploitation of the specific structural and optical properties offers the possibility to address recent fields of research such as nonlinear optical conversion, hyperbolic media, perfect absorbers, and intersubband plasmons, among others. Finally, an outlook of further research directions and the potential technological transfer is presented.

Throughout the manuscript, we will make often use of wavelengths to define a specific range in the electromagnetic spectrum as common within the nano-optics and plasmonics community. However, the reader should be aware that, in the framework of IR spectroscopies, frequencies or wavenumbers are often preferred to wavelengths, with e.g. 1 THz corresponding to about 300 μm or 33 cm^{-1} and 30 THz to about 10 μm or 1000 cm^{-1}.

During the preparation of the review, we obviously had to make our own choices about the topics that should be included in it. This reflects, of course, the natural inclination and the background knowledge of the authors and inevitably makes the work partial. However, we hope that it can still represent a valuable source to foster novel ideas, new collaborations, and perspective technological transfers in the emerging field of semiconductor plasmonics.

2 Heavily doped semiconductors: growth, doping, and nanofabrication

The main evolutionary steps of humankind have been accompanied by the development and control of new materials. If with the Bronze Age, 5000 years ago, men made a significant step forward and learned how to build advanced tools, microelectronics was one of the greatest advances of the last century. The mastery of Si purification and growth techniques led in 1954 to the demonstration of the first Si transistor, paving the way for all the recent developments in semiconductor technology. Profiting from these advances, III–V semiconductor substrates of high crystalline quality and large size were also developed, featuring a low density of point defects and highly monitored doping levels, which is a prerequisite for any high-performance device.

An even higher degree of material control and new growth techniques were required to efficiently exploit quantum effects in electronic and optoelectronic devices, such as high electron mobility transistors [29], quantum cascade lasers [30], and superlattice detectors [31]. To this aim, novel epitaxy techniques were developed to grow single-crystal layers on single-crystal substrates. The most convenient ones for mass production are the chemical vapor deposition (CVD) techniques [32], first developed in the 1960s for Si [33], which are based on the pyrolysis reaction of chemical precursors at the substrate surface. In standard CVD techniques, the precursors are in the gaseous phase and the thermal energy required for the pyrolysis reaction is provided by the substrate temperature, which therefore controls both the growth speed (through thermal-assisted precursor dissociation) and the quality of the growth process (through temperature-dependent surface diffusion coefficients). Group IV materials and their alloys can typically be grown by standard CVD techniques. In this respect, however, low-energy plasma-enhanced CVD (LEPECVD) has emerged over the last two decades as a variant in which a low-energy plasma adds a further degree of freedom to the growth process, allowing one to independently control the dissociation

of the precursor and to perform the growth at lower temperatures [34, 35]. LEPECVD techniques provide high-rate, high-quality epitaxial growth of group IV materials that is especially crucial in mid-IR plasmonics, where the typical required thicknesses for antennas and devices are of the order of 100s of nanometers. Finally, the CVD growth of III–V and II–VI alloys typically employs metal-organic liquid precursors that are brought into the gas phase by bubbling a carrier gas that transports the precursor vapor into the reactor chamber. This metal-organic CVD is also often referred to as vapor phase epitaxy (VPE).

Another important growth technique for semiconductors, which is, however, mainly employed in laboratory research because it typically requires ultrahigh vacuum conditions, is molecular beam epitaxy (MBE) [36, 37]. Unlike CVD and VPE, the target materials in an MBE reactor are heated, sublimated, and physically deposited as molecular or atomic beams directly onto the sample surface with no chemical dissociation of precursors. This is why MBE achieves a high degree of purity and is a particularly well-adapted growth technique to precisely control the thickness and composition of the epitaxial films.

The advances brought by all these techniques have led to the realization of extremely complex devices [29–31], notably in terms of low-loss materials even with high doping levels and with a thickness control down to the single atomic layer (which is often needed, for example, for quantum cascade lasers, distributed Bragg reflectors, or multiple quantum well structures).

The same issues of material quality, thickness control, and doping levels are also addressed, although with application-specific requirements, in semiconductor plasmonics. The precise control of the film thickness does not represent a limiting factor here, because, as discussed before, the typical thickness of a standard heavily doped antenna is 100 of nanometers and the associated operating wavelengths are on the micrometer scale. In this respect, the most demanding proposals in the literature are probably those related to semiconductor hyperbolic metamaterials [38, 39], for which, however, an accuracy at the nanometer level is enough and can be obtained with standard epitaxy techniques. The achievement of a high doping level, in contrast, is crucial to operate semiconductor plasmonic devices over the whole mid-IR spectral range, which requires carrier densities in the 10^{20} cm^{-3} range. From this point of view, two different issues are faced when growing the active semiconductor layer, as one must be able to both incorporate a large density of dopants and fully activate them to render the free carrier density as close as possible to the dopant density. In CVD- and MBE-related techniques, besides the flux of the dopants, the substrate temperature and the growth rate are crucial parameters that can be controlled to tune the dopant incorporation rate also to above the solubility limit by working off equilibrium. However, despite the achieved incorporation, only the dopants that are placed in substitutional positions inside the crystal can actively contribute to the carrier density, whereas interstitial collocations usually prevent the dopants from being ionized. Also, nonsubstitutional dopants tend to cluster, which is, for example, a common occurrence in close proximity of dislocations and crystal defects in general, an event that further inhibits their activation. For these reasons, it is a common occurrence that, in the as-grown materials with dopant incorporations in the 10^{20} cm^{-3} range, the density of dopant atoms (as measured, for example, by means of secondary ion mass spectrometry) is larger than the active carrier density (which can be extracted from Hall-bar measurements or by means of IR spectroscopy). Typically, postgrowth annealing procedures are therefore applied to favor the establishment of a more ordered lattice with low losses and achieve a higher activation for the dopants. This is, of course, a critical step during which the dopant density might even decrease due to desorption and therefore requires careful optimization. Rapid thermal annealing, flash-lamp annealing, and laser annealing techniques have all been successfully exploited to this aim [40–43]. It should also be mentioned here that the use of surfactants in the growth chamber has also been proposed as a means to achieve high-quality structural and electronic properties [44–46].

When targeting extremely high doping levels for mid-IR plasmonics, many different effects that will limit the ultimate plasma frequency need to be taken into account. First of all, the nonparabolicity of the conduction band comes into play for very high carrier densities [47–50]. This results in an increased effective mass for the conduction population and, accordingly, in a reduced plasma frequency for a given carrier concentration. Also, when the growth occurs close to thermodynamic equilibrium, the density of the incorporated dopant atoms is limited by their solubility in the host semiconductor matrix. For example, depending on the temperature, typical solubility limits are reported between 10^{19} and 10^{21} cm^{-3} for P atoms in Si and Ge [51, 52] and between 10^{18} and 10^{20} cm^{-3} for Si in GaAs [53], with an increasing solubility for increasing temperature. However, it should be noted here that incorporation levels above the thermodynamic solubility limit can be reached since, as already mentioned, the growth often proceeds outside the conditions of thermodynamic equilibrium. Besides the achievement of a high dopant incorporation in the semiconductor,

a relevant issue is that the associated defect must be ionized, which requires that its transition energy level is not too deep and that no other competing and nonionizable defects are formed [54]. For Ge doping, for example, a reduced fraction of activated (i.e. ionized) dopants can be related to the presence of negatively charged vacancies that pair with the dopant atoms. Their concentration increases with the electron density due to a lower formation energy when the Fermi level moves closer into the conduction band [55]. In III–V compound semiconductors, in contrast, a dominant limiting effect is the one related to the amphoteric nature of dopants, i.e. to the dependence of their donor/acceptor behavior on the substitutional site. As the n-type doping level increases, the Fermi level moves into the conduction band and the formation of the amphoteric defect is reduced, leading to the so-called autocompensation [56]. Moreover, a detailed analysis of the doping levels under high incorporation conditions must take into account other effects, such as those related to lattice deformations (and associated shifts of the band structure), whose origin can be linked either with hydrostatic effects due to the different atomic radii or with electronic-induced deformations in which the increased charge population modifies the bond lengths [47, 48, 57]. It has also been suggested that, by proper engineering of the dopant-related distortions, one might achieve strain-enhanced doping in semiconductors [58]. Finally, a high doping level can determine a tail in the conduction band and the formation of an impurity band within the gap, which can have a relevant impact on the distribution of the carriers and on their effective mass.

The growth of the semiconductor film is followed by the nanofabrication of antennas, slits, and metasurfaces. In the field of semiconductor technologies, this is traditionally obtained with electron-beam lithography (EBL) [59–61] or optical lithography [62–65] techniques, that is, by exposing a polymer resist spun onto the wafer to a focused beam of photons [with wavelengths in the ultraviolet (UV) part of the electromagnetic spectrum] or of electrons (with typical energies in the 30–100 keV range). This is followed by the development of the imprinted resist by means of wet chemistry. As all the techniques described so far for the growth of high-quality doped semiconductor films imply epitaxy, the growth needs to be performed directly onto clean single-crystal substrates. Although localized growth exists [66], this limits the possibility of employing lift-off processes for the definition of the nanostructures, which is one of the most common routes in metal-based plasmonics. Instead, based on the type of material to be eroded, either wet etching or reactive ion etching techniques are used, the latter being a standard dry etching procedure in foundry processes where a reactive plasma creates high-energy ions that erode the semiconductor. Eventually, the resist mask layer is also removed with another wet etching step. EBL, being based on the scanning of a focused electron beam, is costly and time-consuming; however, it allows for the definition of patterns down to the nanometer scale. UV optical lithography, in contrast, suffers from a diffraction-limited resolution (depending on the wavelength employed) but requires only one time-consuming step for the preparation of the mask, which can then be used for mass production employing a large-area and low-cost exposure process. Although, for visible and near-IR plasmonics, optical lithographies are not an option due to their poor resolution, they become an available alternative to EBL for many semiconductor mid-IR devices that often do not require a spatial definition much below 50–100 nm.

Besides EBL and optical lithography, other nanofabrication techniques have been used in the literature, although less extensively, for the fabrication of plasmonic semiconductor nanostructures. Focused ion beam (FIB) techniques have been largely employed for Au-based plasmonics, especially with single-crystal films [67], and are based on the localized erosion of the sample atoms by a focused beam of accelerated ions (typically Ga ions). In the field of semiconductor mid-IR plasmonics, FIB milling was, for example, applied for the realization of Ge bow-tie antennas [68]. Also, a low-cost alternative to standard lithography techniques is represented by the so-called nanosphere lithography, in which a closely packed monolayer of polymer nanospheres is deposited onto the sample surface and acts as the mask for deposition and/or etching. Nanosphere lithography was, for example, employed to create a high-density array of InAs nanopillars for sensing applications [69]. Finally, it should be noted that there has been some interest in using direct ion implantation of dopants to define specific geometries by creating lateral patterning of mid-IR semiconductor surfaces [70, 71]. A representative image gallery, featuring several antenna geometries realized with different materials and different fabrication techniques, is presented in Figure 1.

3 Optical properties of semiconductor nanoantennas: modeling and experiments

In this section, we will review the basic understanding and modeling of the optical response of heavily doped

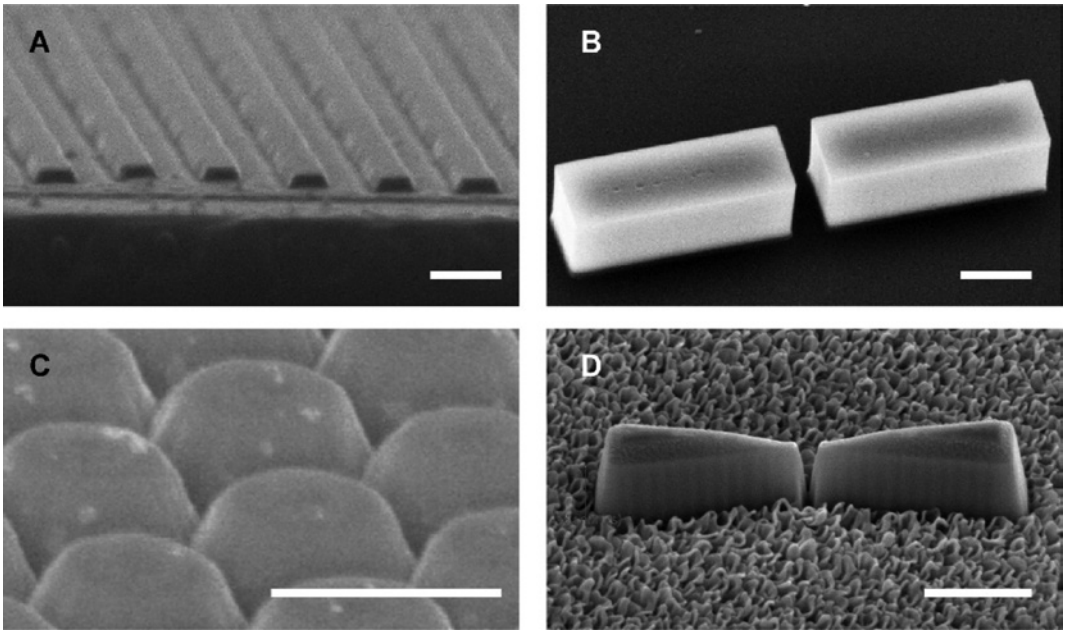

Figure 1: Nanofabrication of semiconductor plasmonic antennas.
(A) InAsSb gratings fabricated by optical lithography (courtesy from F. Barho), (B) Ge gap antenna fabricated by EBL [60], (C) InAs islands fabricated by nanosphere lithography [69], and (D) Ge bow-tie antenna fabricated by FIB milling [68]. All scale bars are 500 nm (C), reprinted from [69] with permission, Copyright 2013 American Chemical Society.

semiconductors together with the techniques available for their characterization. We will focus on both bulk materials/thin films and nanostructured systems. A special attention will be paid to the crucial issue of losses that hamper the plasmonic response.

3.1 Optical response of doped semiconductors

The response of a doped semiconductor to IR radiation can be modeled with a simplified approach that takes three main ingredients into account: (i) the presence of the plasma of electrons in the conduction band as determined mainly by the doping level; (ii) the material absorption related, for example, to the excitation of optical phonons or to interband transitions; and (iii) the presence of a dielectric background of polarization that is generated by the tails of all the high-frequency excitations in the material. Let us now consider the three contributions separately.

The conduction electrons can be to a first approximation modeled as a Drude plasma, with an associated dielectric constant that takes the restoring force exerted by the nuclei into account:

$$\varepsilon_{\text{Drude}}(\omega) = 1 - \frac{\omega_{\text{p}}^2}{\omega^2 + i\gamma\omega},$$

where γ is the damping constant associated with the conduction electron oscillations and ω_{p} is the plasma frequency, i.e. the frequency for which, in the limit of low damping, $\varepsilon_{\text{Drude}}(\omega) \cong 0$.

The presence of absorption lines can be described with a set of Lorentz oscillators, whose dielectric function takes the form:

$$\varepsilon_{\text{Lorentz}}(\omega) = 1 + \frac{\tilde{\omega}_{\text{p}}^2}{(\omega_0^2 - \omega^2) - i\tilde{\gamma}\omega},$$

where $\tilde{\omega}_{\text{p}}$ and $\tilde{\gamma}$ are the parameters associated with the strength and damping of the oscillator, respectively, whereas ω_0 is the resonance frequency. In mid-IR, such absorption processes are often related to optical phonons, whose creation is allowed by dipolar selection rules only in polar semiconductors such as III–V and II–VI compounds. In these materials, the energy of the absorption phonon bands limits therefore the IR transparency window of the intrinsic material and the associated losses are detrimental for plasmonic applications as well. In elemental group IV semiconductors such as Si and Ge, in contrast, such phonon transitions are forbidden in the dipolar approximation. However, local crystal defects (impurities, vacancies, dislocations, etc.) can weaken the selection rules and make such phonon excitations partially allowed. This is the main reason, for example, for the nonnegligible absorption

of standard Si wafers above a wavelength of about 9 μm, a spectral region for which Ge and GeSn alloys represent instead a valid alternative [3]. Another relevant absorption channel, which is specific to p-doped semiconductors in the IR, is represented by interband transitions between the different valence bands around the Γ point of the Brillouin zone. Such transitions are not fully inhibited by the dipolar selection rules because of the mixed sp character of the valence bands away from Γ. In Ge, for example, the transitions from the split-off band to the heavy- or light-hole bands prevent the use of p-doped materials for IR plasmonics due to the large losses [35].

It should also be noted here, while still discussing interband transitions, that the promotion of electrons from the valence band to the conduction band through the optical gap of the crystal, mediated by the absorption of higher-energy photons in the visible or near-IR spectral range, does not significantly impact the losses in the mid-IR range. However, all the high-energy transitions contribute a polarization background that adds up to the real part of the dielectric function in the form of a constant offset. Putting all the contributions together, the complete model for the Drude-Lorentz dielectric function of a heavily doped semiconductor therefore reads:

$$\varepsilon(\omega)=\varepsilon_{\infty}-\frac{\omega_{\mathrm{p}}^{2}}{\omega^{2}+i\gamma\omega}+\sum_{i}\frac{\tilde{\omega}_{\mathrm{p,i}}^{2}}{(\omega_{0,i}^{2}-\omega^{2})-i\tilde{\gamma}_{i}\omega},$$

where ε_{∞} is a real positive number and the sum runs over all the oscillators required for a comprehensive description of the transition losses in each specific material.

To a first approximation, if the heavily doped semiconductor is employed in a spectral region far away from allowed optical transitions (interband absorption or optical phonons), the Lorentz summation can be neglected and the material response can be described with the Drude term and the ε_{∞} offset only:

$$\varepsilon(\omega)\cong\varepsilon_{\infty}-\frac{\omega_{\mathrm{p}}^{2}}{\omega^{2}+i\gamma\omega}.$$

Although this represents already a good description of the plasma and is indeed successfully used in most fitting procedures to describe the IR response of heavily doped semiconductors [13, 40, 62, 63, 72, 73], it should be noted here that it also relies on the assumption that the electron losses (i.e. the damping parameter γ) are not dependent on frequency, which is generally not true. A more sophisticated approach relies on the use of Kramers-Kronig relations to describe a modified Drude-like response in which the electron scattering rate is indeed frequency dependent. In the case of heavily doped Ge, for example, it has been demonstrated experimentally that the frequency dependence is dominated by the scattering of the conduction electrons with optical phonons and charged impurities and increases almost linearly with frequency [35].

By inspecting the last equation, it is also apparent that the condition $\mathrm{Re}[\varepsilon(\omega)]=0$ here is not met at the plasma frequency ω_{p} but rather for a so-called "screened" plasma frequency that we define as

$$\omega^{*}=\sqrt{\frac{\omega_{\mathrm{p}}^{2}}{\varepsilon_{\infty}}-\gamma^{2}}.$$

Finally, it should be noted that the fact that the screened plasma frequency of n-type semiconductors is located far below the energy onset of interband transitions between the valence and conduction bands creates the conditions for the straightforward exploitation of epsilon-near-zero (ENZ) phenomena, as the spectral region in which $\mathrm{Re}[\varepsilon(\omega)]\cong 0$ is fully accessible [74–76]. This marks a significant difference with the standard plasmonic behavior of metals in the visible spectral region, to which we are mostly accustomed. In that case, the high density of free carriers places the plasma frequency in the UV spectral region, whose access in plasmonics is, however, hindered by the strong interband absorption. Therefore, an ENZ behavior can be achieved with metal plasmonics only by resorting to metamaterials that act as tunable effective media [77–79], whereas heavily doped semiconductors intrinsically provide the users with this opportunity.

3.2 Losses in plasmonic material

When it comes to specific practical applications, plasmonic materials are usually employed to engineer nanophotonic platforms that sustain propagating SPPs and/or localized surface plasmon (LSP) resonances [80–83]. SPPs are transverse-magnetic surface modes that exist at the interface between a metal and a dielectric material. They possess a complex wavevector parallel to the interface (describing a damped wave-like propagation) and an imaginary wavevector perpendicular to the interface (associated with an evanescent tail whose confinement is largely explored for sensing). Localized resonances, in contrast, occur in bounded metal nanostructures surrounded by dielectric materials or in their reciprocal counterparts (a dielectric hole in a metal surrounding). Their characteristic feature is a very strong dependence of the resonance frequency on their shape and on the

refractive index of the dielectric material (also exploited for sensing).

In the comparison between metals and heavily doped semiconductors for mid-IR plasmonics, one of the most relevant and debated issues pertains to the losses [1]. It is now established that the imaginary part of the dielectric constant, to which losses are somehow related, cannot be taken as a simple direct indication for the quality of the associated localized plasmon resonances. Indeed, it can be demonstrated that a proper figure of merit (FOM) for such resonances is provided by the quantity ω_p/γ [84], implying that, for a given damping parameter γ, a higher plasma frequency ω_p is also beneficial in terms of losses. Indeed, for a fixed working frequency, a higher plasma frequency implies a larger absolute value of the negative real part of the dielectric constant, which is the essence of what we call a good conductor. For this reason, the quality factors of localized plasmon resonances in the mid-IR tend to be larger for metals than for heavily doped semiconductors. Other FOMs have been discussed in the literature, depending on the targeted quantity that one needs to optimize, for example, looking at the local field enhancement or at the extinction [85–88]. In general, losses in plasmonic materials are also inherently related to their ability to achieve subdiffraction field confinement [89]. This trade-off between the quality of the plasmonic oscillations and the associated field confinement is well captured by a recent analysis framework introduced by Dastmalchi et al., which employs SPPs as a benchmark [90]. In their approach, the dielectric constant of a conducting material is plot onto a 2D graph where the two coordinate axes are two FOMs related to SPPs. The first one describes their propagation length (and therefore the related losses), which is inversely proportional to the imaginary part of the in-plane wavevector, whereas the second one assesses the field confinement by measuring the spatial decay constant of the evanescent tail toward the vacuum, which is proportional to the imaginary part of the out-of-plane wavevector. Figure 2 demonstrates the behavior of a prototypical heavily doped semiconductor compared to that of Au in the mid-IR. The trade-off between losses (favoring Au) and confinement (favoring the semiconductor) is clear. Indeed, recent theoretical and simulation analyses comparing semiconductor plasmonics to Au in the mid-IR concluded that the enhancement achieved by the two platforms is within the same order of magnitude [84, 91]. This, together with other properties of semiconductors such as the high material quality, the possibility of tuning the optical response through doping or electrical/optical excitation, and the compatibility with standard foundry processes, makes the perspective integration of semiconductor plasmonic sensing devices a unique possibility that cannot be easily achieved with standard metals that are not CMOS compatible.

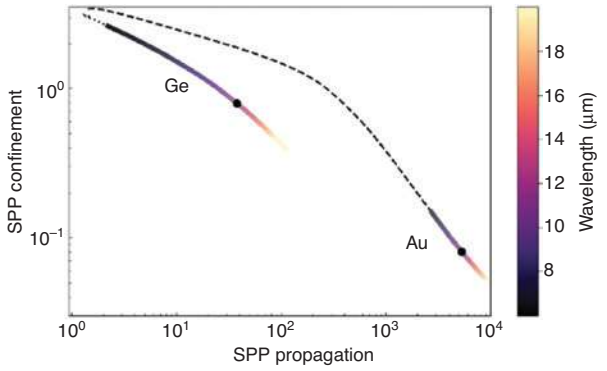

Figure 2: Evaluation of the mid-IR plasmonic properties of Au and a typical heavily doped Ge material characterized by a n-type doping density of about 8.8×10^{19} cm^{-3} and a screened plasma frequency corresponding to about 5.6 μm wavelength.
The experimental dielectric functions are employed to represent the material response as a function of an FOM for the SPP propagation length and one for the SPP confinement. Adapted from [91] with permission.

3.3 Optical characterization of doped semiconductors

From an experimental point of view, the characterization of the dielectric function of heavily doped semiconductors in the IR generally relies on the acquisition of transmission/reflection spectra with a Fourier transform IR (FTIR) spectrometer. An FTIR system is based on a Michelson interferometer and a thermal source, which together allow measuring the spectral response of a sample by Fourier transforming the acquired interferogram as a function of the phase delay between the two paths in the interferometer. A typical reflection spectrum, as sketched in Figure 3A, shows four prominent features: (i) a very high (almost 100%) reflectivity well below the plasma frequency, where the system behaves as a good conductor; (ii) a rather sharp drop in reflectivity around the plasma frequency, which marks the transition from conducting to dielectric (insulating) behavior; (iii) a minimum in the reflectivity when the real part of the dielectric constant equals 1 and is therefore index matched to vacuum (ideally implying zero reflectivity); and (iv) a set of fringes at higher frequencies due to Fabry-Pérot etaloning inside the semitransparent semiconductor film because of the refractive index contrast with the underlying substrate. In Figure 3B, we also show different simulated reflection

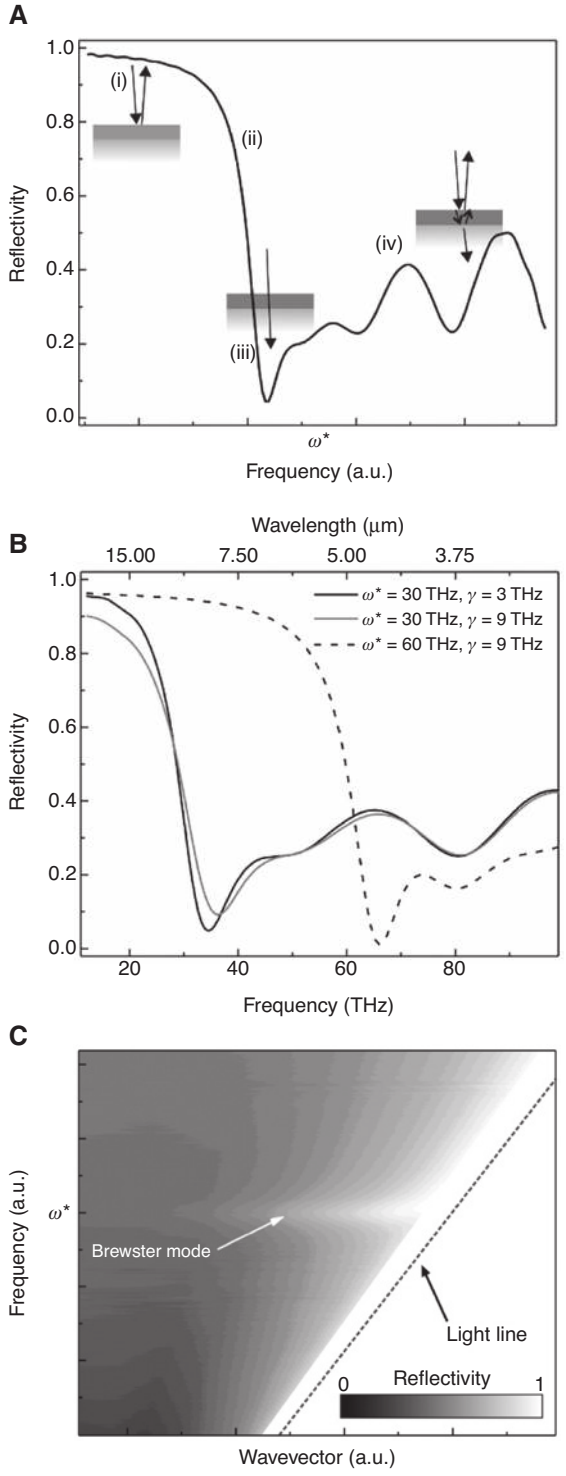

Figure 3: Infrared characterization of doped semiconductor films. (A) Simulation of a typical reflectance spectrum of a thick layer of heavily doped semiconductor. Four distinct regimes are apparent: (i) good conductor, (ii) plasma edge, (iii) index matching with almost-zero reflectivity, and (iv) dielectric behavior. (B) Impact of the plasma and scattering frequencies on the simulated reflectance spectra. (C) Reflectance dispersion for TM excitation of a $\lambda/50$ thin film of heavily doped InAsSb. Adapted from [92] with permission, Copyright 2014 The Optical Society.

spectra for different values of the scattering frequency γ and the screened plasma frequency ω^*. It is apparent how increasing the scattering frequency leads to a broader and smoother transition at the plasma edge (compare solid black and solid gray lines), whereas increasing the screened plasma frequency translates the plasma edge (compare solid and dashed lines).

In practice, the experimental spectra can be fitted numerically with a Drude-Lorentz model to extract all the relevant parameters for the dielectric function of the material. It should be stressed here, however, that the parameter values entering the mid-IR Drude-Lorentz model of a specific heavily doped material are not unambiguously defined by such a fitting procedure. Indeed, the value of ε_∞ changes accordingly to the number of high-energy oscillators that are explicitly included in the Lorentz summation. Although this has no relevant consequences for the quantitative estimate of $\varepsilon(\omega)$, it should be taken into account when, for example, the value of ε_∞ is employed to evaluate the doping density from the value of the screened plasma frequency ω^*. From this point of view, the plasma frequency ω_p is a much more robust fitting parameter in the Drude-Lorentz model and should be preferred when an estimation of the density of activated dopants is needed. As an alternative, as discussed before, Kramers-Kronig relations can be applied to the analysis, which requires, however, the availability of reflection/transmission data for all frequencies and therefore the use of a broadband spectrometer covering the whole spectral region from the THz to the visible range. In this way, the dielectric constant can be calculated without any a priori assumption or modeling [35].

Finally, special care is required when the thickness of the investigated doped layer is much lower than the skin depth for the penetration of the radiation inside the semiconductor material [93]. In this case, indeed, the film is partly transparent and 100% reflectivity is not achieved below the plasma frequency, rendering the fitting procedure more involved. An alternative characterization procedure is available for thin films when the primary goal is to determine the value of the screened plasma frequency without full knowledge of the frequency-dependent dielectric constant. In this case, collecting reflectance spectra under p-polarized light with a large incidence angle allows accessing the so-called Brewster mode [94, 95], which can be observed even for very thin doped layers (down to below 100 nm). This leaky mode directly couples to light and is enhanced near the screened plasma frequency thanks to the permittivity discontinuity leading to an electric field enhancement inside the doped layer. The consequence is the observation of a narrow dip in

the reflectance spectra near the plasma frequency, which clearly marks the plasma edge in the spectra with a high level of accuracy. This mode, predicted by Ferrell [96], was first observed by Steinmann [97] and McAlister and Stern [98] in an Ag foil and a similar mode was observed by Berreman [99] for polar materials. Its spectral signature is enhanced thanks to the cancellation of the permittivity ("ENZ" phenomena) near the frequency of the longitudinal mode of a polariton. This is why this mode is also termed "radiative ENZ mode" in the literature [100]. In Figure 3C, we plot a representative map with reflectance spectra as a function of the angular coupling for the TM excitation of heavily doped thin films, with thickness of the order of $\lambda/50$, clearly demonstrating the reflectance dip related to the excitation of the Brewster mode [92].

Ellipsometry can be also a powerful tool to characterize bulk material properties and access the real and imaginary parts of the permittivity. It consists of oblique incident excitation light whose polarization is controlled by a polarizer. The reflection at the sample surface modifies the polarization of the excitation light that is then analyzed by a second polarizer. However, this technique is not widely used in the mid-IR because, besides the complicated fitting procedure for the extraction of optical data for multilayered structures, it involves a relatively complex experimental setup for these wavelengths.

3.4 SPPs and plasmonic antennas

As already discussed in Section 1, one of the main driving forces for the development of plasmonic platforms in the IR spectral region is to achieve enhanced vibrational sensing and spectroscopy of molecules. This marks somehow a difference with standard surface plasmon sensing in the visible, which is typically a refractometric scheme that detects resonance shifts (either of SPPs or of localized plasmon resonances) as a consequence of changes in the dielectric environment. On the contrary, as the IR region is characterized by strong molecular resonances, plasmonic sensing here exploits the rich phenomenology of coupling between interacting resonators (the molecule on the one hand and the resonant plasma oscillations on the other hand). Perhaps for this reason, the most natural approach to surface-enhanced IR sensing so far has been the realization of nanoantennas, slits, or arrays (gratings) rather than the exploitation of propagating SPPs. Also, this is likely motivated by the fact that the first steps of mid-IR plasmonic sensing have been made with Au, which, as discussed before, is characterized by a poor intrinsic ability of field confinement in the mid-IR that is detrimental for SPP-based sensing. Possibly, in the near future, the establishment of semiconductor plasmonics might open new routes for the exploitation of SPPs in the IR. This would also be a natural extension of the well-established methods traditionally employed in mid-IR surface spectroscopy based on total-internal reflection schemes.

In the next sections, we will highlight the main features of IR plasmonic devices based on heavily doped semiconductors. It is not the purpose of this analysis to cover the rich phenomenology related to SPPs and LSPs, for which the reader is referred to the many books and reviews on the topic [80–83, 101]. Rather, we aim at briefly drawing their main features and specifically stressing the opportunities provided by semiconductors and their differences in comparison to standard metals.

3.5 Modeling of localized plasmon resonances

The shape of plasmonic nanoparticles drastically affects their optical properties. If elongated as in Figure 4A, the nanoparticles, often referred to as nanoantennas, can sustain at least two resonant modes that can, for example, be observed in reflectance or transmittance geometry with an electric field polarization oriented along the short axis (high-frequency resonance) or the long axis (low-frequency resonance). Higher-order, coupled, and collective resonances can then be engineered by increasing the number of nanoparticles and changing their individual geometry. To describe and understand the physically meaningful properties of such systems, it is fundamental to be able to model the optical properties of LSP resonances (LSPRs). Models are the building blocks to predict and design any nanophotonic device [102]. Nevertheless, they have to consider several features such as a broad variety of dielectrics and metals, an accurate description of the geometry scaling from the nanometer to the millimeter range, and field amplitude variations over several orders of magnitude in addition to possible nonlinearities, magneto-optical effects, and quantum effects. To do so, it is necessary to solve Maxwell's equations with the proper boundary conditions that describe the geometry of the problem but mostly with an adapted formulation to the problem to be solved. There are several different typical problems that are addressed in nanophotonics: the propagation of light, its localization, and its diffusion (scattering) together with multiscale problems that include geometry scaling, nonlinear optical processes, nonlocal effects, quantum effects, and 2D materials (e.g.

graphene or MoS_2). To this aim, we can resort to analytical methods [103], semianalytical methods [104], or numerical methods with commercial [105, 106] or freeware software [107–109]. All these approaches, and especially the numerical ones, solve Maxwell's equations in different conditions. The numerical solvers operate with either a differential or an integral formulation of the problem and either in the time domain or in the frequency domain. The ease of solving the considered nanophotonic problem will depend on the choice of the method to solve Maxwell's equations.

One of the main points to consider in solving Maxwell's equations by numerical methods is the discretization [102]. In their differential formulation, discretizing Maxwell's equations in space and time using finite differences allows one to solve them in the time domain [finite-difference time-domain method (FDTD)] [110]. However, to obtain an accurate description of the nanostructure, the mesh has to be fine enough and this affects the computational time. Moreover, if the coordinate axes are not parallel to the nanostructure surfaces, aliasing and staircase effects appear. Figure 4B shows an example of the discretization by the staircase approximation in the nanostructure of Figure 4A and the surrounding materials. Expanding the electromagnetic fields as local functions in elements as for the finite element method (FEM) gives a more faithful representation of the nanostructure (Figure 4C) and more accurate results in the frequency domain. However, time-domain description is much more adapted to study systems with transient field effects or nonlinear behaviors of the material. To combine the time-dependent calculations with a higher accuracy in the geometrical description, time-domain methods can be adapted to FEMs, but the global linear system of equations needs to be solved at each time step, which is time consuming. A more adapted technique is the discontinuous Galerkin time-domain (DGTD) method [111], consisting in ensuring the continuity between adjacent elements by numerical fluxes rather than by operating on the tangential field components. This relaxation of the continuity conditions reduces the linear system of equations to a block-diagonal system that is less time consuming to solve.

The integral formulation, in contrast, has the main advantage to only deal with the nanostructure and to consider the surrounding materials as homogeneous. These methods resort to the dyadic Green's function to seek the solution and to only discretize the nanostructure [112]. Figure 4D shows the discretization in the volume of the nanostructure with the discrete dipole approximation (DDA) [113], a common volume integral method. This approach can even give an analytical solution in the case of simple geometries such as a sphere. If the simulated structure is large compared to the operating wavelength, it can be useful to work with a surface integral method such as the surface integral equation (SIE) [114] or the boundary element method [115]. In this case, instead of dealing with dipoles everywhere in the nanostructure, only the surface is modeled (Figure 4E). Notably, surface integral methods are best suited to describe the nanostructure with a piecewise homogeneous material. This method is peculiarly adapted to describe the scattering processes of irregular nanoantennas where it is fundamental to link accurately their near- and far-field optical properties, which is, for example, the case for surface-enhanced Raman scattering (SERS) [116].

Other methods exist. They generally rely on the expansions of the electromagnetic field on basis functions with symmetry adapted to the problem to be solved and with the proper boundary conditions enforced at interfaces between the different materials. For example, the T-matrix method expands the electromagnetic field on spherical basis functions [117] and is particularly adapted to solve the scattering problem of spherical or quasi-spherical geometries. When the electromagnetic field is expanded into multipoles such as in the generalized multipole

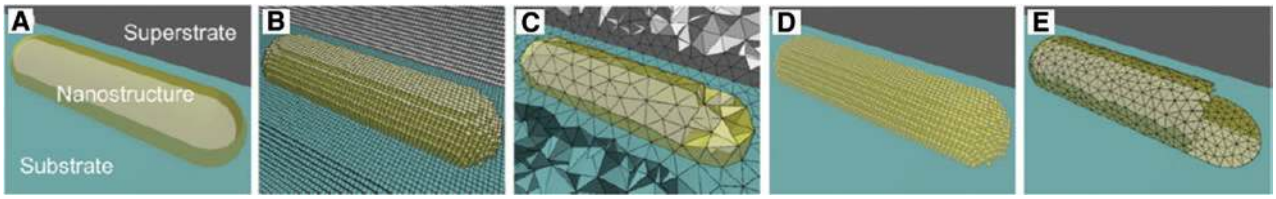

Figure 4: Discretization schemes for electromagnetic numerical simulations.
(A) Example of nanostructure to model. (B) Discretization in the nanostructure and the surrounding materials using a Cartesian grid for the finite difference in time-domain method. (C) Discretization in tetrahedral elements of the nanostructure and the surrounding materials for finite element or DGTD method. (D) Discretization in dipoles inside the nanostructure for DDA. (E) Discretization in triangular element at the surface of the nanostructure for SIE method. Reprinted from [102] with permission, Copyright 2015 John Wiley and Sons.

technique [118], the geometry constraint is much more relaxed because the multipoles can be centered close to each actual scatterer. Finally, the rigorous coupled-wave analysis method is among the preferred ones to solve scattering problems from periodic structures because it relies on a Fourier expansion of the electromagnetic field [119].

The most suitable method to solve Maxwell's equations has therefore to be carefully chosen to save the computation time and reduce the memory requirement depending on the system and the physical quantities that need to be computed [102]. The FEM and DGTD methods are particularly suited to solve device problems with large differences in the spatial scale and where propagation problem have to be considered simultaneously to localization effects, whereas the FDTD method is especially effective to solve broadband problems. The surface and volume integral methods are much more suited for scattering and localization problems.

All the methods described above can be used to analyze the behavior of mid-IR semiconductor plasmonic devices. In this respect, it is interesting to notice how, spectrally speaking, antennas in the IR lay in between classical radiofrequency (RF) antennas and novel plasmonic antennas. Indeed, standard metal antennas made of very good conductors have been developed for a long time by employing metal wires to collect and emit radiation, originally in the RF and microwave range but then also in the THz [120] and mid-IR [121–126] range, whereas plasmonic antennas are much more recent [127, 128]. But what is exactly an antenna and what are the main differences between a classical antenna and a plasmonic antenna? Antennas allow us to emit or receive electromagnetic waves, exploiting the flow of electrons at the antenna surface. When the antenna is subject to an electromagnetic field, electrons move back and forth, creating oscillating currents along the antenna. A standing wave appears because the current is reflected at each extremity undergoing a phase shift of half a wavelength. This standing wave creates a field maximum in air at each antenna end that can be enhanced by the lightning rod effect, i.e. the field enhancement due to the small radius of curvature. The antenna therefore converts electromagnetic waves into oscillating currents and vice versa. By doing this, it creates a link between propagating far fields and localized near fields. This process does not need any plasmonic effect. The antenna can be made of a perfect conductor or a metal with an extremely high absolute value of the permittivity, i.e. a Drude-like material operating far away (well below) its own plasma frequency. Reducing the permittivity values of the metal and working closer to the plasma frequency allows the electric fields to penetrate inside the antenna arms, converting surface currents into volume currents. As already discussed, this is intrinsically associated with larger losses but also with improved confinement [89]. For a given operating wavelength, the relative size of the antenna reduces when passing from radio to visible frequencies, which is associated with an increase in the effective index of the antenna modes [129, 130], as shown by the dispersion relation in Figure 5A. Whereas at radio frequencies the dispersion relation of the metal surface almost coincides with the light line in air, in the plasmonic regime it bends significantly. As a consequence of this rich phenomenology, in plasmonic antennas, there is a mismatch between the wavelength of antenna modes and that of the propagating radiation. This results also in a significant change in the radiation patterns (Figure 5B–D), which plays a major role in the design of plasmonic antennas [131].

The plasmonic effects described so far are largely negligible in the case of Au antennas in the mid-IR or the THz. Their near-field optical properties are essentially dominated by the lightning rod effect, by the presence of nanoscale gaps, and by collective diffractive phenomena in the case of periodic antenna arrays that are currently exploited for sensing [5]. In contrast, Au nanoantennas in the visible range and doped semiconductors in the mid-IR and THz range combine these effects with a genuine plasmonic behavior and a higher degree of intrinsic (i.e. material-related) field confinement.

3.6 Optical properties of IR semiconductor antennas

The optical properties of plasmonic antennas deeply depend on the field distribution at the near-field scale so a weak modification of the antenna's shape can drastically affect its optical properties. Applying a scale law to reduce the antenna size makes it possible to qualitatively transfer RF antenna designs to the IR range: this allows accessing a large zoology of antennas [5], which have been largely exploited in Au-based plasmonics. All shapes of plasmonic antennas are also possible with doped semiconductors, although just a few of them are present in the literature mainly because semiconductor plasmonics is still at an infancy stage and also because growth and fabrication technology with Au is easier to access compared to semiconductor technology.

One practical issue that is of relevance when developing all-semiconductor plasmonic platforms is that usually their epitaxial growth requires the use of high-index substrates, such as Si or GaAs. This marks a

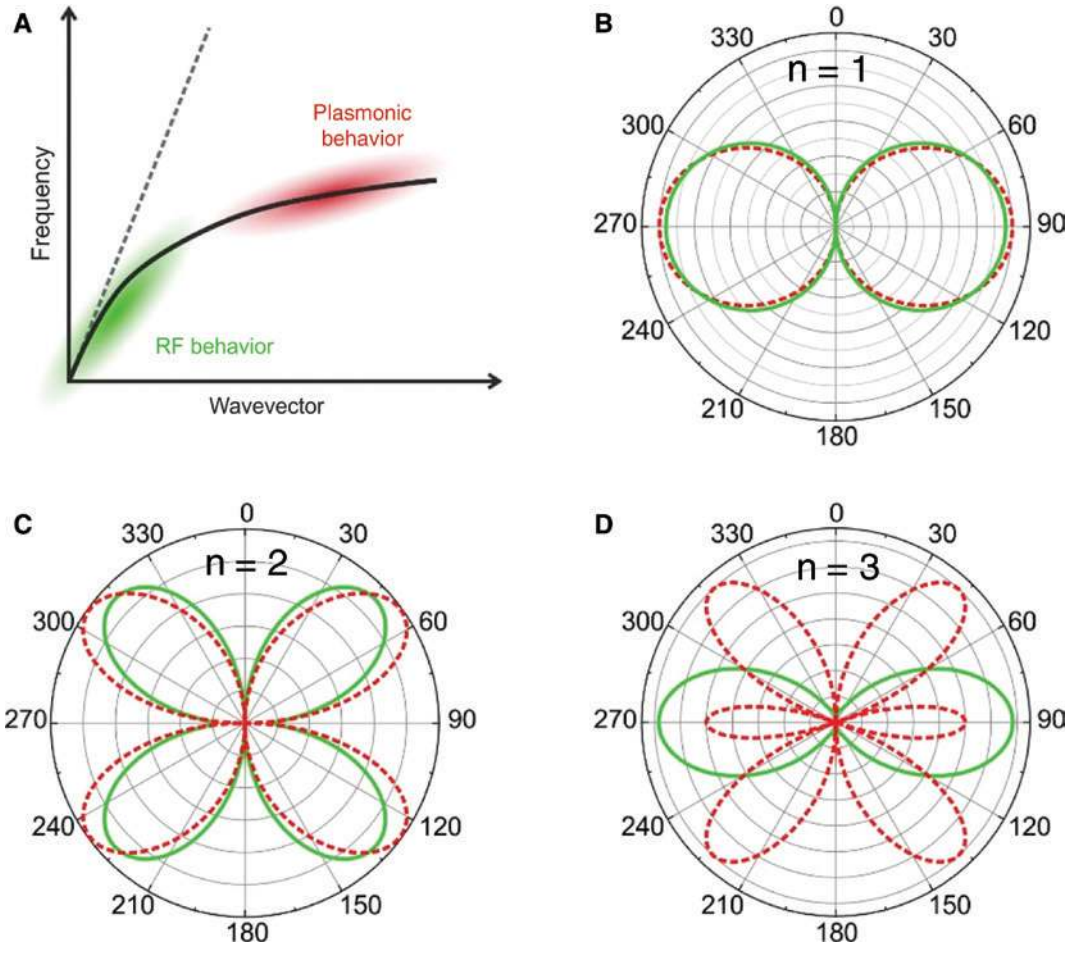

Figure 5: Comparison between the typical radio-frequency and plasmonic behaviors of antennas.
(A) Sketch of the typical dispersion relation for the mode propagating along the antenna wire in the RF (green region) and visible (plasmonic, red region) parts of the electromagnetic spectrum. (B–D) Plot of the radiation patterns for the first three antenna modes in the case of RF (solid green lines) and plasmonic (dashed red lines) antennas. Adapted from [131] with permission.

difference with our general understanding of localized plasmon resonances in Au nanostructures that typically sit on low-index glass substrates. Indeed, the presence of a high-index substrate is known to bend the electric field lines downward, which limits their interaction with the surrounding environment. Moreover, a stronger induced mirror dipole will be present, which will typically lower the resonance quality via near-field interactions. Finally, the large index contrast between the air (or the analyte) and the substrate, together with the relatively large thickness of semiconductor plasmonic devices, tends to decouple the plasmonic behavior at the upper and lower surfaces of the plasmonic device, often resulting in two split resonances as recently demonstrated in both grating arrays [63] and individual antennas [60, 91]. One resonance involves plasmonic currents that are mainly localized toward the air interface and lay at higher frequencies, whereas the other one involves currents that are mainly located at the substrate interface and possess a lower resonance frequency. Another important difference between semiconductor and Au antennas in the IR is the amplitude of the scattering processes compared to the absorption processes. The absorption cross-section dominates in the case of doped semiconductors because of the lower carrier concentration that allows for a deeper electric field penetration into the material. Although this might be a drawback for certain applications, when the absorption cross-section dominates over the scattering cross-section, a closer packing of the antennas is possible without deteriorating the quality factor of their resonances thanks to the reduced interaction between adjacent antennas in the array. This, together with the geometrically smaller footprint of plasmonic antennas compared to perfect conductors, increases the hotspot density and therefore the active surface useful for sensing applications [129, 130]. Similarly, the close packing of

periodic structures is easier with heavily doped semiconductors and allows one to access very high wavevectors because of the dispersion relation bending of the SPP and quasi-LSP modes. Their behavior is very similar to that of localized plasmon modes even for periodic arrays. Both propagating surface plasmons and LSPs can coexist in arrays of doped semiconductors, which were intensively studied at the early stage of this field of research in the THz range with doped Si [132]. Here, grooves and holes were realized by a dicing saw to study the impact of the geometry (hole spacing and size) on the transmittance of SPPs through the grating (Figure 6A and B). InSb arrays (Figure 6C and D) have also been investigated to demonstrate the possibility to control the carrier density by direct or laser heating that impacts the plasma frequency and therefore the SPP properties in the THz range [133, 134]. Indeed, changing the temperature of the InSb material increases the carrier density because of its small band gap.

The extension of doped semiconductor arrays to the mid-IR range is more recent, with Si-doped InAsSb gratings featuring a short periodicity (pitch between 0.5 and 2 μm) used to excite LSP modes or high-wavevector SPP modes [63, 65] (Figure 7A). In such a system, one can tune

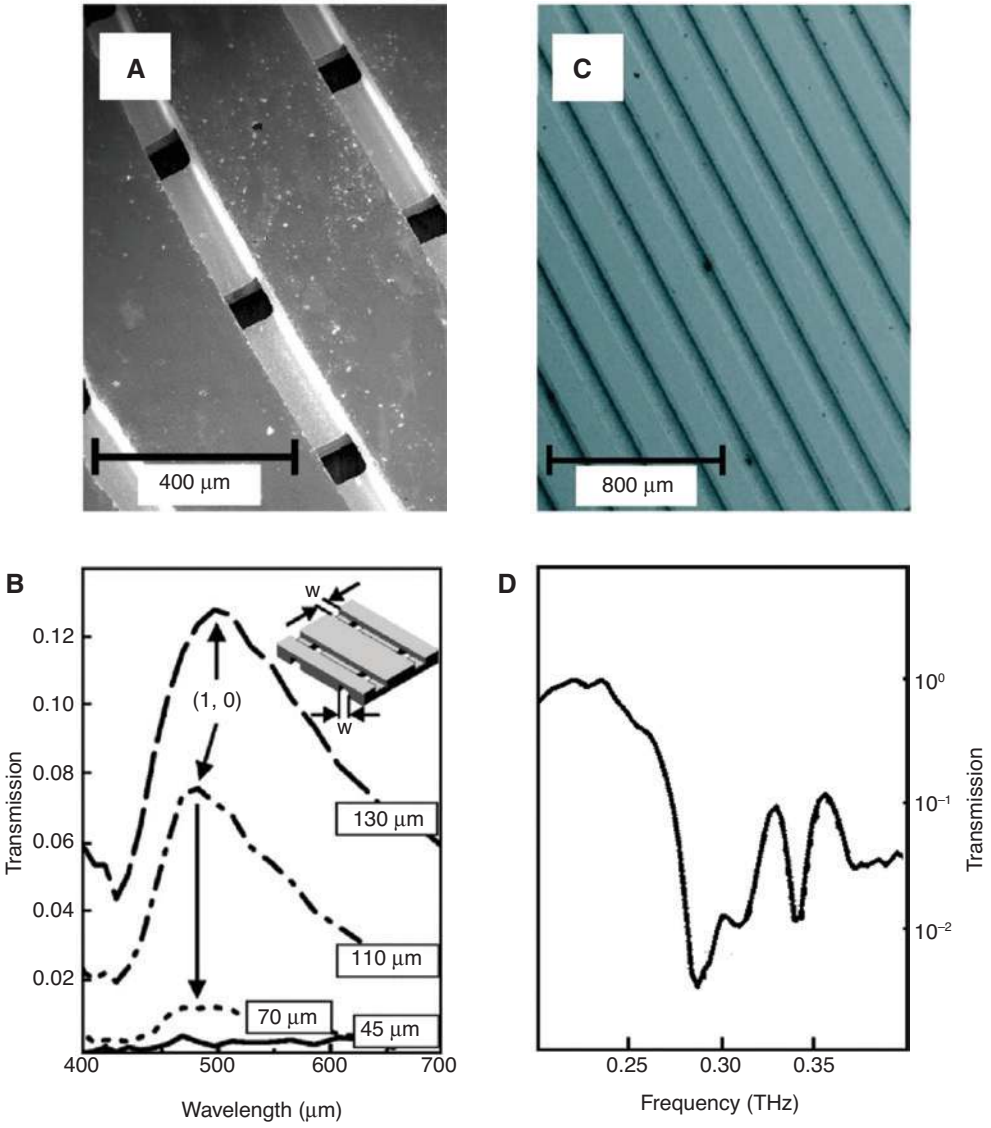

Figure 6: Semiconductor plasmonic gratings for the THz spectral range.
(A) Scanning electron microscope (SEM) micrograph of a square grating with subwavelength holes fabricated with a dicing saw and (B) transmission spectra for different hole sizes [132]. (C) SEM top view of an SPP Bragg grating structured on InSb and (D) transmission spectrum measured with time-domain spectroscopy [133]. (A and B) Reprinted from [132] with permission, Copyright 2004 Amrican Physical Society. (C and D) Reprinted from [133] with permission, Copyright 2006 American Physical Society.

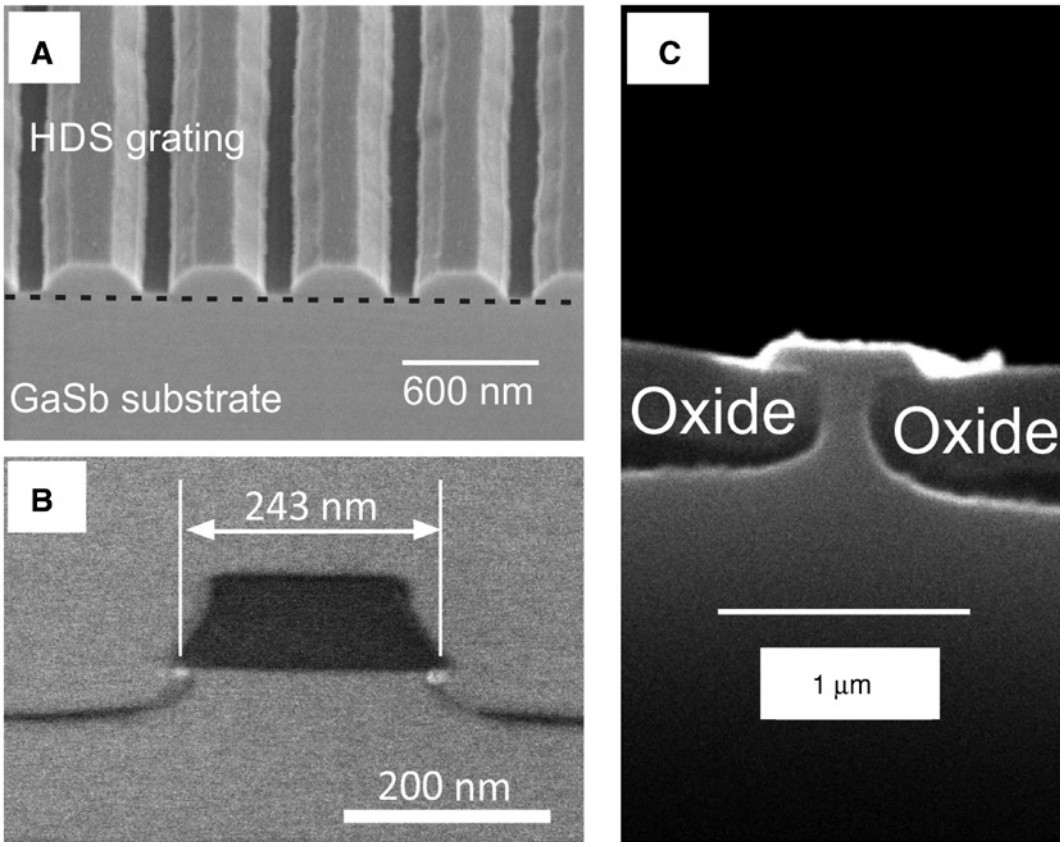

Figure 7: Semiconductor plasmonic gratings for the mid-IR spectral range.
(A) SEM image of a tilted view of an Si-doped InAsSb array. (B) Cross-section of one ribbon by bright-field scanning transmission electron microscopy [64]. (C) SEM image of a cross-section of a Si-doped InAsSb pedestal antenna [135]. (B) Adapted from [64] with permission, Copyright 2015 The Opitcal Society. (C) Adapted from [60] with permission.

the resonance frequency adjusting the doping level or the ribbon width. In the perspective of integration to semiconductor technology, InAsSb resonators buried into GaSb (Figure 7B) have been demonstrated. The frequency and the shape of the LSPR are deeply affected but remain tunable by a careful design of the plasmonic antennas [64]. To continue taking advantage of the size reduction for a given plasma frequency and because, as discussed before, the typical refractive indexes of the semiconductor substrates are high (about 3–4), it can be interesting to develop pedestal antennas such as those demonstrated in Figure 7C, where the pedestal geometry is realized by partially oxidizing the GaSb substrate [135]. The active surface of the pedestal antennas is larger and the quality of the resonances is higher, which increases the sensitivity for biosensing [136, 137]. Finally, adjusting the ribbon's width and the carrier density of the InAsSb by the doping level (something that is not possible with standard metals) allows one to bring the LSPR at the chosen frequency in the mid-IR [65].

The experimental demonstration of individual semiconductor plasmonic antennas in the mid-IR is also very recent and benefits from all the previous studies employing Au antennas. The simplest antenna geometries are the nanosphere and the nanorod, sustaining a fundamental dipolar resonance. When we consider lithographed antennas on a substrate, the natural counterpart of nanospheres is represented by nanocylinders or nanodisks. Along this line, closely packed doped InAs nanoislands have been fabricated on undoped InAs/GaAs substrates, experimentally demonstrating two separate localized plasmon resonances occurring at the antenna-air and antenna-substrate interfaces (Figure 8A and B) [69].

The most common antenna geometry, however, remains the nanorods. Their simplicity of fabrication and the high field enhancement appearing at their extremity are favorable for surface-enhanced spectroscopy techniques [139, 140]. The parallelepiped antennas in Figure 8C and D are made of n-doped Ge with a carrier concentration of 2.3×10^{19} cm^{-3} that gives a plasma frequency of about 10 μm wavelength [60]. This plasmonic antenna also gives two main dipolar resonances because of the high-index substrate and the large thickness of about 1 μm,

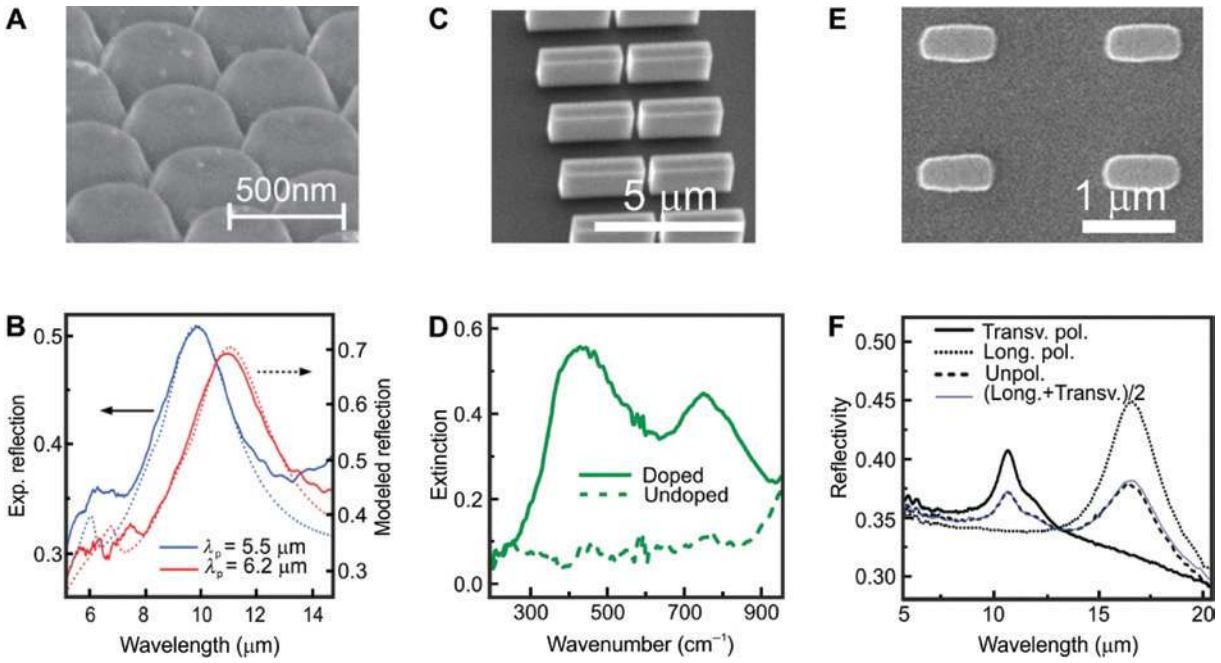

Figure 8: Mid-IR resonances of semiconductor antennas.
(A and B) SEM image and reflection spectra (solid lines: experiment; dashed lines: simulations) of Si-doped InAs islands fabricated on GaAs substrates by nanosphere lithography [69]; blue and red lines refer to two different samples with different doping levels and therefore different plasma wavelength λ_p. (C and D) SEM image and extinction spectra of gap antennas made of phosphorus-doped Ge fabricated on Si substrates by EBL [60]; the spectra reveal the two resonances associated with plasmon oscillations at the Ge-air interface (higher frequency) and at the Ge-Si interface (lower frequency). (E and F) SEM image and polarization-resolved reflectivity spectra of InAsSb antennas fabricated on GaSb substrates by EBL [138]. (A and B) Reprinted from [69] with permission, Copyright 2013 American Chemical Society. (C and D) Reprinted from [60] with permission, Copyright 2015 American Chemical Society. (F) Reprinted from [138] with permission.

the substrate-like mode at the interface between Ge and Si of about 20 μm wavelength (500 cm^{-1}), and the air-like mode at the interface between Ge and air of about 11.5 μm wavelength (850 cm^{-1}). Also, one of the main advantages of plasmonic antennas is the possibility to work exploiting both short- and long-axis resonances, which is not possible with Au antennas whose transverse resonance lays in the visible spectrum and has indeed been exploited for combined surface-enhanced Raman and IR spectroscopy [141]. Elongated Si-doped InAsSb plasmonic antennas also give plasmonic resonances in the mid-IR (Figure 8E and F).

3.7 Experimental characterization of IR plasmonic antennas

Plasmonic antennas are designed to feature a specific optical functionality and to develop a targeted application. To validate their optical properties, it is fundamental to characterize them with the proper spectroscopy tools. The simplest techniques are based on the acquisition of reflectance or transmittance spectra at normal (or quasi-normal) incidence. Transmittance is often referred to as extinction and contains information on both absorption and scattering by the plasmonic sample. Therefore, it typically provides a very clear signature for the excitation of plasmonic resonances that reveal themselves as a dip in the spectrum (light is either resonantly absorbed or resonantly scattered by the sample). The scattering of light away from the forward direction, in particular, can be related either to the single-particle radiation pattern or to collective, grating-induced diffraction modes. The interpretation of reflection spectra can instead be more involved, as the intensity collected at the detector is the result of an interference process between the radiation that is back-scattered (with a certain phase difference) by the plasmonic structures and that reflected by the high-index dielectric substrate. This process can result in complex interferential line shapes that require proper numerical modeling for their analysis [142].

Reflectance and transmittance experiments are generally performed with an FTIR spectrometer operating with the proper configuration (beam splitters, detectors, and sources) for the selected spectral range. Because of the low brilliance of IR sources and the low sensitivity of detectors, measuring single antenna spectra is challenging, at

variance with the standard practice in visible and near-IR plasmonics. Nevertheless, IR spectroscopy of single nanoantennas has been performed using an IR synchrotron light source coupled to an FTIR spectrometer and a high-detectivity mercury-cadmium-telluride detector [139] or by an optimized confocal transmission microscope operating with broadband pulses coupled to Cassegrain objectives [143].

As mentioned previously, Kramers-Kronig relations can be used to extract the bulk optical properties of doped semiconductors but they can also be employed to analyze the reflectance spectra of plasmonic antennas. Indeed, a plasmonic resonator can be modeled as two damped Lorentzian oscillators that we can describe with a longitudinal and a transverse natural frequency [144].

Much more generally, the acquisition of angular-dependent reflectance and transmittance spectra provides a deeper physical insight into the nature of plasmonic resonances. Indeed, it allows accessing their dispersion relation, as demonstrated, for example, in Figure 9A and B, and notably to distinguish between localized plasmon modes, whose resonance frequency is not sensitive to the angle of incidence or wavevector, and propagative/collective surface plasmon modes, whose resonance frequency is sensitive to the angle of incidence or wavevector [64, 92, 145].

Time-domain pump-probe experiments are also ultrasensitive experimental tools to characterize plasmonic platforms. Generally speaking, they are based on the control of the relative time delay between two trains of pulses originating from the same source, one of which is used to excite the sample and the other one to probe its response as a function of the time delay. Pump-probe spectroscopy has been applied to IR semiconductor plasmonics in the literature mainly with two different types of experiments: in a first set of works, near-IR laser pulses are used to photogenerate free carriers in plasmonic antennas and a mid-IR probe measures the dynamics of such free carriers and notably of the associated plasmonic modes [35, 61, 146]. This possibility to optically control and trigger the plasmonic response of a semiconductor will be discussed later on with more details. Another time-domain characterization technique that is widely used is the so-called electro-optical sampling. This technique was originally developed in the THz range and it is based on two near-IR pulses that are used to generate and detect the THz radiation. One of the beams photogenerates electron-hole pairs in a piece of semiconductor, which are accelerated in the depletion layer and act as dipoles that emit broadband THz pulses. This THz radiation can then be used to study the response of plasmonic antennas. To analyze the THz beam after interaction with the sample, the second near-IR pulse is incident on a photoconductive switch, generating carriers that are then put into motion by the electric field of the THz pulse and produce a measurable current. By varying the time delay, the electric field of the THz pulse is thus reconstructed with subpicosecond temporal resolution as limited by the carrier lifetime inside the photoconductive switch. Finally, the acquired time trace can also be Fourier transformed to provide the spectral response of the plasmonic device. This technique was, for example, used in the THz domain to analyze the transmission through Si gratings [147] but can also be extended to the mid-IR by changing the generation process for the excitation radiation, which is typically obtained by means of optical parametric amplifiers [148].

The characterization of localized plasmon resonances in nanoparticles and nanoantennas, besides the far-field

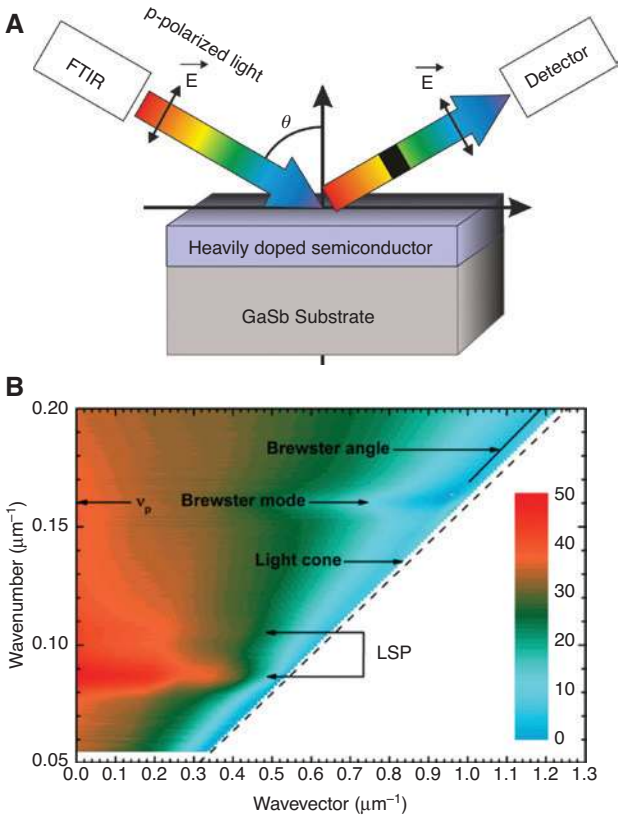

Figure 9: Angle-resolved characterization of semiconductor plasmonic gratings in the mid-IR.
(A) Brewster mode configuration [145]. (B) Reflectance dispersion under p-polarized light of an Si-doped InAsSb array. The light cone is represented by the dark dashed line. The Brewster angle is represented by the dark solid line and the Brewster mode occurring at the plasma frequency υ_p is indicated by the horizontal arrow. LSP modes are also indicated by the linked arrows [64]. Adapted from [64] with permission, Copyright 2015 The Optical Society.

analysis by means, for example, of scattering or extinction spectra, often entails an assessment of the local fields generated in close proximity to the antenna. Such fields, whose enhancement and localization is the essence of all plasmon-based sensing concepts, possess strong nonpropagating near-field components whose analysis requires a scanning local probe. Scattering-type near-field microscopy has emerged over the last decade as a powerful and versatile tool to investigate plasmonic field distributions in the IR spectral region [149, 150]. The main idea behind the use of an atomic force microscopy tip for near-field imaging is that the plasmonic resonances are excited with a far-field illumination and a polarization parallel to the sample plane, whereas the tip possesses a significant polarizability only along its own axis, i.e. perpendicular to the polarization of the excitation far fields. Local near fields, on the contrary, display all spatial components according to the specific distribution of the charge oscillations and therefore can couple to the tip dipole, which scatters them to the far field where they can be detected, usually employing heterodyne amplification. Although this approach has also been successfully employed in the visible and near-IR parts of the electromagnetic spectrum [151], the advantage of its use in the mid-IR is even more dramatic given that the lateral resolution is roughly determined by the size of the tip apex, which for this spectral region can be of the order of $\lambda/100$. Recently, this has been applied to doped InAs nanowires to demonstrate gate-tunable spatial modulation of localized plasmon resonances [152]. Noticeably, this technique also allows for the study of strain in semiconductor nanostructures by leveraging on the specific IR absorption lines associated with surface phonon polaritons (optical lattice vibrations in polar crystals) [153].

During the last few years, alternative near-field approaches have also been developed for IR microscopy. Photothermal induced resonance microscopy is a photoexpansion mapping technique that uses the atomic force microscopy probe as a mechanical transducer of the local sample expansion due to the resonant absorption of IR light. It has been applied to measure the thermal expansion due to Joule heating in resonant InAs nanostructures [154] and to map the local near-field distribution of heavily doped Ge bow-tie antennas operating at a wavelength of 4.5 mm and covered with a thin polymer layer [68]. Photoinduced force microscopy can be used to image the dipole force between the probe and the sample. In this case, it has been possible to distinguish dissipative (absorption-related) from dispersive (real part of the dielectric function) line shapes [155]. Finally, it should be mentioned here that to improve the performance of near-field microscopy the use of resonant plasmonic tips has also been proposed [156] and that, in this framework, heavily doped semiconductors provide a possible path toward the mass fabrication of resonant IR tips exploiting the available foundry technologies. Resonant Ge tips, for example, have been applied to the study of free carriers in ZnO nanowires by mid-IR near-field microscopy [157].

3.8 Doped semiconductors versus metals in the mid-IR: a difficult comparison

Although Au is still the plasmonic material of choice for most applications, its use suffers from some limitations, notably in the subwavelength confinement of electromagnetic modes and related metamaterial applications [158] and for the very poor compatibility with the mainstream microelectronic foundry processes. Several studies tried to make a fair comparison of the optical and sensing performance of Au and doped semiconductors in the mid-IR. This is, for example, the case of the comparative study performed by Barho et al. on ribbon arrays of doped InAsSb compared to Au. They demonstrated theoretically an electric field enhancement larger by one order of magnitude in favor of the doped semiconductor (Figure 10A and B) and experimentally a highest sensitivity in sensing [159]. However, these results are not unexpected when one considers that both the simulated devices possess a ribbon thickness of 100 nm. Although a thick layer is indeed needed for the optimized semiconducting grating because of the large skin depth for mid-IR radiation in this material, the same thickness is not needed for Au because of the extremely low field penetration and is instead detrimental as it inhibits lightning-rod enhancement effects.

A more recent study by Hsieh et al. reached opposite conclusions in the comparison of doped InGaAs spheres and Au nanorods [84]. The authors demonstrate a higher field enhancement, by a factor of 2, for Au antennas (Figure 10C and D). However, also, in this case, this does not come as a surprise as the two investigated systems have a quite different radius of curvature (700 nm for the InGaAs sphere and 300 nm for the Au nanorod), which results in a different role played by curvature-induced charge accumulation and lightning-rod field enhancement.

Eventually, as already mentioned in this review, one should always recall that the response of heavily doped semiconductors in the IR is qualitatively very similar to that of noble metals in the visible (the main notable difference being the achievement of ENZ behavior thanks to the absence of interband transitions). To dig further into this, we can calculate the quasi-static field enhancement

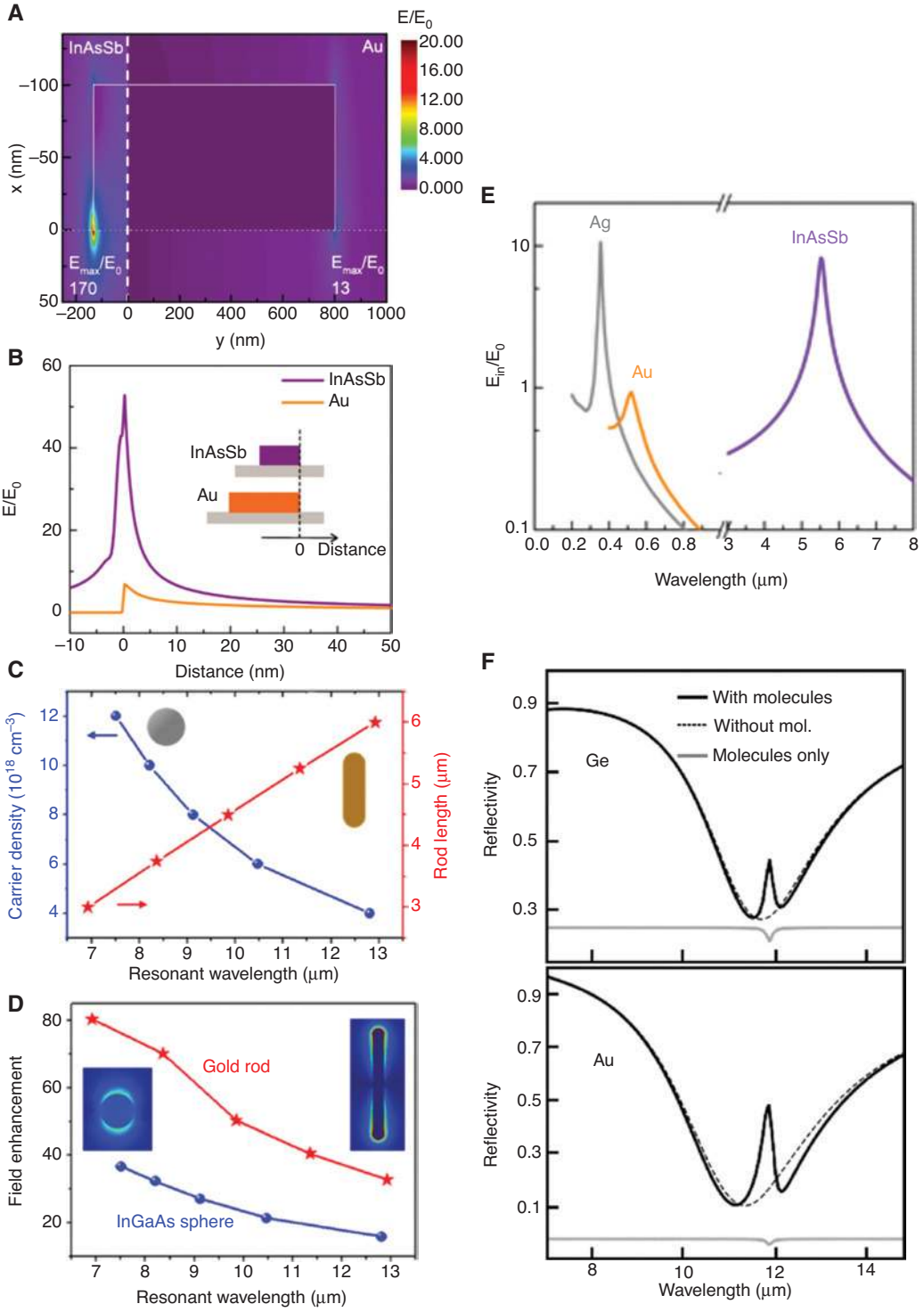

Figure 10: Comparison between metal and semiconductor antennas.
(A) Electric field profile at 10 μm wavelength for the single InAsSb ribbon (left) and single Au resonator (right) on a GaSb substrate. (B) Cut through the field profile 1 nm above the substrate-resonator interface. The sidewall of both resonators has been placed at the origin $x=0$ to compare the evanescent field of the semiconductor and the Au resonator [159]. (C) Adjusting the doping in an InGaAs sphere with 1.4 μm diameter or the length of an Au rod with fixed cross-section of 0.6 μm diameter, it is possible to tune the LSP resonant wavelength. (D) Maximum achievable field enhancement for both structures [84]. (E) Electric field enhancement in a spherical nanoparticle in vacuum for different plasmonic materials computed in the quasi-static approximation. (F) Sensing of a vibrational line of about 12 μm wavelength with optimized resonant Ge and Au slit arrays [91]. (A and B) Adapted from [159] with permission, Copyright 2016 The Optical Society. (C and D) Adapted from [84] with permission, Copyright 2017 American Chemical Society. (F) Adapted from [91] with permission, Copyright 2018 American Chemical Society.

inside a sphere for different materials using Mie theory and the tabulated value of the permittivity for Ag, Au, and InAsSb [65, 160]. Figure 10E demonstrates that the highest enhancements are obtained for Ag and InAsSb, with the Au enhancement being one order of magnitude lower. These differences are due to the internal material losses compared to plasma frequency, which are much more favorable for Ag and InAsSb than for Au. However, the important point that we have to keep in mind is the strong wavelength dependence of these results. In other words, the material choice is strongly linked to the working wavelength range. Therefore, any comparison should be done with a specific targeted application in mind.

This was done recently, for example, by Pellegrini et al. who benchmarked heavily doped Ge against Au with the specific goal of sensing a vibrational resonance at a wavelength of 12 μm [91]. To take the respective skin depth into proper account, the authors considered different thicknesses for the two systems (50 nm Au and 300 nm Ge). After carefully optimizing the two slit arrays and assessing their sensing performance with three different FOMs, they confirmed that the signal enhancement provided by heavily doped semiconductors does not outperform that by Au, although the difference is not significant (much less than an order of magnitude), as also found in the work by Hsieh et al. (see Figure 10F).

To conclude, making a fair comparison between plasmonic materials that are as different as metals and semiconductors is not an easy task. Typically, if one selects a specific working wavelength, different antenna geometries need to be considered that exploit different confinement effects (plasmonic, lightning rod, or gap-related) to optimize them individually. In contrast, when a specific antenna geometry is chosen, the natural working wavelength will be different for different materials. Each material has its advantages and its drawbacks. As mentioned previously, the high material quality, the possibility of tuning the optical response through doping or electrical/optical excitation, and the compatibility with standard microelectronic fabrication processes make the perspective of integration of semiconductor plasmonic sensing devices a unique possibility that cannot be easily achieved with standard metals that are not CMOS compatible.

4 Applications of semiconductor nanoantennas

The mid-IR range is of particular interest for biomolecules thanks to the specific absorption lines that represent a spectral signature related to their vibrational modes. For this reason, IR spectroscopy has found countless applications in security and health, where it allows one to unambiguously detect the presence of specific classes of molecules. In this framework, surface-enhanced spectroscopies pursue the goal of increasing the sensitivity of standard techniques and making them capable of detecting very small quantities of analytes. Traditionally, plasmon-enhanced sensing in the visible is intrinsically refractometric as it measures the resonance shift of surface plasmon resonances (SPRs) as a function of the refractive index change at the metal surface. This often requires proper surface functionalization to selectively address a specific molecule or class of molecules. In the IR, the situation is made more complex, but for this reason also more versatile, by the coupling between the plasmonic resonances and the molecular ones, which leads to a vast phenomenology of spectral modifications and enriches the possibilities and the available sensing strategies with the added value of molecular specificity. These approaches usually go under the name of surface-enhanced IR absorption (SEIRA).

Moreover, beyond the standard route of static doping during the growth, which has already been extensively discussed in this review, semiconductor materials also offer the exciting possibility for the active control of their population of conduction electrons either by means of electrostatic fields applied via a back gate electrode or by means of illumination with optical pulses and the subsequent absorption of photons. Such possibilities pave the way toward the realization of integrated, active, and possibly ultrafast tunable plasmonic devices in the mid-IR.

Finally, in this section, we will briefly address other applications of semiconductor mid-IR plasmonics, in particular, waveguiding, nonlinear optical conversion, ENZ phenomena, metamaterials, and intersubband plasmons.

4.1 Plasmon-enhanced refractometric sensing

Plasmonic sensing can be based either on propagating SPPs or on LSPRs. Because of the evanescent character of the field perpendicularly to the metal surface, SPPs are extremely sensitive to the refractive index modification in the surrounding medium. This refractometric effect is the basic mechanism for SPP sensing. An analyte is introduced in proximity to the metal surface and any weak modification of its composition changes the refractive index accordingly, an occurrence that can be detected by the perturbations induced in the optical properties of

the SPP. The analyte can also react with the recognition element of a functionalized surface by binding events. In general, SPP sensing can be based on different approaches that also modulate the coupling wavelength, the coupling angle, or the light intensity to increase the sensitivity [161]. LSPR sensing, in contrast, exploits the shift in the localized resonances of metal nanoparticles due to the presence of molecules in their electromagnetic hotspots. Compared to SPPs, LSPR sensing requires a more complex (nanostructured) surface but a simpler optical setup (no need for evanescent light coupling to the SPP modes), whereas, in terms of performance, the two approaches tend to achieve similar results [162].

The main advantages of plasmon-enhanced sensing are the high sensitivity (resonance shift measured in nanometers per refractive index unit, nm RIU^{-1}), the linearity between the input and the output signals (for reasonably large variations of the refractive index), the high resolution (measured in RIU), and the low limit of detection [161]. The sensitivity is generally defined as the ratio between the change in the sensor output (in our case, the value of the resonance frequency λ_R) and the change in the environmental refractive index n_b of the molecular analyte, which can be casted as

$$S = \frac{\partial \lambda_R}{\partial n_b} = \frac{\partial \lambda_R}{\partial n_{eff}} \frac{\partial n_{eff}}{\partial n_b},$$

where n_{eff} is the effective refractive index probed by the SPP and n_b is the refractive index of the analyte molecules binding to the recognition element. $\partial \lambda_R / \partial n_{eff}$ depends on the experimental configuration, whereas $\partial n_{eff} / \partial n_b$ takes into account the refractive index profile as molecules at different locations will impact n_{eff} differently. An FOM can then be defined to characterize the SPR sensitivity as the ratio between the sensitivity S and the full-width at half-maximum (FWHM) of the plasmonic resonance:

$$\mathrm{FOM} = \frac{S}{\mathrm{FWHM}}.$$

Indeed, the narrower the plasmonic resonance is, the easier it is to detect a resonance shift. This is why developing extremely narrow plasmonic resonances has become a crucial issue for high-sensitivity biosensors. This narrowing can be obtained using LSPRs and specifically exploiting Fano resonances [64, 163, 164]. Fano resonances originate from the coupling between a continuum of states and a discrete narrow state and can be implemented in a plasmonic system featuring, for example, both a broad bright resonance and a narrower dark resonance. The interference between the two modes gives the resonance a typical asymmetric line shape [165, 166].

Commercial SPP sensing systems based on Au already exist. The field has been pioneered by Biacore AB Corporation since the 1980s, currently reaching concentration detections down to 1 pM [167]. Based on a prism coupling geometry, the system has a resolution down to 10^{-7}–10^{-8} RIU. In general, the large footprint of SPP sensing devices is a limitation that might, for example, be reduced by grating coupling configurations at the expenses of resolution. Recently, LamdbaGen Corporation commercialized a solution based on LSPR with femtomolar sensitivity [168]. All these approaches can also be developed with a spatial resolution allowing for multiplexing [169] and thus increasing the read-out throughput.

Plasmon-enhanced sensing is a very active field of research. Nonetheless, it is not straightforward to make a fair comparison among different systems because they are generally evaluated under different working conditions. The typical record values of sensitivity and resolution reported in the literature, for example, for a concentric circular grooves interferometer [170], plasmonic patches [171], periodic gratings [172], or nanodolmens [173] are in the range of 500–700 nm RIU^{-1} and the typical resolutions are of the order of 10^{-6} RIU. All these systems are exclusively based on Au. Hyperbolic metamaterials consisting of metal-insulator multilayers of few tens of nanometers have also been recently demonstrated, reaching a refractive index sensitivity above 10^4 nm RIU^{-1} and an FOM above 500 that originates from the excitation of bulk plasmon modes sustained by the metamaterial [174] (see also the discussion on hyperbolic metamaterials in Section 4.8). The sensitivity of all these refractometric approaches increases when moving deeper into the IR thanks to the stronger refractive index changes experienced by the sensor because of the molecular vibrational absorption lines in this spectral range.

In the mid-IR range, doped semiconductors offer the perspective of developing CMOS-compatible platforms for refractometric plasmonic sensing with integrated waveguides, sources, and detectors [175]. However, just a few and mainly theoretical proposals have been published at the moment. An SPR sensing configuration with a grating based on doped Si and a carrier concentration of 10^{21} cm^{-3} has been proposed and the geometrical parameters of the grating have been adapted to reach a perspective sensitivity above 10^4 nm RIU^{-1} [176]. Similar structures have also been combined with a thin Au layer. Here, the semiconductor grating is used to obtain an easier and more efficient coupling with the sensing Au layer [177]. The sensitivity obtained in this specific configuration is 3000 nm

RIU^{-1}. In the case of prism configuration, Ghosh and Ray introduced a very thin layer of undoped Si below or above the Au layer to increase the sensitivity of the sensor [178, 179]. This layer allows for a higher degree of confinement and enhancement of the electric field close to the Au layer, thus increasing the sensitivity. Finally, prism configurations with a thin layer of doped Si [180] or Ga-doped ZnO [181] have been experimentally investigated but without any evaluation of the respective sensing performance.

The most advanced experimental results in refractometric SPR sensing with doped semiconductors so far have been obtained exploiting LSPRs. The reported sensitivity values depend on the geometry of the plasmonic antenna and are of the order of 1–2 10^3 nm RIU^{-1} with ribbon arrays of InAsSb [159], pillar arrays of InAs [69], or plasmonic antenna arrays of InAsSb [138]. These values have been obtained for typical carrier concentrations of the order of 5×10^{19} cm^{-3} featuring a plasma wavelength of about 5.5 μm. All-semiconductor SPR sensing is at an infancy stage but based on recent works on Ge, Si, and III–V materials the opportunity to develop a monolithic integrated system is a clear advantage compared to classical SPR systems featuring a larger footprint.

4.2 Resonant SEIRA

IR absorption spectroscopy is a powerful tool to study molecules; however, because of the three orders of magnitude difference between the light wavelength and the molecule size, light-matter coupling is weak in this frequency range. This main limitation is circumvented using adapted spectroscopy techniques such as grazing incidence reflectance or attenuated total reflectance. These experimental techniques exploit a limited field enhancement that appears at the sensing surface upon reflection of an incident beam. Hartstein et al. [182] developed the same idea in the case of corrugated Au and Ag films. When light illuminates the corrugated metallic surface, hotspots appear due to LSP oscillations with high field enhancement. The light is focused at the nanoscale allowing for an efficient coupling with molecules adsorbed on the metal surface and thus increasing the light absorption by the molecules. This can be regarded as one of the very first demonstrations of SEIRA. The hotspots in this situation are randomly distributed not only spatially (according to the random roughness of the metal surface) but also spectrally, making it difficult to accurately control the experimental conditions and obtain reproducible results. In this context, the concept of resonant SEIRA employing nanoantennas was introduced recently to better control all these parameters and make SEIRA competitive with SERS spectroscopy [140]. This is achieved by spectrally tuning the localized plasmon resonances of the antennas to the frequency of the molecular vibrations.

To understand the mechanisms behind the SEIRA enhancement, we need to describe the coupling between the plasmonic resonance and the molecular vibration, as in a SEIRA experiment the weak molecular absorption is not probed directly but rather by considering the modulation it induces in the plasmonic spectrum. The coupled harmonic oscillator model is well adapted to mimic the Fano-like shape of the SEIRA signal [183]. It considers the "bright" mode of the plasmonic resonator, which is efficiently coupled to the far-field radiation by an arbitrary driving term, and the "dark" mode of the molecular vibration, which is weakly coupled to the far-field radiation. The two modes interact with each other by a coupling factor that allows transferring energy between them. This well-established model explains the observed Fano-like asymmetric line shapes as well as the observation of the electromagnetically induced transparency (EIT) that appears when both modes are in resonance [183]. However, the line shape modulation of the plasmonic resonance depends deeply on the plasmonic structure [184]. For example, it changes from EIT to electromagnetically induced absorption just by adjusting the long axis of a prolate spheroidal metal nanoparticle coated with a thin absorbing layer (Figure 11A). The mentioned coupled harmonic oscillator model cannot account for this behavior because it does not describe adequately the coupling between light and the plasmonic resonator. In other words, it is necessary to treat accurately the impedance matching between the plasmonic resonator and the incident light. To do that, an extension of the model has been proposed by considering the possibility of reflected or scattered waves (Figure 11B) [184]. The model uses the temporal coupled mode theory formalism [185, 186] to describe the Fano-like shape of the modulated plasmonic resonances. In this case, the driving term κ, which links the incident wave s_+ to the resonant mode, is not an arbitrary parameter, but rather it is directly related to the radiation rate γ_{Ae} because of the constraints imposed by the time-reversal symmetry and the energy conservation. Finally, the damping rate of the bright mode γ_A is the sum of γ_{Ae} and the intrinsic material absorption γ_{A0}. In this approach, the line shape modulation of the plasmonic resonance results from the interplay between the radiative and the nonradiative loss mechanisms and the role of the molecular absorption is to modulate this interplay. The absorption on resonance takes the following simple form: $A=\frac{4f}{(1+f^2)}$, where f is the ratio between γ_{Ae} and γ_{A0}. Figure 11C represents the absorption as a function

of f. The maximum value of the absorption corresponds to the so-called critical coupling condition ($\gamma_{Ae}=\gamma_{A0}$). If the internal damping rate dominates over the external damping rate, the resonator is undercoupled, which is the typical case for heavily doped semiconductor antennas in the mid-IR range, whereas Au antennas in the same spectral range are typically overcoupled as the external damping rate dominates over the internal damping rate. Adding a thin layer of molecules to this model increases the internal damping of the oscillator, which corresponds to a left shift of the absorption condition in Figure 11C. This model demonstrates the importance of considering not only the coupling between the antenna and the molecules but also the coupling between the antenna and the external radiation.

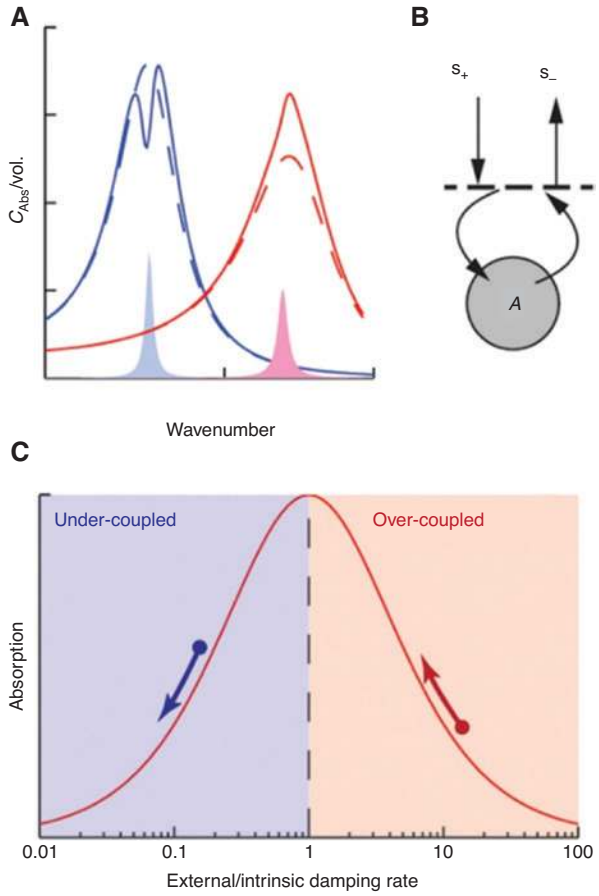

Figure 11: Mechanisms for SEIRA enhancement.
(A) Absorption cross-sections (C_{Abs}) normalized to the particle volume for Ag prolate spheroidal particles with two different lengths of the long semiaxis a (dashed curves). Solid curves show the same quantity for Ag particles coated with a 5-nm-thick shell of a model material exhibiting an absorption band aligned with the particle resonance (colored regions at the bottom). (B) Schematics of a single cavity (with a mode amplitude A) coupled to input (s_+) and output (s_-) waves through a single port. (C) Absorption of the Ag prolate spheroidal particles as a function of the ratio of the radiation rate γ_{Ae} to the intrinsic damping rate γ_{A0} [184]. Reprinted from [184] with permission, Copyright 2013 American Chemical Society.

Other efforts have been done along the same line, trying to understand the conditions that grant optimal SEIRA enhancement. In a recent paper, Neuman et al. highlight with both theoretical calculations and numerical simulations that the largest SEIRA modulation of the plasmonic resonance is achieved when the spectral maxima of absorption and scattering of the antennas are of similar magnitude. Moreover, they demonstrate that, under such circumstances, the vibrational fingerprint is exclusively a result of the scattering [187]. All the considerations reported so far highlight that the control of the different loss mechanisms in the antenna-molecule coupled system is a critical issue in the design of SEIRA platforms.

Once the models to describe the SEIRA effect are established, it is important to access a reliable and common parameter characterizing the SEIRA performance, i.e. to quantify an enhancement factor, which can, for example, be defined as

$$\mathrm{EF}=\frac{I_{\mathrm{SEIRA}}}{I_0}\frac{A_0}{A_{\mathrm{SEIRA}}},$$

where I_{SEIRA} is the enhanced signal strength from antenna-coupled molecules covering (filling) a surface (volume) A_{SEIRA}. This quantity is compared to the signal strength I_0 collected from bare reference molecules covering (filling) a surface (volume) A_0. To correctly evaluate the enhancement factor, one needs to accurately measure I_{SEIRA}, a task that can be performed following the procedure defined by Neubrech et al. [188], and to estimate A_{SEIRA}, which is, in general, an indirect assessment that can also be done via electromagnetic simulations. This last point has to be considered carefully to avoid any overestimation or underestimation of the enhancement. At this point, the reader should also be aware that, in any case, such enhancement estimation will hold only for those molecules that are located in close proximity of the plasmonic hotspots. Therefore, it is still a very relevant issue to achieve a proper delivery of the molecules to the antennas.

Experimentally, SEIRA has been mainly performed with Au antennas that sustain LSP modes in resonance with the frequencies of the molecular vibrations, exploiting either a single rod geometry, where the enhancement is further boosted by the lightning rod effect [140, 188, 189], or a double-rod geometry with the additional enhancement provided by the nanogap [190–192]. The combination of these three effects – localized plasmon resonances, lightning rod, and nanogap – allows reaching a high field enhancement,

which is a fundamental parameter for SEIRA. In the case of antennas, the maximum enhancement is obtained for a ratio between the frequency of the molecular vibration and the frequency of the plasmon resonance, $\omega_{vib}/\omega_{resonance}$, which has to be slightly smaller than unity [193]. Indeed, the total damping of the coupled molecular and plasmonic systems causes a redshift of the near-field enhancement [194]. A careful design of the antenna allows for an even better funneling of the light into a small gap, reaching an enhancement up to 10^7 [195], or the detection of fewer than 500 molecules of 4-nitrothiophenol [196]. However, realizing controlled nanogaps is not trivial and requires complex technological processes. Other designs avoid this challenge. For example, a so-called "perfect-absorber" geometry improves the coupling between the incident light and the antenna by positioning the antenna at a distance of a quarter of the wavelength from a back-reflecting mirror [17]. In the pedestal geometry, also, the impedance matching thanks to the lower refractive index of the surrounding combined to a larger active surface area allows increasing the SEIRA signal by nearly one order of magnitude compared to planar nanostructures [137, 197]. Moreover, collectively enhanced IR absorption exploits the collective plasmonic excitations created by tailoring the dipolar interactions in engineered nanoantenna arrays [189] and reaches an enhancement factor of up to 10^5. Finally, the material quality improves also the enhancement factor of the plasmonic resonance. This is, for example, the case for monocrystalline Au and aluminum where the technological process was improved and so were the plasmonic performance in the visible and near-IR parts of the spectrum [67, 198]. Along the same line, the high quality of doped semiconductors can be in perspective one of the premium features for SEIRA.

The first demonstration of SEIRA with doped semiconductors was reported for Si-doped InAs islands fabricated by nanosphere lithography, as already discussed in Section 3.7 (Figure 8A and B) [69]. The nanostructures are covered with a 50-nm-thick layer of polymethylmethacrylate (PMMA) by spinning (Figure 12A). The authors did not report the specific enhancement factor, which, however, can be roughly estimated to be about two orders of magnitude and is comparable to values reported in ribbon arrays of Si-doped InAsSb covered by a 200-nm-thick layer of PMMA [159]. Baldassarre et al. reported an enhancement factor of about 200 for the phosphorus-doped Ge plasmonic antennas of Figure 8C and D [60]. The antennas are coated with a thin layer of polydimethylsiloxane (PDMS) of less than 40 nm, which features a vibrational absorption resonance at about 800 cm^{-1} due to the Si-C bond stretching modes. The experimental spectra in Figure 12B demonstrate the spectral perturbation induced by the PDMS layer and the highest

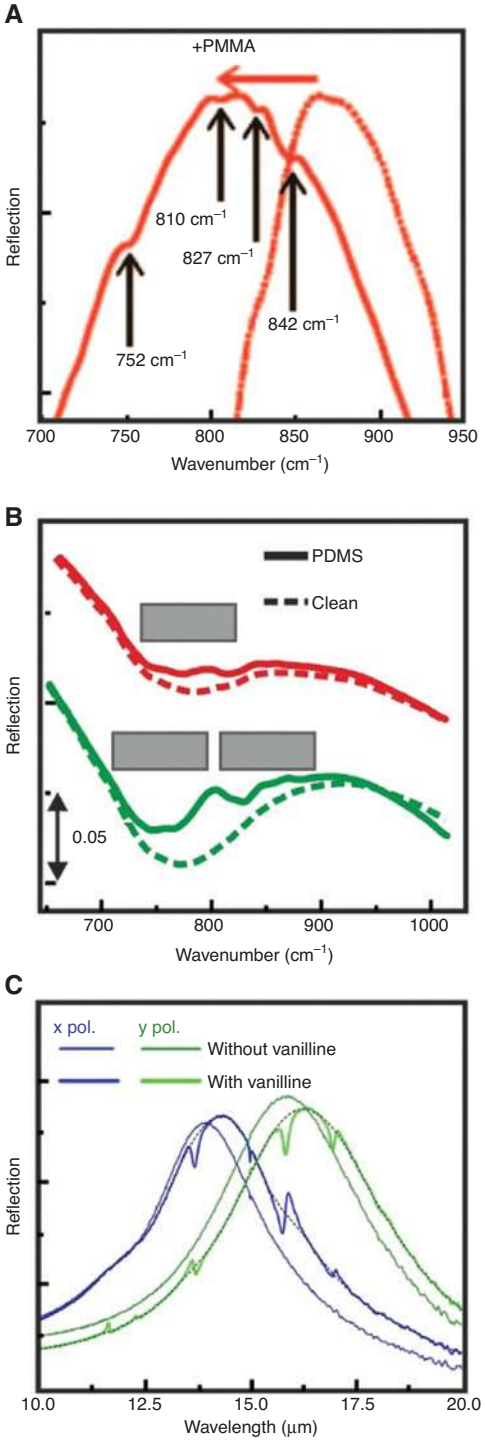

Figure 12: SEIRA spectra.
(A) SEIRA spectra (with and without PMMA) of Si-doped InAs islands fabricated on GaAs substrates by nanosphere lithography [69]. (B) SEIRA spectra (with and without PDMS for both single- and double-arm antennas) of phosphorus-doped Ge antennas fabricated on Si substrates by EBL [60]. (C) SEIRA spectra (with and without vanilline, comparing longitudinal and transverse electric field polarization) of InAsSb antennas fabricated on GaSb substrates by EBL [138]. (A) Reprinted from [69] with permission, Copyright 2013 American Chemical Society. (B) Adapted from [60]. (C) Adapted from [138].

enhancement that is achieved with a gap geometry compared to a single-rod geometry.

A significantly higher experimental enhancement of about 10^4 was reported for 2D plasmonic antenna arrays made of Si-doped InAsSb [138]. These plasmonic antennas have elliptical shape featuring strong anisotropy to polarized light. This allows addressing different spectral ranges when the electric field of the excitation beam is polarized along the long or short axis of the antenna (Figure 12C, thin curves). After drop casting of a vanillin film, the plasmonic antenna resonances redshift, and Fano-like features superimpose to the broad plasmonic response (Figure 12C, thick curves). For a given vibrational mode, the shape and the strength of the vibrational feature change depending on the polarization direction. Selecting different plasmonic modes for one antenna results in a modification of the coupling between the light, the plasmonic resonance, and the vibrational mode and accordingly of the enhancement factor.

These few findings are extremely promising because many geometries still have to be investigated by semiconductor plasmonics to reach the highest enhancement factors and the best coupling between the molecules and the antennas. Progresses in doping incorporation are also needed to reach the highest doping level and the highest SEIRA enhancement as recently discussed by Hsieh et al. [84] and demonstrated, for example, by Milla et al. [199]. The densification of the plasmonic antennas will also be an important issue to increase the signal-to-noise ratio as demonstrated experimentally [129] and theoretically [130]. Finally, semiconductor technologies allow for the fabrication of favorable sample geometries that would be almost prohibitive with metals. For example, as already mentioned, Pellegrini et al. recently demonstrated by numerical simulations that slit arrays in suspended heavily doped Ge membranes, which are well within the capabilities of Si foundry processes, allow for SEIRA enhancements that compare well (they are within the same order of magnitude) to those achieved with state-of-the-art Au slits [91]. This is achieved thanks to the possibility of getting rid of the detrimental effect of the proximity of high-index substrates that hinders the establishment of high-quality localized resonances.

4.3 Optically active plasmonic elements

When a photon with energy larger than the optical bandgap is absorbed by a semiconductor, an electron is excited to the conduction band and leaves an extra hole in the valence band. In the steady state determined by a continuous-wave illumination, on the one hand, such interband excitations result in a constant additional concentration of electrons and holes that adds up to the static doping of the material. Because of thermal effects that occur upon absorption and can damage the plasmonic structures, this possibility is usually limited to lower doping levels that allow covering only the far-IR (THz) range. In the case of short laser pulses, on the other hand, a transient ultrafast modulation of the carrier densities can be achieved. In this situation, a larger carrier concentration can be achieved and the whole mid-IR window becomes transiently accessible. Moreover, multiphoton absorption processes can also take place with ultrashort laser pulses and contribute to the total transient doping.

Some of the seminal works employing these effects for active IR plasmonics date back to 2006 with the demonstration of the optical control of SPPs propagating on an InSb surface, which is achieved by optically modulating the carrier concentration in the grooves of a surface Bragg mirror [133]. More recently, similar concepts have been applied to achieve the photogeneration of plasmonic antennas on an otherwise continuous semiconducting film by means of a patterned illumination that locally creates a larger and confined carrier concentration and allows for the realization of reconfigurable THz plasmonic devices [200–203]. Noticeably, the relatively low carrier concentrations required to achieve THz plasma frequencies also allow for the much simpler – although clearly much slower as well – control of the plasmonic material response by changing the temperature of the system and therefore directly modulating the thermal population in the conduction band [134].

Another way to indirectly exploit semiconductors for active THz plasmonics requires the realization of conducting metal antennas on a semiconducting substrate. Optical carrier excitation in the semiconductor is here exploited to tune the response of the metallic elements by changing their dielectric environment. In this context, tunable Cu and Au metamaterials coupled with active GaAs or Si semiconductors have, for example, been demonstrated [204, 205].

More recently, the concepts described above have been successfully translated from the THz to the mid-IR range. Ultrashort near-IR pulses have been used to optically induce a transient carrier concentration in the 10^{19} cm^{-3} range in a Ge wafer by a combination of one-photon absorption around the Γ point and two-photon absorption around the L point of the Brillouin zone. The Ge wafer thus acts as an ultrafast switchable plasmonic mirror, which was exploited to achieve subcycle slicing of intense mid-IR transients, as monitored directly in the time domain by electro-optical sampling [148, 206]. Subsequently, a similar setup was also used to trigger transient

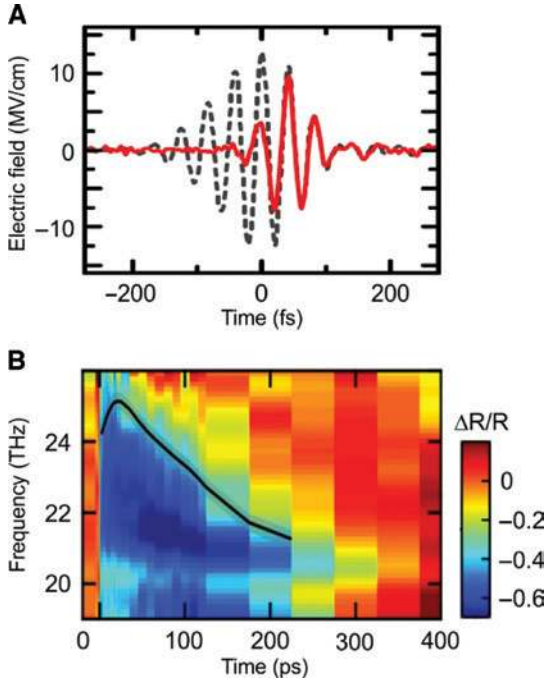

Figure 13: Transient excitation of plasmonic behavior.
(A) Temporal profile of the mid-IR probe electric field transmitted by an optically doped (red) or undoped (dashed line) Ge wafer, which allows achieving subcycle slicing of the ultrafast pulses [148]. (B) Spectrally resolved differential reflectivity of optically doped Ge antennas. The spectral changes over time and the superimposed black line highlight the establishment and the temporal redshift of the antenna resonance as the two optically injected electron and hole plasmas are created and then relax back to the unperturbed concentration [61]. (A) Adapted from [148]. (B) Reprinted from [61] with permission, Copyright 2016 American Physical Society.

localized plasmon resonances in otherwise undoped Ge antennas fabricated by EBL on a Si substrate as demonstrated in Figure 13 [61]. This approach gives full control over the enhancement and confinement of mid-IR radiation within subdiffraction volumes and on an ultrafast timescale for the all-optical manipulation of nanoscale mid-IR devices. It is important here to stress that exploiting interband optical excitations to achieve a high level of transient carrier population always implies that both electrons and holes (with the respective different scattering rates and effective masses) are generated concurrently and that therefore the response of the device can be modeled and understood only if the combined response of both plasmas is taken into account [61].

4.4 Electrically active plasmonic elements

The ability to monitor and control electrically the optical properties of a system is one of the main objectives of the optoelectronics community. However, not all optical systems are electrically active. As a relevant example in the context of plasmonics, the carrier density in noble metals is so high that the achievable modulation is often weak. In the case of doped semiconductors, in contrast, the accumulation and depletion of charges is one of the most common processes that are ordinarily exploited for microelectronic components and that can be used to tune the plasma frequency of the material. Nevertheless, the ease of operation depends directly on the targeted carrier density so that, although the electrical modulation of the plasmonic properties of doped semiconductors is certainly possible in the THz range, it is much more challenging in the mid-IR. The process requires applying a voltage at the extremities of a structure featuring a potential barrier, thus determining an inhomogeneous charge accumulation that typically extends for a few tens of nanometers. However, a carrier density beyond 10^{19} cm^{-3} is required to access the mid-IR range. Although, as discussed before, it is possible to generate optically such a high carrier injection [61], reaching the same densities electrically would require high voltages with an extremely inhomogeneous distribution. This is one of the main reasons why the direct electrical modulation of the plasmonic properties of heavily doped semiconductors has been essentially achieved in the THz range, whereas the mid-IR range has been approached only with more complex and somehow indirect solutions. These typically include exploiting the refractive index variation by the carrier modulation in the semiconductor to tune the dielectric environment of a metallic plasmonic device, which was already discussed previously in the context of all-optical modulation but can be achieved by electrical means as well. Moreover, to circumvent the inhomogeneity issue, it is possible to use quantum wells, often with waveguided and optical cavities approaches that increase the light-matter interaction.

Electrically active THz devices based on Au plasmonic layers on GaAs substrates have been first demonstrated more than 10 years ago in a few seminal publications by Chen et al., including the active tuning of metamaterial arrays [207] and the electronic switching of the extraordinary THz transmission through a subwavelength hole array [208]. In the investigated devices, the metal film deposited on a 2 μm n-doped GaAs layer with a carrier density in the 10^{16} cm^{-3} range creates a Schottky junction that can deplete the n-doped GaAs layer close to the Au electrode by applying a reverse voltage bias. The control of such applied bias, and therefore of the accumulated charges, achieves a modulation of the transmission through the metamaterial or through the hole array of up to 50% (Figure 14).

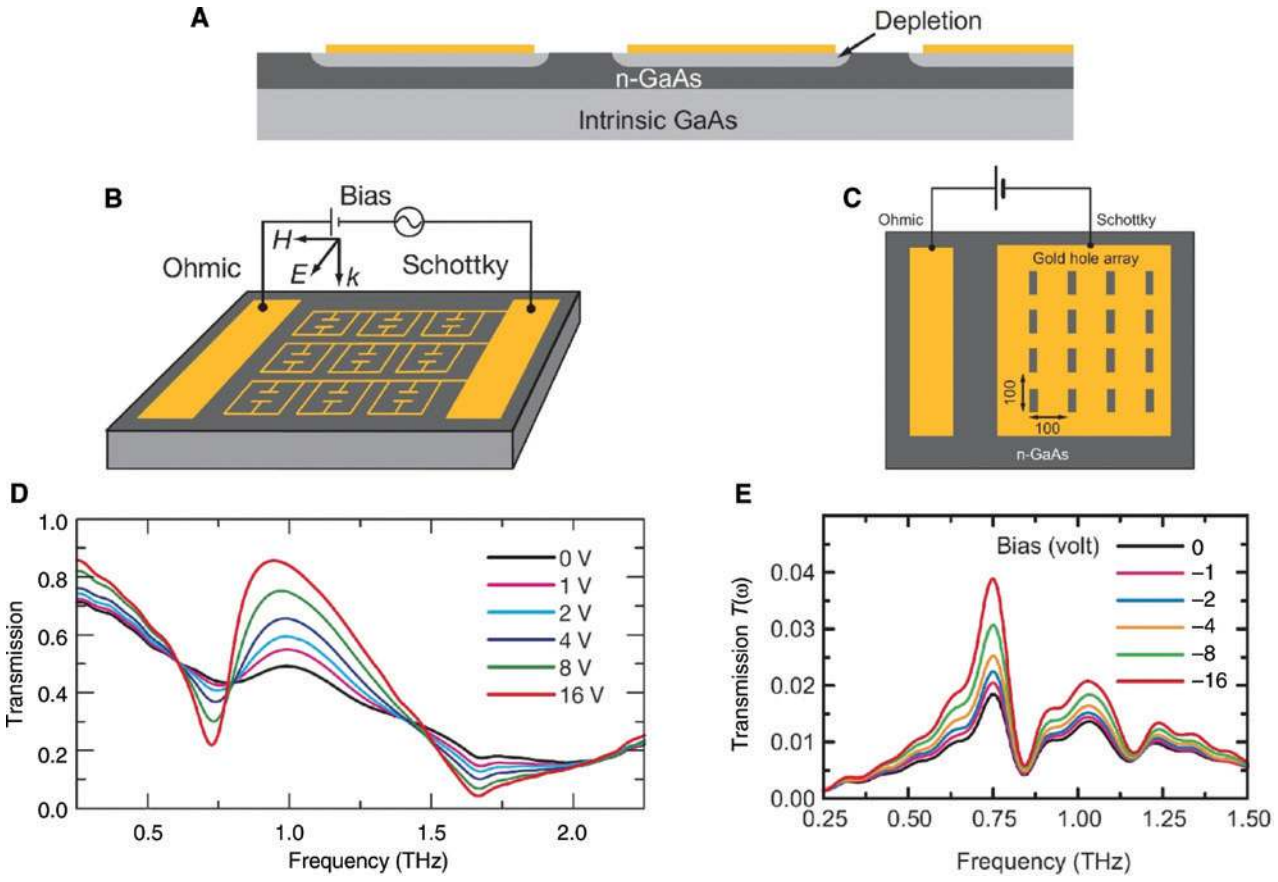

Figure 14: Electrically-active devices in the THz spectral range.
(A) Cross-sectional view of structures showing the depletion regions under reverse voltage bias. (B and C) Schematic design of the metamaterial arrays (B) and the metal hole arrays (C) exhibiting an electronically switchable extraordinary THz transmission. (D and E) Corresponding THz intensity transmission spectra for the metamaterial arrays (D) and metal hole arrays (E) as a function of the applied reverse voltage bias [207, 208]. (A, C and E) Adapted from (2008). (B and D) Reprinted from (2007) with permission, Copyright 2006 Springer Nature.

An efficient alternative for active plasmonics in the THz spectral range is also represented by 2D electron gases (2DEGs) as predicted by Diakonov and Shur [209, 210]. The possibility to control the plasma waves created inside the 2DEG of a ballistic field effect transistor has led to many demonstrations of both THz detection [211] and emission [212]. The degree of control of these peculiar plasmonic modes is so high that it is possible to couple coherently the localized plasmonic excitation with a finite 1D THz plasmonic crystal [213] or to achieve tunable EIT thanks to the complex interplay between a finite plasmonic crystal, plasmonic defects, and Tamm states (weakly localized crystal surface states with a complex rather than purely real Bloch wavevector) [214]. Few demonstrations of electrically tunable plasmonic properties based on semiconductor quantum wells have also been obtained in the mid-IR range. They are generally based on a 2DEG undergoing intersubband transitions, i.e. the electronic transition between two quantized levels of the quantum well. Adjusting electrically the carrier density in the quantum well allows activating the intersubband transition due to the subband filling. Furthermore, the related absorption peaks shift as the carrier density changes. This renormalization of the intersubband transition energies arises from the dipole-dipole Coulomb coupling with the 2D plasmons in the quantum wells [215]. The specific use of these 2D plasmons is detailed in Section 4.9.

The level of control of quantum well structures based on semiconductors that support 2DEGs is at present very high. Over the last decade, however, 2D layered materials, graphene in particular, have also emerged as a very promising perspective thanks to their superior optical and electrical properties. The propagation of mid-IR SPPs on graphene was first demonstrated in 2012 [17, 18], but the first applications were limited by the low material quality and strong plasmon damping. As the technology rapidly

progressed, the introduction of graphene-boron nitride heterostructures, in which the graphene sheet is sandwiched between two films of hexagonal boron nitride, paved the way toward low-loss plasmons whose quality is fundamentally limited by phonons [216]. The propagation length can be further improved by going to cryogenic temperatures, thus reaching a fundamental limit in which the main contributing factor is represented by the losses in the encapsulating films [217]. Compared to 2DEG in quantum wells made of conventional semiconductors, graphene has the advantage of lower phonon losses and of a surface field concentration that is beneficial for sensing applications [218]. It also enables for the gated electrical control [17, 18, 219] and the all-optical control [220] of the carrier densities and therefore of the resonances, with the possible perspective of integration into CMOS devices [221]. In contrast, the main limitation today seems to be the difficulty in achieving a large-scale production of high-quality material, which is fundamental for any further development.

The combination of optical and electrical functionalities paves the way toward a higher degree of integration. As an example, Li and Ning have introduced an all-semiconductor integrated active plasmonic system [222]. Using an InAs substrate platform, they combine active sources, waveguides, and detectors on a chip. This can be achieved in a single epitaxial growth process with GaSb or AlSb alloys that can be lattice matched to the InAs substrate. Applying a voltage can accumulate charges in the InAs layer and sustain SPPs. However, the proposed design will be limited by the broken-gap band alignment between InAs and GaSb, a structure with the InAs conduction band edge lower than the GaSb valence band edge, allowing for a current flow across the heterojunction [223] that hampers charge accumulation. This drawback might be circumvented, for example, with InAs/AlAsSb heterojunctions. Another limitation of the design is the large inhomogeneity of the charge profile that broadens the SPP resonances.

Recently, the field-effect spatial control of mid-IR plasmon resonances has been demonstrated at 10.5 μm wavelength in an InAs nanowire grown by Au-assisted chemical beam epitaxy. A highly inhomogeneous carrier distribution along the nanowire axis (ranging from 10^{16} to 10^{18} cm^{-3}) is spatially modulated through gating, resulting in a spatial shift of the localized plasmonic hotspot that is imaged with a scattering-type scanning near-field optical microscope [152].

At present, however, the main experimental demonstrations of electrically tunable mid-IR plasmonic devices that include doped semiconductors do not directly exploit the plasmonic properties of the semiconductor but rather the refractive index variation involved by the free carrier modulation [224, 225], as already discussed previously for the THz range. The concept was first validated by statically varying the doping level in the 10^{16}–10^{18} cm^{-3} range during the growth of a GaAs [226] or an InSb [227] semiconductor substrate on which an Au hole array was deposited allowing for extraordinary transmission of about 10 μm wavelength. Because varying the doping in these proportions determines a larger refractive index change for InSb than for GaAs, their respective resonances blueshift by 123 and 23 cm^{-1}, respectively.

The electrically tunable counterparts were demonstrated on GaAs/AlGaAs heterojunctions [224, 225] and use two different physical mechanisms (Figure 15). In the first demonstration [225], the current flowing in an n-doped layer between two electrodes causes a temperature change that increases the internal losses and accordingly decreases the transmission through a metal hole array. A second demonstration of electrically tunable plasmonic resonances based on the same material platform was obtained with Au split-ring resonators fabricated onto a 10-nm-thick GaAs quantum well sandwiched between two AlGaAs barriers [224]. A 10% change in the transmission of the fundamental resonance of the split rings was measured as a consequence of the shift caused by a carrier-induced change in the refractive index of the material underneath.

Although promising, electrically tunable structures based on semiconductor plasmonics still miss a convincing demonstration. The few experimental realizations show poor performance and are essentially based on refractive index changes induced by carrier or temperature change. Future developments might leverage on further improvements in the coupling between plasmonic structures and quantum wells to ensure strong enough modulation [224, 228–230] and on the exploitation of waveguide geometries to increase the interaction volume, as envisaged in the original PlasMOStor proposal (metal-oxide Si field-effect plasmonic modulator) operating in the visible and near-IR [231].

4.5 Waveguiding

Standard dielectric waveguides are characterized by a sharp cutoff for all the propagating modes and can be employed to distribute optical signals only as long as the dimensions of their lateral cross-section are of the order of λ/n (with n being the refractive index of the waveguide material) or larger. Plasmonic waveguides, on the

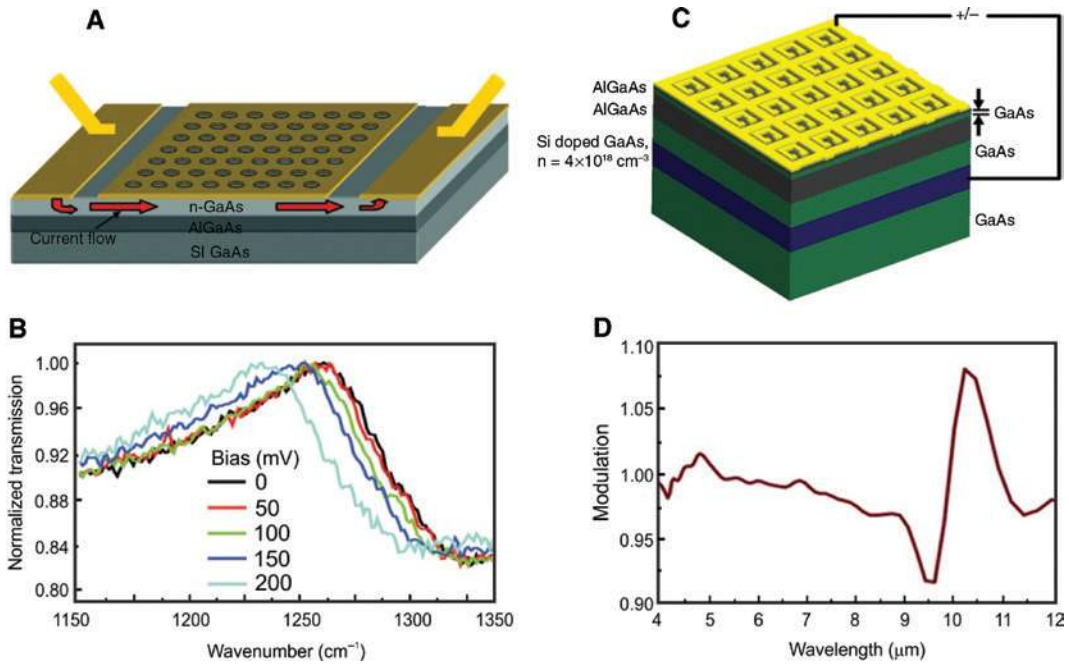

Figure 15: Electrically-active devices in the mid-IR spectral range.
(A) Sketch of the GaAs/AlGaAs device demonstrating thermal modulation of the extraordinary transmission through an Au hole array [225]. (B) Normalized transmission spectra of the device sketched in A as a function of the applied bias. (C) Sketch of the GaAs/AlGaAs device demonstrating the electrical modulation of the mid-IR transmission through an array of Au split-ring resonators [224]. (D) Modulation spectra (defined as the ratio between the spectral response at positive and negative bias) of the device sketched in C. (A and B) Reprinted from [225] with permission, Copyright 2007 AIP Publishing. (C and D) Reprinted from [224] with permission, Copyright 2012 AIP Publishing.

contrary, possess the unique feature of an extreme subwavelength field confinement in the plane perpendicular to the direction of propagation. Indeed, the fundamental modes in metal nanowires and metal-insulator-metal gap waveguides display no cutoff when the cross-section of the waveguide is reduced even down to the nanometer scale [232–234]. Along this line, the adiabatic tapering of the cross-section in plasmonic waveguides has been proposed as a means to achieve superlocalization into a specific hotspot [235]. However, such opportunities come with the usual trade-off imposed by the large losses that inevitably accompany the field confinement. For these reasons, on the one hand, plasmonic waveguides have been introduced as a way to merge the speed of photonics with the typical footprints of microelectronics and to target enhanced molecular sensing. On the other hand, their development has been partially hindered by the fact that the typical propagation length of plasmonic modes is often only of a few wavelengths. Longer propagation lengths can be achieved at the expense of a lower degree of field confinement, for example, with the so-called dielectric-loaded plasmonic waveguides. Generally speaking, waveguides are a crucial building block for on-chip mid-IR sensors [175]; therefore, the perspective provided by plasmonics to implement them over a small footprint is clearly appealing.

Indeed, after the many original proposals in the visible and near-IR spectral regions, metal waveguides have also entered the realm of mid-IR plasmonics, although not yet extensively. Here, the low losses of Au allowed, for example, for the experimental demonstration of light propagation and nanofocusing in two-wire transmission lines [236] and for the effective implementation of dielectric-loaded waveguides in a lab-on-a-chip sensing platform, featuring integrated quantum cascade sources and detectors [237]. Heavily-doped semiconductors have been used in the mid-IR as cladding layers by decreasing their refractive index to confine the electromagnetic wave in the active region of a quantum cascade laser [238–240]. Mid-IR plasmonic waveguides made of heavily doped semiconductors have also been proposed; however, most of the works report only simulation results so far. Such designs include Ge and GeSn stripe waveguides [241], Si two-wire transmission lines [242], Ge-on-Si dielectric-loaded waveguides [243], and V-shaped grooves in InSb [244], although the latter have been investigated only in the THz regime. The simulation results in Figure 16, which have been obtained with a finite-difference eigensolver

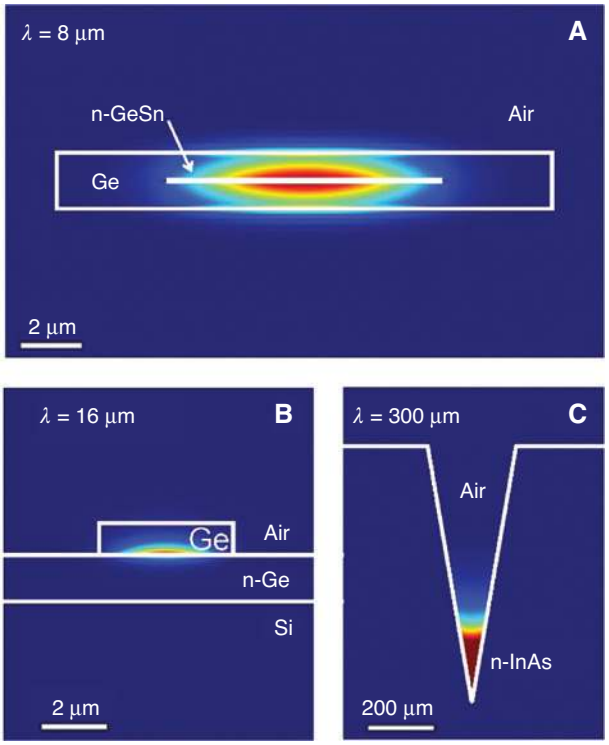

Figure 16: Simulations of semiconductor plasmonic waveguides. (A) n-doped GeSn stripe embedded in a Ge waveguide achieving subdiffraction mode confinement at 8 μm wavelength (geometrical and material parameters taken from Ref. [241]). (B) Dielectric-loaded plasmonic waveguide operating at 16 μm composed of an undoped Ge stripe on top of a n-doped Ge film on Si (geometrical and material parameters taken from Ref. [243]). (C) n-doped InAs V-shaped groove for the waveguiding of THz radiation at 300 μm wavelength (geometrical and material parameters taken from Ref. [244]).

in the frequency domain employing the same material parameters and the same geometries as in Refs. [241, 243, 244], demonstrate the fundamental plasmonic modes supported by such heavily-doped waveguides.

It should be noted here that, although the use of semiconductor plasmonic waveguides may be confined to a few selected sensing applications, the same undoped semiconductor materials, Ge and SiGe in particular [3, 245–247], are the preferred choice for standard dielectric waveguides in the mid-IR. This already motivates the presence of such materials in the pipeline of the foundry processes for on-chip mid-IR photonics and represents therefore a further incentive in using the heavily doped version of the same materials for plasmonic sensing antennas and metasurfaces. A hybrid semiconductor-metal design, resembling that of dielectric-loaded waveguides, in which a thin metal stripe is inserted in a dielectric high-index waveguide, has also been introduced for mid-IR wavelengths [248, 249].

4.6 Nonlinear optical conversion

Over the last decade, plasmonics has also become a fundamental asset to boost nonlinear optical effects. Nanoscale nonlinear sources will find application for the optical processing in integrated photonics, the generation of photons for quantum information devices, and the novel nonlinearly enhanced optical sensing schemes. As nonlinear photon-photon interactions are extremely weak, two ingredients are often combined to achieve a large conversion efficiency in macroscopic systems: high powers, requiring pulsed laser sources to keep thermal damages under control, and long interaction paths, for which phase-matching engineering in nonlinear crystals is usually employed. At the nanoscale, the reduced interaction volume provided by the nanostructures requires an additional boosting mechanism, which is usually found in the presence of localized resonances. The extreme local field enhancement provided by plasmonics has thus been employed to compensate for the reduced interaction volume and to realize coherent nanoscale light sources. Among the nonlinear effects that have been demonstrated in the visible and near-IR spectral regions, plasmon-enhanced second-harmonic generation (SHG) [250, 251], third-harmonic generation (THG) [252], and four-wave mixing [253] are the most common ones, but higher-order effects have also been reported [254, 255].

In the mid-IR, the field of nonlinear plasmonics is still in its infant stage. SHG has been reported in an Si-organic-metal waveguide supporting hybrid plasmonic modes [256] and Au plasmonic metamaterials have been employed to improve the nonlinear coupling of mid-IR light with quantum wells [257]. However, in such examples, the nonlinear conversion does not rely on the intrinsic nonlinearity of the plasmonic material rather mainly on that in the polymer for the first case and in the quantum well for the second case. More recently, mid-IR semiconducting antennas made of heavily doped Ge have demonstrated genuine plasmon-enhanced THG [143]. Ge antennas with a carrier concentration of about 2.5×10^{19} cm^{-3} and a corresponding plasma wavelength of about 9.7 μm were fabricated by EBL. In the experiment, the antennas were excited with ultrashort mid-IR pulses generated via difference frequency mixing and coupled to a confocal microscope based on reflective optics for single-antenna measurements. The efficiency of THG for different arm lengths demonstrates a clear maximum when the antenna is tuned to the fundamental wavelength of the excitation pulses; therefore, localized plasmon resonances are excited (see Figure 17). In this case, the nonlinear emission originates directly from the intense fields

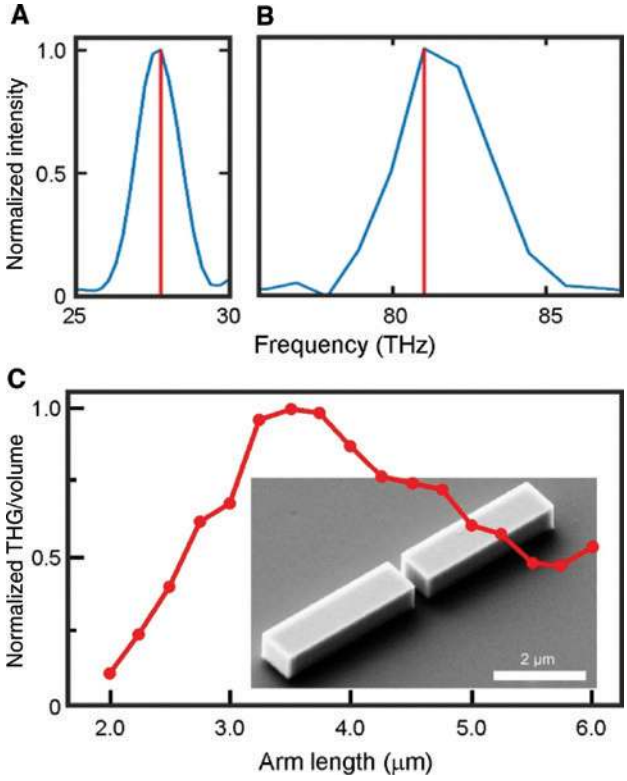

Figure 17: Nonlinear frequency conversion with semiconductor plasmonic antennas.
(A) Spectrum of the mid-IR excitation pulses employed for THG. (B) Spectrum of the emitted THG photons. (C) THG efficiency (collected THG intensity per unit antenna volume) as a function of the arm length of the plasmonic antenna, demonstrating maximum efficiency for a length of about 3–4 μm that corresponds to resonant excitation (inset, SEM image of one of the investigated antennas).

inside the Ge antenna arms. In this respect, besides the plasmonic enhancement, the large third-order nonlinear coefficient in Ge [258] certainly plays a fundamental role in the observed high conversion efficiency.

Generally speaking, mid-IR nonlinear plasmonics with doped semiconductors, besides providing a building block for the on-chip integration of nanoscale nonlinear functionalities, represents an exciting platform for fundamental studies in light-matter interaction and to address the possible role played by the intrinsic nonlinearities of the plasma oscillations in such processes.

4.7 ENZ phenomena

In the attempt to continuously improve the coupling between light and subwavelength objects, recent approaches introduced the use of ENZ materials, i.e. materials with vanishingly small dielectric permittivity [259, 260]. This small value of the permittivity has the consequence to extend the local wavelength and to dramatically homogenize the electromagnetic field inside the material. In the case of lossless ENZ materials, for example, theoretical work demonstrated that light can be squeezed through extremely narrow subwavelength channel structures [259].

A simple way to obtain ENZ materials is to work close to the longitudinal mode of a polaritonic system sustaining, for example, phonon polaritons, plasmon polaritons, or exciton polaritons. Indeed, at correspondence with the excitation frequency of such longitudinal modes, the real part of the permittivity is zero. However, to use efficiently such ENZ effect, the splitting between the longitudinal and transverse polaritonic modes has to be large enough and adjustable, i.e. it must be possible to tune and control the ENZ frequency. Phonon-polariton systems do not possess this feature and exciton-polariton systems have limited longitudinal-transverse splitting with the exception of dye molecules that demonstrated ultrastrong coupling [261]. In metals, intrinsic ENZ effects are hindered by the presence of interband transitions that dramatically increase the associated losses. From all these points of view, heavily doped semiconductors represent the ideal material platform to benchmark and exploit ENZ phenomena, as they possess a highly tunable plasma frequency that can be controlled by doping and can be spectrally located away from any electronic or vibrational absorption of the material to keep losses as low as possible.

When the ENZ materials are employed in the form of thin waveguiding layers, their ENZ mode splits into two modes that, for symmetry reasons, are very differently coupled to radiation. The radiative ENZ mode, which is also referred to as the Brewster mode, has first been observed in transmission experiments through a thin Ag foil [98] and its dispersion relation has been studied more recently by reflectance experiments in thin Si-doped InAsSb films [92]. This is an optical leaky mode that appears in thin layers at a frequency slightly higher than the screened plasma frequency. It can also be used to monitor optically the doping level of doped semiconductor layers. At a frequency slightly smaller than ω_{p*}, a second mode, which corresponds to the symmetric plasmonic mode sustained by a thin metallic layer, appears [92]. This second nonradiative guided mode is the ENZ mode typically used in the literature to develop optical devices [74, 262]. Campione et al. observed the nonradiative ENZ mode in a thin indium-tin oxide (ITO) layer deposited on a glass substrate in an evanescent excitation configuration [100].

Transparent conducting oxides such as ITO or AZO [263] are especially suitable for ENZ applications in the visible and near-IR range but suffer from large losses

because of their poor crystallinity. They have been employed, for example, to demonstrate ultrafast all-optical modulation at telecommunication wavelengths thanks to their large optical nonlinearity [75, 264]. Working with conventional semiconductors, in contrast, represents a highly promising opportunity for the mid-IR spectral region and for applications where losses are especially detrimental.

The peculiar ability of ENZ materials to favor light funneling into subwavelength apertures and channels was exploited by Adams et al. to boost the transmission of a slit in an Au film deposited onto an ENZ InAsSb layer [265]. The heavily doped InAsSb film was grown by MBE onto a GaAs substrate and the excitation of the ENZ mode was demonstrated to improve the TM transmitted light through the slit. Similar approaches have been developed exploiting metallic gratings or metamaterial arrays to favor the coupling between light and the ENZ mode in a thin semiconductor layer. Figure 18 represents the normalized near-field distribution $|E_z|^2$ at the resonance (34.3 μm) for a p-polarized plane wave incident at 15° on a hybrid metal-semiconductor structure featuring an Au grating on top of a AlGaAs/GaAs/AlGaAs quantum well. The Au grating allows coupling the light with the ENZ phonon-polariton mode of the 22-nm-thick GaAs well. When a voltage is applied between the bottom of the structure and the Au grating, the quantum well is filled with or depleted of carriers and a modulation of the transmitted light is achieved thanks to the strong interaction of the incident light with the ENZ mode [262]. Similar ideas for optoelectronic modulation via ENZ modes have been developed with Au metamaterial arrays deposited on an n-doped GaAs layer [74]. Contrary to the previous situation, which exploited a phonon-polariton mode associated with the longitudinal optical phonon of the well material, here the use of plasmon-polariton ENZ modes improves the tunability of the optoelectronic device thanks to the control of its doping level.

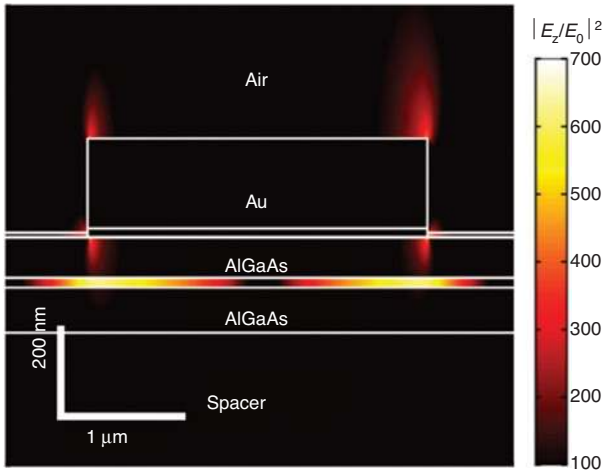

Figure 18: Normalized near-field distribution $|E_z|^2$ at resonance (34.3 μm) for a p-polarized plane wave incident on a Au grating structure coupled to a doped semiconductor quantum well, demonstrating the efficient excitation of the ENZ mode and the channeling of light into the thin absorbing layer [262]. Reprinted from [262] with permission, Copyright 2012 American Physical Society.

4.8 Hyperbolic media, negative refraction, and perfect absorption

Heavily doped semiconductors are also the ideal building blocks for so-called hyperbolic media thanks to the dielectric function tunability that they provide. Let us consider, for example, a stacked multilayer of a doped semiconductor (behaving as a conductor) and an undoped semiconductor (behaving as an insulating dielectric material) with their effective permittivity values $\varepsilon_{\parallel}$ parallel and $\varepsilon_{\perp}$ perpendicular to the plane of the stacked films, which can be calculated using the effective medium theory [266]. This uniaxial material gives the following dispersion relation:

$$\frac{k_{\parallel}^2}{\varepsilon_{\parallel}} + \frac{k_{\perp}^2}{\varepsilon_{\perp}} = \frac{\omega^2}{c^2},$$

where $k_{\parallel}$ and $k_{\perp}$ are the wavevectors of electromagnetic waves propagating along or perpendicularly to the layers. A detailed analysis of the permittivity values of the stacked structure needs to consider that $\varepsilon_{\parallel}$ and $\varepsilon_{\perp}$ can be either positive or negative. If both of them are positive, the isofrequency surface in the dispersion relation will be a sphere ($\varepsilon_{\parallel} = \varepsilon_{\perp}$) or an ellipsoid ($\varepsilon_{\parallel} \neq \varepsilon_{\perp}$). If both of them are negative, we have a metal. The hyperbolic behavior appears when $\varepsilon_{\parallel}$ and $\varepsilon_{\perp}$ have opposite sign. If $\varepsilon_{\parallel} < 0$, the hyperbolic medium is type I, whereas if $\varepsilon_{\perp} < 0$ the hyperbolic medium is type II. Hyperbolic media are characterized by an extremely large local density of states and can be exploited as negative refractive index materials. A representative example is demonstrated in Figure 19, where a structure constituted of alternating doped InGaAs and undoped AlInAs layers features an effective permittivity $\varepsilon_{\parallel}$ corresponding to a Drude-like behavior (metallic response for wavelengths longer than 12 μm; blue curve), whereas $\varepsilon_{\perp}$ reproduces the typical response of ionic crystals (phononic-like Lorentzian line shape; red curve) [268]. This system, therefore, features both a type I hyperbolic response (for wavelengths longer than 12 μm) and a type II response (Figure 19A, yellow colored region). This careful design of the stacking allows engineering

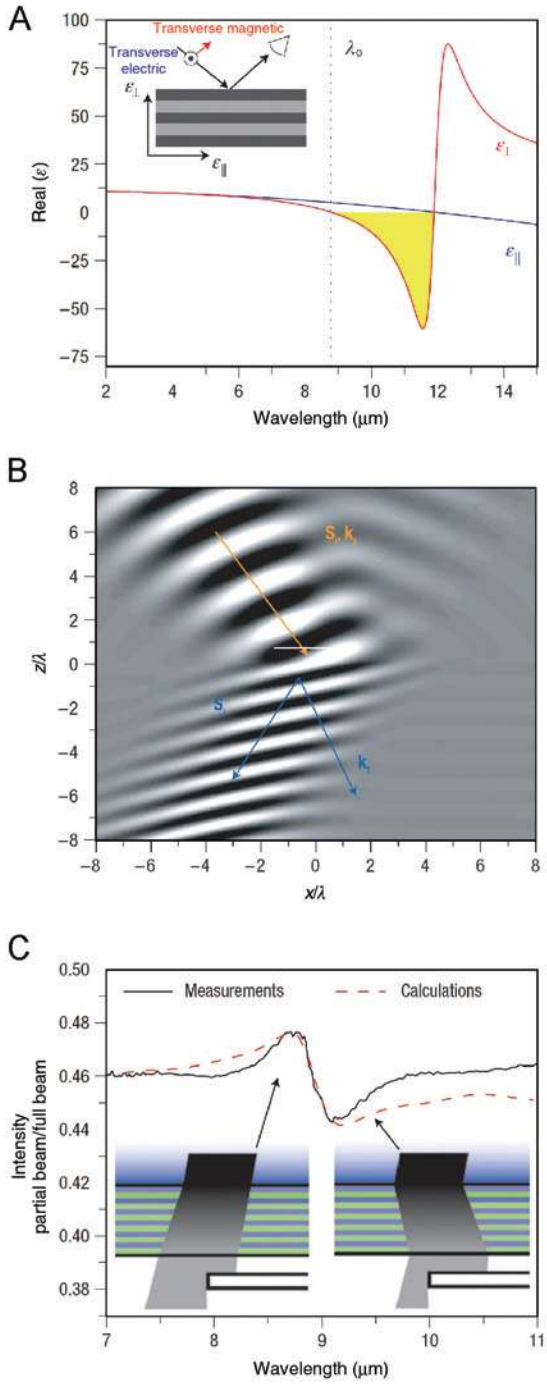

Figure 19: Negative refraction with semiconductor hyperbolic metamaterials.
(A) Calculated effective permittivities for a uniaxial hyperbolic material. The inset shows the relative orientation of the permittivity, the electric field vectors, and the layered structure. (B) Calculated negative refraction map for a monochromatic transverse-magnetic polarized Gaussian beam across an air-hyperbolic material interface. (C) Experimental demonstration of negative refraction by exploiting a blade along the detection path to translate the lateral beam displacements at different wavelengths into a modulation of the collected intensity [267]. Reprinted from [267] with permission, Copyright 2007 Nature Materials.

the optical properties of the system and realizing a negative index material, with which negative refraction at IR wavelengths can be achieved. Figure 19B demonstrates the results of numerical simulations achieving negative refraction with the system described in Figure 19A, whereas Figure 19C reports experimental results in which a blade in the detection path is exploited to translate the lateral beam displacement due to positive and negative refraction into a change in the collected intensity [267].

Similar demonstrations have been achieved with hyperbolic media based on Si-doped and undoped InAs grown on a semi-insulating GaAs substrate [38]. However, even simpler structures can demonstrate negative refraction properties. For example, perfect lensing is also possible with negative index materials [269]. To optically resolve subdiffraction objects, the superlens effect can be exploited with just a thin metal foil [270] thanks to the excitation of SPPs on its surface. However, the use of noble metals with their plasma frequencies in the UV range strongly limits the application of this concept and heavily

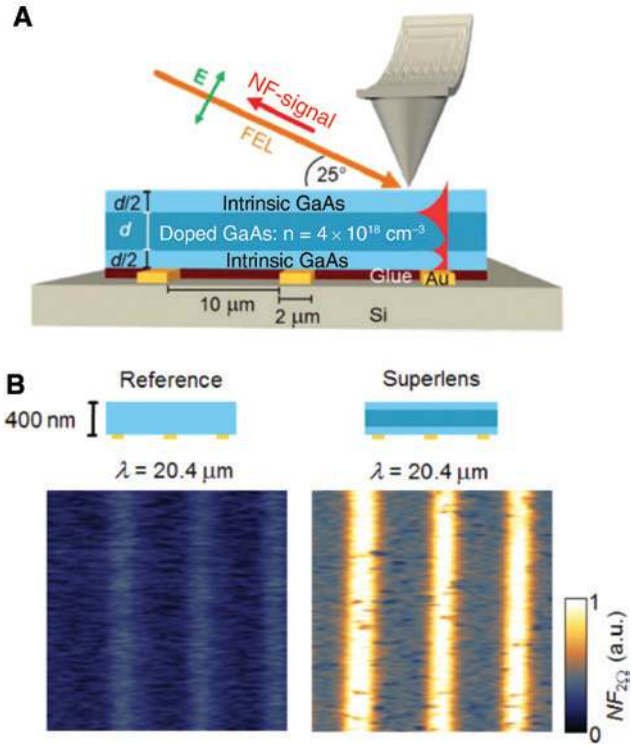

Figure 20: Superlensing with semiconductor plasmonics.
(A) Sketch of the s-SNOM investigation of a GaAs superlens illuminated by p-polarized free electron laser radiation. (B) Au stripes (width 2 μm and spacing 10 μm) are imaged through a 400 nm undoped layer of GaAs or a three-layer system of doped and undoped GaAs. Superlensing is demonstrated in the case of the layered system [271]. Reprinted from [271] with permission, Copyright 2015 American Chemical Society.

doped semiconductors can be used to cover a larger spectral range. A thin n-doped GaAs layer was, for example, employed to demonstrate superlensing in the mid-IR range using a scattering-type scanning near-field optical microscope illuminated by p-polarized free electron laser radiation as sketched in Figure 20A. The scattered light yields information about the local near-field at the upper GaAs surface. Au stripes (width 2 μm and spacing 10 μm) are imaged through a 400-nm-thick layer of undoped GaAs (reference sample) or through a three-layered system of doped and undoped GaAs (superlens sample) [271]. The experimental results in Figure 20B demonstrate that, in the case of the 400 nm undoped GaAs, the Au stripes image is blurred, whereas through the superlens system the stripes can be more clearly resolved. At $\lambda = 20.4$ μm, the stripes are imaged with a $\lambda/6$ subwavelength spatial resolution. This effect, which is mediated by the SPPs in the Drude-Lorentz material (Figure 20A, red features), can be adjusted spectrally by tuning the plasma frequency of the doped semiconductor.

It should be noted here, however, that the description of the hyperbolic stacking in terms of homogeneous dielectric constants, while being perfectly suited for the analysis of far-field propagating waves, fails to correctly describe the near fields of the system and the associated local density of states as discussed and demonstrated both theoretically [272] and experimentally [39]. Still, thanks to their modes with high wavevectors, hyperbolic

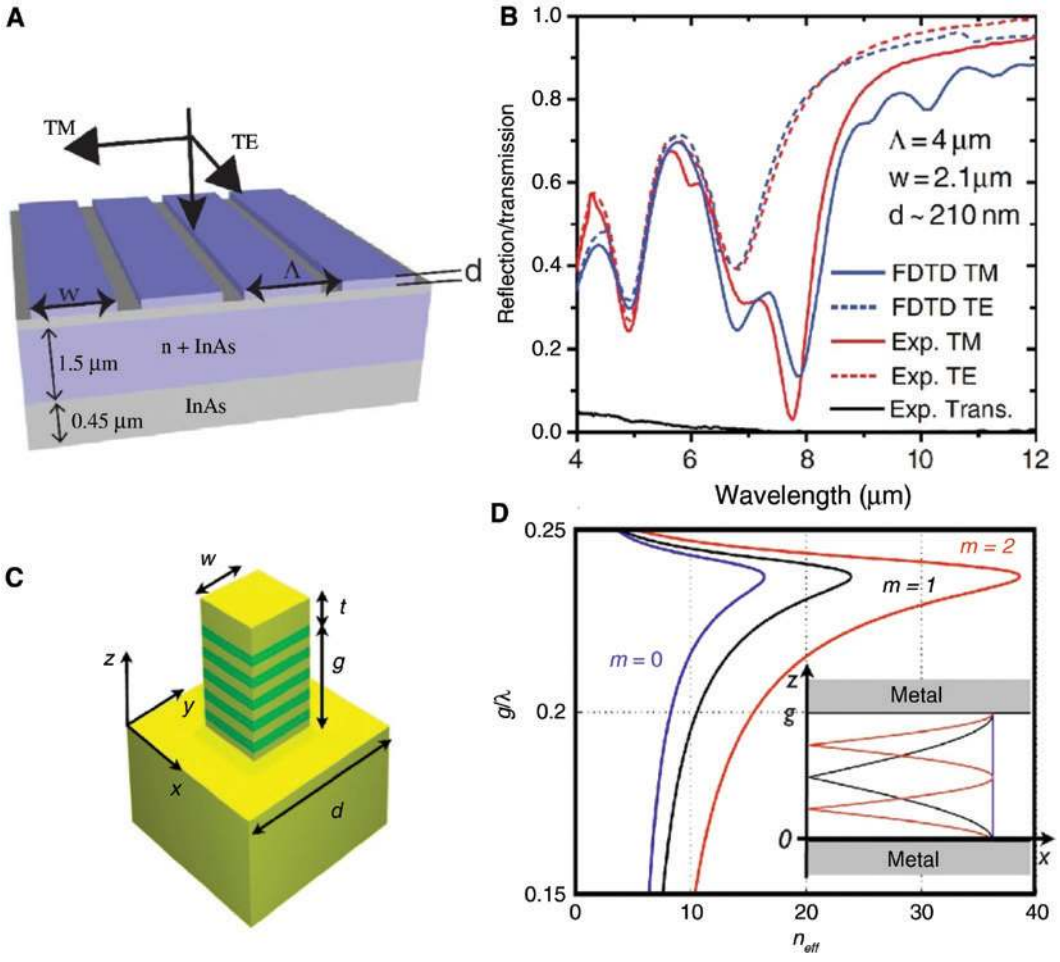

Figure 21: Applications of hyperbolic metamaterials.
(A) Sketch of the perfect absorber based on doped InAs [274]. (B) Experimental (red) and simulated (FDTD; blue) reflectivity for TE and TM illumination of the structure sketched in A, together with the experimental transmission (black), demonstrating perfect absorption of about 8 μm wavelength. (C) Schematics of the unit cell for a hyperbolic wire sandwiched between a metallic patch and a metallic substrate [275]. (D) Dispersion relation of the first three modes ($m = 0, 1, 2$) of the structure sketched in C as a function of the reduced frequency γ/λ, where γ is the stack thickness, demonstrating a mode index up to about 40. The inset represents the modulus of the magnetic field associated with the three lowest-order modes. (A and B) Reprinted from [274] with permission, Copyright 2014 American Physical Society. (C and D) Reprinted from [275] with permission, Copyright 2017 American Physical Society.

materials possess a naturally large effective index, which can be exploited to design patch antennas. Patch antennas consist of a metallic patch deposited onto a dielectric spacer and an underlying metallic mirror. This sustains a gap plasmon that originates from a Fabry-Perot resonance of the guided mode squeezed into the spacer. By tuning the spacer thickness and the patch size, even perfect absorption can be reached [273], as the metallic mirror prevents any forward transmitted light while the patch antenna cancels the reflected light by proper impedance matching. The entire incident power is thus concentrated into the gap and absorbed therein. Semiconductors offer a particular versatility in the design of perfect absorbers. This application of heavily doped semiconductors has been first demonstrated by Law et al. with undoped and Si-doped InAs grown on GaAs (see Figure 21A and B) [274]. It is also possible to extend the spectral range down to the THz by increasing the antenna size [276] and broaden the perfect absorption band using a variable patch size [277].

Smaali et al. suggested that the dielectric spacer in patch antennas can be replaced by a hyperbolic material to exploit its high refractive index value [275]. In this way, it is possible to achieve an extremely small footprint (Figure 21C) thanks to the very large effective index (up to 40 as demonstrated in Figure 21D) of the gap plasmon mode. This structure thus presents the interest of a large surface-to-volume ratio, which increases the active surface area for sensing applications. By decreasing the spacing between the patches, it is possible to exploit the funneling of the electromagnetic wave via vertical nanoslits into the gap plasmons within the spacer to obtain a universal design and realize a tunable perfect absorber from IR to microwave frequencies independently of the choice of the metals and the dielectrics [278]. This geometry can also be adapted to the THz range where, instead of exploiting nanoslits, it is possible to photogenerate patches in a top undoped layer to develop active THz plasmonic devices [279].

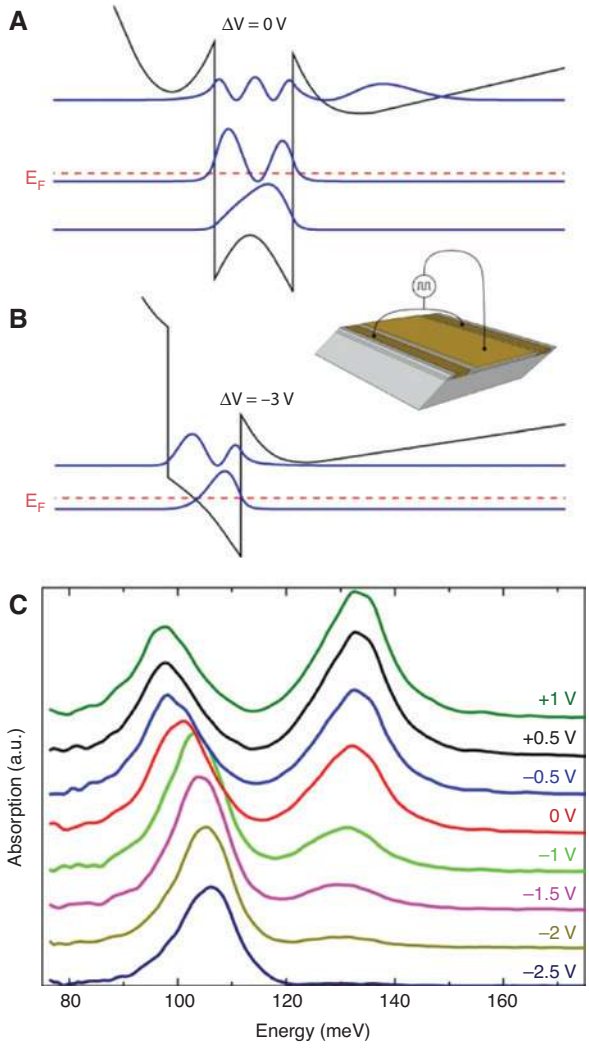

Figure 22: Intersubband excitations in quantum wells. Band diagram of a quantum well structure at 77 K as calculated with a self-consistent Schrödinger-Poisson solver at 0 V (A) and −3 V (B). The square moduli of the relevant wave functions are plotted as blue solid lines, whereas the Fermi energy is indicated by a red dashed line. The inset sketches the geometry of the device used to perform absorption measurements under the application of a gate voltage. (C) Absorption spectra measured at 77 K for different gate voltages [215]. Reprinted from [215] with permission, Copyright 2013 AIP Publishing.

4.9 Intersubband plasmons

The last application that we want to present in this review is the exploitation of intersubband plasmons. Intersubband excitations correspond to the electronic transition between two successive electronic states confined in a quantum well (Figure 22). Radiative transitions between such levels become possible only if electrons are injected electrically [215], optically [280], or chemically [281] into the first subband. In a doped quantum well, the collective excitation of a 2DEG confined in the ground state of a quantum well [282] gives rise to an intersubband plasmon whose energy depends on both the plasma frequency and the energy difference between two consecutive electronic levels. When the quantum well thickness increases, a multisubband plasmon appears because several subband are occupied leading to several intersubband plasmons that couple together through dipole-dipole Coulomb interactions [281]. The vanishing contribution of electron confinement when the quantum well thickness increases leads progressively to the classical bulk plasmon in a

semiconductor slab that is well described by the Drude model [283].

Intersubband plasmons open the possibility to develop agile devices, in which the energy of the resonances can be engineered by adjusting the quantum well thickness and the carrier density. This allows covering the whole mid-IR range. The intersubband plasmons can be coupled to metasurfaces to improve the light amplitude modulation [284, 285]. Additionally, the carrier density can be adjusted by applying a voltage to deplete or fill the quantum well [215]. Recently, intersubband plasmons demonstrated a nearly unitary emissivity with a structure consisting of GaInAs/AlInAS highly doped quantum wells grown by metal-organic CVD on an InP substrate. An electrical current is injected into the quantum well, and in the edge configuration, the intersubband plasmons efficiently emit light [286]. This is the consequence of the superradiance that occurs when a dense collection of two-level emitters oscillate in phase leading to an increase of the spontaneous emission rate [287].

5 Outlook and perspectives

We have reviewed the recent advances related to a new family of materials for plasmonics, namely conventional semiconductors such as Si, Ge, and III–V alloys. This recent field of research is at its infancy stage but benefits from 50 years of research in semiconductor technology in terms of growth techniques and technological processes. The high degree of control over the material properties and the related nanofabrication is a clear advantage for the future development of devices and their technological transfer.

The most advanced applications based on heavily doped semiconductor plasmonics are related to active devices and biosensing. Although the performance of amplitude modulation and the enhancement factors are still not optimized, many possible future paths have already been envisaged. The modulation of the amplitude of SPPs propagating along a waveguide can be improved by increasing the interaction of the SPP with the lossy material. In the case of biosensing, it is possible to address more complex antenna geometries, lightning rod effects, or gap plasmons to reach state-of-the-art enhancement factors for SEIRA sensing. Along this road, the development of reliable techniques to achieve extremely high levels of doping with low defectivity and full dopant activation is also a crucial step.

Moving forward, semiconductor-based metamaterials can boost further the current performance of plasmonic devices. Thanks to the high accuracy of epitaxy techniques, heavily doped semiconductors are the best-suited materials to exploit ENZ properties or create layered structures and realize hyperbolic materials in the THz and mid-IR spectral range. The ultimate situation here is represented by the possibility to confine carriers in quantum structures and reach an ultrastrong coupling between intersubband transitions and bulk plasmons. Finally, the ultrafast dynamic control at high frequencies of the plasmonic properties of heavily doped semiconductors can be realized optically, although many limitations still exist due to the required high fluences of the pump laser.

One can reasonably foresee a short-term technological transfer of heavily doped semiconductor plasmonics for active devices in the THz range because of the advanced control on the carrier modulation that is achieved in 2DEGs. Integrated solutions for biosensing are probably a longer-term vision. Even if efficient sources, detectors, and plasmonic biosensors are already available in the mid-IR range, further technological developments are needed to combine all these individual building blocks onto the same platform.

Acknowledgments: P.B. warmly acknowledges Leonetta Baldassarre, Daniele Brida, Marco Finazzi, Jacopo Frigerio, Vincenzo Giannini, Reuven Gordon, Giovanni Isella, Enrico Napolitani, Michele Ortolani, Douglas J. Paul, Giovanni Pellegrini, Marco Polini, Emilie Sakat, and Michele Virgilio for all the stimulating discussions and experiments on heavily doped semiconductors. The research leading to this work has received funding from the European Union's Seventh Framework Programme under Grant Agreement No. 613055, Funder Id: http://dx.doi.org/10.13039/100011102. T.T. warmly acknowledges Franziska Barho, Mario Bomers, Emmanuel Centeno, Laurent Cerutti, Fernando Gonzalez-Posada-Flores, Maria Milla, Chloe Nestor, Vilianne N'Tsame Guilengui, Stephane Lanteri, Guilhem Pacot, Jean-Baptiste Rodriguez, Eric Tournié, and Angela Vasanelli for the fruitful discussions and brainstorming in link with all-semiconductor plasmonics. This work was partially funded by the French "Investment for the Future" Program (EquipEx EXTRA, ANR 11-EQPX-0016, Funder Id: http://dx.doi.org/10.13039/501100001665), the French ANR (SUPREME-B, ANR-14-CE26-0015, Funder Id: http://dx.doi.org/10.13039/501100001665), and the "Occitanie Region" and European Union H2020 Program (PROMIS ITN European Network Grant Agreement No. 641899, Funder Id: http://dx.doi.org/10.13039/501100007601).

References

[1] Boltasseva A, Atwater HA. Low-loss plasmonic metamaterials. Science 2011;331:290–1.
[2] Tonouchi M. Cutting-edge terahertz technology. Nat Photonics 2007;1:97.
[3] Soref R. Mid-infrared photonics in silicon and germanium. Nat Photonics 2010;4:495–7.
[4] Akyildiz IF, Jornet JM, Han C. Terahertz band: next frontier for wireless communications. Phys Commun 2014;12:16–32.
[5] Neubrech F, Huck C, Weber K, Pucci A, Giessen H. Surface-enhanced infrared spectroscopy using resonant nanoantennas. Chem Rev 2017;117:5110–45.
[6] Collin S, Vincent G, Haïdar R, Bardou N, Rommeluere S, Pelouard JL. Nearly perfect Fano transmission resonances through nanoslits drilled in a metallic membrane. Phys Rev Lett 2010;104:27401.
[7] Mittleman DM. Twenty years of terahertz imaging. Opt Express 2018;26:9417.
[8] Watts CM, Shrekenhamer D, Montoya J, et al. Terahertz compressive imaging with metamaterial spatial light modulators. Nat Photonics 2014;8:605.
[9] Gagnon MA, Jahjah KA, Marcotte F, Tremblay P, Farley V, Chamberland M. Time-resolved thermal infrared multispectral imaging of gases and minerals. In: Proceedings Multi-, Hyper-, Ultraspectral Remote Sens Tech Tech Appl V 2014;9263:92630G.
[10] Agarwal A, Vitiello MS, Viti L, Cupolillo A, Politano A. Plasmonics with two-dimensional semiconductors: from basic research to technological applications. Nanoscale 2018;10:8938.
[11] Constant TJ, Hornett SM, Chang DE, Hendry E. All-optical generation of surface plasmons in graphene. Nat Phys 2016;12:124–8.
[12] Avouris P. Graphene photonics, plasmonics, and optoelectronics. IEEE J Sel Top Quantum Electron 2014;20:6000112.
[13] Kim J, Son H, Cho DJ, et al. Electrical control of optical plasmon resonance with graphene. Nano Lett 2012;12:5598–602.
[14] Li Y, Yan H, Farmer DB, et al. Graphene plasmon enhanced vibrational sensing of surface-adsorbed layers. Nano Lett 2014;14:1573–7.
[15] Low T, Avouris P. Graphene plasmonics for terahertz to mid-infrared applications. ACS Nano 2014;8:1086.
[16] Bao Q, Loh KP. Graphene photonics, plasmonics, and broadband optoelectronic devices. ACS Nano 2012;6:3677–94.
[17] Chen J, Badioli M, Alonso-González P, et al. Optical nano-imaging of gate-tunable graphene plasmons. Nature 2012;487:77–81.
[18] Fei Z, Rodin AS, Andreev GO, et al. Gate-tuning of graphene plasmons revealed by infrared nano-imaging. Nature 2012;487:82–5.
[19] Grigorenko AN, Polini M, Novoselov KS. Graphene plasmonics. Nat Photonics 2012;6:749–58.
[20] Tervo EJ, Boyuk DS, Cola BA, Zhang ZM, Filler MA. Sub-diffractional waveguiding by mid-infrared plasmonic resonators in semiconductor nanowires. Nanoscale 2018;10:5708.
[21] Agrawal A, Cho SH, Zandi O, Ghosh S, Johns RW, Milliron DJ. Localized surface plasmon resonance in semiconductor nanocrystals. Chem Rev 2018;118:3121–207.
[22] Kriegel I, Scotognella F. Tunable light filtering by a Bragg mirror/heavily doped semiconducting nanocrystal composite. Beilstein J Nanotechnol 2015;6:193–200.
[23] Kriegel I, Scotognella F, Manna L. Plasmonic doped semiconductor nanocrystals. Properties, fabrication, applications and perspectives. Phys Rep 2017;674:1–52.
[24] Chen Y, Francescato Y, Caldwell JD, et al. Spectral tuning of localized surface phonon polariton resonators for low-loss mid-IR applications. ACS Photonics 2014;1:718–24.
[25] Caldwell JD, Glembocki OJ, Francescato Y, et al. Low-loss, extreme subdiffraction photon confinement via silicon carbide localized surface phonon polariton resonators. Nano Lett 2013;13:3690–7.
[26] Vassant S, Marquier F, Greffet JJ, Pardo F, Pelouard JL. Tailoring GaAs THz radiative properties with surface phonons polaritons. Appl Phys Lett 2010;97:161101.
[27] Vassant S, Pardo F, Bouchon P, et al. Influence of a depletion layer on localized surface waves in doped semiconductor nanostructures. Appl Phys Lett 2012;100:091103.
[28] Takagi S, Kim SH, Yokoyama M, et al. High mobility CMOS technologies using III–V/Ge channels on Si platform. Solid State Electron 2013;88:2–8.
[29] Mimura T. The early history of the high electron mobility transistor (HEMT). IEEE Trans Microw Theory Tech 2002;50:780.
[30] Faist J, Capasso F, Sivco DL, Sirtori C, Hutchinson AL, Cho AY. Quantum cascade laser. Science 1994;264:553–6.
[31] Esaki L, Tsu, R. Superlattice and negative differential conductivity in semiconductors. IBM J Res Dev 1970;14:61–5.
[32] Manasevit HM. Single-crystal gallium arsenide on insulating substrates. Appl Phys Lett 1968;12:156.
[33] Glang R, Kippenham BW. Impurity introduction during epitaxial growth of silicon. IBM J Res Dev 1960;4:299.
[34] Rosenbad C, Deller HR, Graf T, Mὺller E, von Kȁnel H. Low temperature growth by LEPECVD. J Cryst Growth 1998;188:125–30.
[35] Frigerio J, Ballabio A, Isella G, et al. Tunability of the dielectric function of heavily doped germanium thin films for mid-infrared plasmonics. Phys Rev B 2016;94:085202.
[36] Arthur J R. Interaction of Ga and As2 molecular beams with GaAs surfaces. J Appl Phys 1968;39:4032.
[37] Cho AY, Arthur JR. Molecular beam epitaxy. Prog Solid State Chem 1975;10:157.
[38] Wei D, Harris C, Bomberger CC, Zhang J, Zide J, Law S. Single-material semiconductor hyperbolic metamaterials. Opt Express 2016;24:8735.
[39] Peragut F, Cerutti L, Baranov A, et al. Hyperbolic metamaterials and surface plasmon polaritons. Optica 2017;4:1409.
[40] Prucnal S, Liu F, Voelskow M, Vines L, et al. Ultra-doped n-type germanium thin films for sensing in the mid-infrared. Sci Rep 2016;6:27643.
[41] Frigerio J, Ballabio A, Gallacher K, et al. Optical properties of highly n-doped germanium obtained by in situ doping and laser annealing. J Appl Phys D Appl Phys 2017;50:465103.
[42] Rebohle L, Prucnal S, Skorupa W. A review of thermal processing in the subsecond range: semiconductors and beyond. Semicond Sci Technol 2016;31:103001.
[43] Lind AG, Aldridge HL, Bomberger CC, Hatem Ch, Zide JMO, Jones KS. Comparison of thermal annealing effects on electrical activation of MBE grown and ion implant Si-doped In0.53Ga0.47As. J Vac Sci Technol B 2015;33:021206.
[44] Okada Y, Sugaya T, Ohta S, Fujita T, Kawabe M. Atomic hydrogen-assisted GaAs molecular beam epitaxy. Jpn J Appl Phys 1995;34:238.
[45] Sarney WL, Svensson SP, Anderson EM, Lundquist AM, Pearson C, Millunchick JM. The influence of growth temperature on

Sb incorporation in InAsSb, and the temperature-dependent impact of Bi surfactants. J Cryst Growth 2014;406:8.
[46] Zhao H, Malko A, Lai ZH. Effect of bismuth on structural and electrical properties of InAs films grown on GaAs substrates by MBE. J Cryst Growth 2015;425:89.
[47] Xu C, Senaratne CL, Kouvetakis J, Menéndez J. Experimental doping dependence of the lattice parameter in n-type Ge: identifying the correct theoretical framework by comparison with Si. Phys Rev B 2016;93:041201R.
[48] Xu C, Kouvetakis J, Menéndez J. Doping dependence of the optical dielectric function in n-type germanium. J Appl Phys 2019;125:085704.
[49] Raymond A, Robert JL, Bernard C. The electron effective mass in heavily doped GaAs. J Phys C Solid State Phys 1979;12:2289.
[50] Li YB, Stradling RA, Knight T, et al. Infrared reflection and transmission of undoped and Si-doped InAs grown on GaAs by molecular beam epitaxy. Semicond Sci Technol 1993;8:101.
[51] Trumbore FA. Solid solubilities of impurity elements in germanium and silicon. Bell Syst Tech J 1960;39:205.
[52] Yudin B. Steady state solubility of substitutional impurities is silicon. Phys Stat Sol A 1987;101:123.
[53] Northrup JE, Zhang SB. Dopant and defect energetics: Si in GaAs. Phys Rev B 1993;47:6791.
[54] Wei SH. Overcoming the doping bottleneck in semiconductors. Comput Mater Sci 2004;30:337.
[55] Vanhellemont J, Simoen E. On the diffusion and activation of n-type dopants in Ge. Mater Sci Semicond Process 2012;15:642.
[56] Tokumitsu E. Correlation between Fermi level stabilization positions and maximum free carrier concentrations in III–V compound semiconductors. Jpn J Appl Phys 1990;29:L698.
[57] Cargill GS, Angilello J, Kavanagh KL. Lattice compression from conduction electrons in heavily doped Si:As. Phys Rev Lett 1988;61:1748.
[58] Zhu J, Liu F, Stringfellow GB, Wei SH. Strain-enhanced doping in semiconductors: effects of dopant size and charge state. Phys Rev Lett 2010;105:195503.
[59] Samarelli A, Frigerio J, Sakat E, et al. Fabrication of mid-infrared plasmonic antennas based on heavily doped germanium thin films. Thin Solid Films 2016;602:52–5.
[60] Baldassarre L, Sakat E, Frigerio J, et al. Midinfrared plasmon-enhanced spectroscopy with germanium antennas on silicon substrates. Nano Lett 2015;15:7225–31.
[61] Fischer MP, Schmidt C, Sakat E, et al. Optical activation of germanium plasmonic antennas in the mid-infrared. Phys Rev Lett 2016;117:047401.
[62] Law S, Adams DC, Taylor AM, Wasserman D. Mid-infrared designer metals. Opt Express 2012;20:12155.
[63] N'Tsame Guilengui V, Cerutti L, Rodriguez JB, Tournié E, Taliercio T. Localized surface plasmon resonances in highly doped semiconductors nanostructures. Appl Phys Lett 2012;101:161113.
[64] Taliercio T, N'Tsame Guilengui V, Cerutti L, et al. Fano-like resonances sustained by Si doped InAsSb plasmonic resonators integrated in GaSb matrix. Opt Express 2015;23:29423.
[65] Milla MJ, Barho F, González-Posada F, et al. Localized surface plasmon resonance frequency tuning in highly doped InAsSb/GaSb one-dimensional nanostructures. Nanotechnology 2016;27:425201.
[66] Fahed M, Desplanque L, Troadec D, Patriarche G, Wallart X. Selective area heteroepitaxy of GaSb on GaAs (001) for in-plane InAs nanowire achievement. Nanotechnology 2016;27:505301.
[67] Huang JS, Callegari V, Geisler P, et al. Atomically flat single-crystalline gold nanostructures for plasmonic nanocircuitry. Nat Commun 2010;1:150.
[68] Calandrini E, Venanzi T, Appugliese F, et al. Mapping the electromagnetic field confinement in the gap of germanium nanoantennas with plasma wavelength of 4.5 micrometers. Appl Phys Lett 2016;109:121104.
[69] Law S, Yu L, Rosenberg A, Wasserman D. All-semiconductor plasmonic nanoantennas for infrared sensing. Nano Lett 2013;13:4569–74.
[70] Rosenberg A, Surya J, Liu R, et al. Flat mid-infrared composite plasmonic materials using lateral doping-patterned semiconductors. J Opt 2014;16:094012.
[71] Salman J, Hafermann M, Rensberg J, et al. Flat optical and plasmonic devices using area-selective ion-beam doping of silicon. Adv Opt Mater 2018;6:1701027.
[72] Ginn JC, Jarecki RL, Shaner EA, Davids PS. Infrared plasmons on heavily-doped silicon. J Appl Phys 2011;110:043110.
[73] Augel L, Fischer IA, Hornung F, et al. Ellipsometric characterization of doped Ge0.95Sn0.05 films in the infrared range for plasmonic applications. Opt Lett 2016;41:4398–400.
[74] Jun YC, Reno J, Ribaudo T, et al. Epsilon-near-zero strong coupling in metamaterial-semiconductor hybrid structures. Nano Lett 2013;13:5391–6.
[75] Alam MZ, De Leon I, Boyd RW. Large optical nonlinearity of indium tin oxide in its epsilon-near-zero region. Science 2016;352:795–7.
[76] Liberal I, Engheta N. Near-zero refractive index photonics. Nat Photonics 2017;11:149–58.
[77] Pollard RJ, Murphy A, Hendren WR, et al. Optical nonlocalities and additional waves in epsilon-near-zero metamaterials. Phys Rev Lett 2009;102:127405.
[78] Maas R, Parsons J, Engheta N, Polman A. Experimental realization of an epsilon-near-zero metamaterial at visible wavelengths. Nat Photonics 2013;7:907–12.
[79] Suchowski H, O'Brien K, Wong ZJ, Salandrino A, Yn X, Zhang X. Phase mismatch-free nonlinear propagation in optical zero-index materials. Science 2013;342:1223–6.
[80] Maier S. Plasmonics, fundamentals and applications. LaVergne, TN, USA, Springer, 2007.
[81] Agio M, Alù A. Optical antennas. Cambridge, UK, Cambridge University Press, 2012.
[82] Novotny L, van Hulst N. Antennas for light. Nat Photonics 2011;5:83–90.
[83] Biagioni P, Huang JS, Hecht B. Nanoantennas for visible and infrared radiation. Rep Prog Phys 2012;75:024402.
[84] Hsieh WT, Wu PC, Khurgin JB, Tsai DP, Liu N, Sun G. Comparative analysis of metals and alternative infrared plasmonic materials. ACS Photonics 2018;5:2541–8.
[85] Miller OD, Hsu CW, Reid MTH, et al. Fundamental limits to extinction by metallic nanoparticles. Phys Rev Lett 2014;112:123903.
[86] Miller OD, Polimeridis AG, Reid MTH, et al. Fundamental limits to optical response in absorptive systems. Opt Express 2016;24:3329.
[87] Gordon R, Ahmed A. Reaching the limits of enhancement in (sub)nanometer metal structures. ACS Photonics 2018;5:4222–8.

[88] Gordon R. Nanostructured metals for light-based technologies. Nanotechnology 2019;30:212001.
[89] Khurgin JB, Boltasseva A. Reflecting upon the losses in plasmonics and metamaterials. MRS Bull 2012;37:768–79.
[90] Dastmalchi B, Tassin P, Koschny T, Soukoulis CM. A new perspective on plasmonics, confinement and propagation length of surface plasmons for different materials and geometries. Adv Opt Mater 2015;4:177–84.
[91] Pellegrini G, Baldassarre L, Giliberti V, et al. Benchmarking the use of heavily-doped Ge against noble metals for plasmonics and sensing in the mid-infrared. ACS Photonics 2018;5:3601–7.
[92] Taliercio T, N'Tsame Guilengui V, Cerutti L, Tournié E, Greffet JJ. Brewster "mode" in highly doped semiconductor layers, an all-optical technique to monitor doping concentration. Opt Express 2014;22:24294.
[93] Calandrini E, Ortolani M, Nucara A, et al. Determination of the free carrier concentration in atomic-layer doped germanium thin films by infrared spectroscopy. J Opt 2014;16:094010.
[94] Boardman AD. Electromagnetic surface modes. Northern Ireland: University Press (Belfast), Wiley, 1982.
[95] Burstein E, Chen WP, Chen YJ, Hartstein A. Surface polaritons – propagating electromagnetic modes at interfaces. J Vac Sci Technol 1974;11:1004.
[96] Ferrell RA. Predicted radiation of plasma oscillations in metal films. Phys Rev 1958;111:1214–22.
[97] Steinmann W. Experimental verification of radiation of plasma oscillations in thin silver films. Phys Rev Lett 1960;5:470–2.
[98] McAlister AJ, Stern EA. Plasma resonance absorption in thin metal films. Phys Rev 1963;132:1599.
[99] Berreman DW. Infrared absorption at longitudinal optic frequency in cubic crystal films. Phys Rev 1963;130:2193–8.
[100] Campione S, Kim I, De Ceglia D, Keeler GA, Luk TS. Experimental verification of epsilon-near-zero plasmon polariton modes in degenerately doped semiconductor nanolayers. Opt Express 2016;24:18782.
[101] Stockman MI, Kneipp K, Bozhevolnyi SI. Roadmap on plasmonics. J Opt 2018;20:043001.
[102] Gallinet B, Butet J, Martin OJF. Numerical methods for nanophotonics, standard problems and future challenges. Laser Photonics Rev 2015;9:577–603.
[103] Mie G. Beiträge zur Optik trüber Medien, speziell kolloidaler Metallösungen. Ann Phys 1908;330:377–445.
[104] Moharam MG, Gaylord TK. Rigorous coupled-wave analysis of planar-grating diffraction. J Opt Soc Am 1981;71:811–8.
[105] Lumerical, Inc. Available at: http://www.lumerical.com/tcad-products/fdtd/. Accessed: August 2018.
[106] COMSOL Multiphysics® version 5.2. COMSOL AB, Stockholm, Sweden. Available at: http://www.comsol.com. Accessed: August 2018.
[107] Hugonin JP, Lalanne P. RETICOLO. Available at: https://www.lp2n.institutoptique.fr/content/download/5968/36955/file/RETICOLO%20documentation.pdf. Accessed: October 15, 2018.
[108] Meep (MIT Electromagnetic Equation Propagation). Available at: https://meep.readthedocs.io/en/latest/. Accessed: August 2018.
[109] CAMFR (Cavity Modelling Framework). Available at: http://camfr.sourceforge.net/. Accessed: August 2018.
[110] Montgomery JM, Lee TW, Gray SK. Theory and modeling of light interactions with metallic nanostructures. J Phys Condens Matter 2008;20:323201.
[111] Busch K, König M, Niegemann J. Discontinuous Galerkin methods in nanophotonics. Laser Photonics Rev 2011;5:773–809.
[112] Martin OJF, Piller NB. Electromagnetic scattering in polarizable backgrounds. Phys Rev E 1998;58:3909.
[113] Draine BT, Flatau PJ. Discrete-dipole approximation for scattering calculations. J Opt Soc Am A 1994;11:1491.
[114] Vandenbosch GAE, Volski V, Verellen N, Moshchalkov VV. On the use of the method of moments in plasmonic applications. Radio Sci 2011;46:RS0E02.
[115] Garcia de Abajo FJ, Howie A. Retarded field calculation of electron energy loss in inhomogeneous dielectrics. Phys Rev B 2002;65:115418.
[116] Kern AM, Martin OJF. Excitation and reemission of molecules near realistic plasmonic nanostructures. Nano Lett 2011;11:482–7.
[117] Mishchenko MI, Travis LD, Mackowski DW. T-matrix computations of light scattering by nonspherical particles, a review. J Quant Spectrosc Radiat Transfer 1996;55:535–75.
[118] Wriedt T, Eremin Y. The generalized multipole technique for light scattering. Springer Series on Atomic, Optical, and Plasma Physics. Switzerland, Springer Nature 2018.
[119] Moharam MG, Grann EB, Pommet DA, Gaylord TK. Formulation for stable and efficient implementation of the rigorous coupled-wave analysis of binary gratings. J Opt Soc Am A 1995;12:1068.
[120] Neikirk DP, Tong PP, Rutledge DB. Imaging antenna array at 119 μm. Appl Phys Lett 1982;41:329.
[121] Twu B, Schwarz SE. Properties of infrared cat-whisker antennas near 10.6 μm. Appl Phys Lett 1975;26:672.
[122] Grossman EN, Sauvageau JE, McDonald DG. Lithographic spiral antennas at short wavelengths. Appl Phys Lett 1991;59:3225–7.
[123] Fumeaux G, Boreman GD, Herrmann W, Rothuizen H, Kneubühl FK. Polarization response of asymmetric-spiral infrared antennas. Appl Opt 1997;36:6485–90.
[124] Fumeaux G, Boreman GD, Herrmann W, Kneubühl FK, Rothuizen H. Spatial impulse response of lithographic infrared antennas. Appl Opt 1999;38:37–46.
[125] Fumeaux C, Gritz MA, Codreanu I, Schaich WL, González FJ, Boreman GD. Measurement of the resonant lengths of infrared dipole antennas. Infrared Phys Technol 2000;41:271–81.
[126] Moreman GD, Fumeaux C, Herrmann W, Kneubühl FK, Rothuizen H. Tunable polarization response of a planar asymmetric-spiral infrared antenna. Opt Lett 1998;23:1912–4.
[127] Crozier KB, Sundaramurthy A, Kino GS, Quate CF. Optical antennas, resonators for local field enhancement. J Appl Phys 2003;94:4632–42.
[128] Mühlschlegel P, Eisler HJ, Martin OJF, Hecht B, Pohl DW. Resonant optical antennas. Science 2005;308:1607–9.
[129] Abb M, Wang Y, Papasimakis N, de Groot CH, Muskens. Surface-enhanced infrared spectroscopy using metal oxide plasmonic antenna arrays. Nano Lett 2014;14:346–52.
[130] Kuznetsov AS. Effect of proximity in arrays of plasmonic nanoantennas on hot spots density, degenerate semiconductors vs conventional metal. Plasmonics 2016;11:1487–93.
[131] Dorfmuller J, Vogelgesang R, Khunsin W, Rockstuhl C, Etrich C, Kern K. Plasmonic nanowire antennas, experiment, simulation, and theory. Nano Lett 2010;10:3596.
[132] Janke C, Gómez Rivas J, Schotsch C, Beckmann L, Haring Bolivar P, Kurz H. Optimization of enhanced terahertz transmis-

sion through arrays of subwavelength apertures. Phys Rev B 2004;69:205314.
[133] Gómez Rivas J, Sánchez-Gil JA, Kuttge M, Haring Bolivar P, Kurz H. Optically switchable mirrors for surface plasmon polaritons propagation on semiconductor surfaces. Phys Rev B 2006;74:245324.
[134] Gómez Rivas J, Kuttge M, Kurz H, Haring Bolivar P, Sánchez-Gil JA. Low-frequency active surface plasmon optics on semiconductors. Appl Phys Lett 2006;88:082106.
[135] Bomers M, Barho F, Milla-Rodrigo MJ, et al. Pedestal formation of all-semiconductor gratings through GaSb oxidation for mid-IR plasmonics. J Phys D Appl Phys 2018;51:015104.
[136] Huch C, Vogt J, Sendner M, Hengstler D, Neubrech F, Pucci A. Plasmonic enhancement of infrared vibrational signals, nanoslits versus nanorods. ACS Photonics 2015;2: 1489–97.
[137] Cetin AE, Etezadi D, Altug H. Accessible nearfields by nanoantennas on nanopedestals for ultrasensitive vibrational spectroscopy. Adv Opt Mater 2014;2:866–72.
[138] Barho FB, Gonzalez-Posada F, Milla MJ, et al. Highly doped semiconductor plasmonic nanoantenna arrays for polarization selective broadband surface-enhanced infrared absorption spectroscopy of vanillin. Nanophotonics 2018;7:507–16.
[139] Neubrech F, Kolb T, Lovrincic R, et al. Resonances of individual metal nanowires in the infrared. Appl Phys Lett 2006;89:253104.
[140] Neubrech F, Pucci A, Cornelius TW, Karim S, Garcıa-Etxarri A, Aizpurua J. Resonant plasmonic and vibrational coupling in a tailored nanoantenna for infrared detection. Phys Rev Lett 2008;101:157403.
[141] D'Andrea C, Bochterle J, Toma A, et al. Optical nanoantennas for multiband surface-enhanced infrared and Raman spectroscopy. ACS Nano 2013;7:3522–31.
[142] Svedendahl M, Käll M. Fano interference between localized plasmons and interface reflections. ACS Nano 2012;6:7533–9.
[143] Fischer MP, Riede A, Gallacher K, et al. Plasmonic mid-infrared third harmonic generation in germanium nanoantennas. Light: Science & Applications 2018,7:106.
[144] AlMothar A, Kazan M, Taliercio T, et al. Direct measurement of the effective infrared dielectric response of a highly doped semiconductor metamaterial. Nanotechnology 2017;28:125701.
[145] Taliercio T, N'Tsame Guilengui V, Cerutti L, Rodriguez JB, Tournié E. All-semiconductor plasmonics for mid-IR applications. Proc SPIE, Nanophotonics Materials X 2013; 8807-01.
[146] Guo P, Schaller RD, Ketterson JB, Chang PH. Ultrafast switching of tunable infrared plasmons in indium tin oxide nanorod arrays with large absolute amplitude. Nat Photonics 2016;10:267–74.
[147] Gómez Rivas J, Schotsch C, Haring Bolivar P, Kurz H. Enhanced transmission of THz radiation through subwavelength holes. Phys Rev B 2003;68:201306(R).
[148] Mayer B, Schmidt C, Bühler J, et al. Sub-cycle slicing of phase-locked and intense midinfrared transients. N J Phys 2014;16:063033.
[149] Schnell M, García-Etxarri A, Huber AJ, Crozier K, Aizpurua J, Hillenbrand R. Controlling the near-field oscillations of loaded plasmonic nanoantennas. Nat Photonics 2009;3:287–91.
[150] Schnell M, García-Etxarri A, Alkorta J, Aizpurua J, Hillenbrand R. Phase-resolved mapping of the near-field vector polarization state in nanoscale antenna gaps. Nano Lett 2010;10:3524–8.
[151] Dorfmüller J, Vogelgesang R, Weitz RT, et al. Fabry-Pérot resonances in one-dimensional plasmonic nanostructures. Nano Lett 2009;9:2372–7.
[152] Arcangeli A, Rossella F, Tomadin A, et al. Gate-tunable spatial modulation of localized plasmon resonances. Nano Lett 2016;16:5688–93.
[153] Huber AJ, Ziegler A, Köck T, Hillenbrand R. Infrared nanoscopy of strained semiconductors. Nat Nanotechnol 2009;4:153–57.
[154] Felts JR, Law S, Roberts CM, Podolskiy V, Wasserman DM, King WP. Near-field infrared absorption of plasmonic semiconductor microparticles studied using atomic force microscope infrared spectroscopy. Appl Phys Lett 2013;102:152110.
[155] Huang Y, Legrand D, Vincent R, et al. Spectroscopic nanoimaging of all-semiconductor plasmonic gratings using photoinduced force and scattering type nanoscopy. ACS Photonics 2018;5:4352–9.
[156] Huth F, Chuvilin A, Schnell M, et al. Resonant antenna probes for tip-enhanced infrared near-field microscopy. Nano Lett 2013;13:1065.
[157] Sakat E, Giliberti V, Bollani M, et al. Near-field imaging of free carriers in ZnO nanowires with a scanning probe tip made of heavily doped germanium. Phys Rev Appl 2017;8:054042.
[158] Naik GV, Alexandra Boltasseva A. A comparative study of semiconductor-based plasmonic metamaterials. Metamaterials 2011;5:1–7.
[159] Barho FB, Gonzalez-Posada F, Milla-Rodrigo MJ, Bomers M, Cerutti L, Taliercio T. All-semiconductor plasmonic gratings for biosensing applications in the mid-infrared spectral range. Opt Express 2016;24:16175–90.
[160] Johnson PB, Christy RW. Optical constants of the noble metals. Phys Rev B 1972;6:4370.
[161] Homola J, Piliarik M. Surface plasmon resonance (SPR) sensors. In: Surface Plasmon Resonance Based Sensors. Homola J, ed. Heidelberg: Springer, Berlin, 2006. Chapter 2.
[162] Svedendahl M, Chen S, Dmitriev A, K□ll M. Refractometric sensing using propagating versus localized surface plasmons, a direct comparison. Nano Lett 2009;9:4428–33.
[163] Luk'yanchuk B, Zheludev NI, Maier SA, et al. The Fano resonance in plasmonic nanostructures and metamaterials. Nat Mater 2010;9:707–15.
[164] Wu C, Khanikaev AB, Adato R, et al. Fano-resonant asymmetric metamaterials for ultrasensitive spectroscopy and identification of molecular monolayers. Nat Mater 2011;11;69.
[165] Fano U. Effects of configuration interaction on intensities and phase shifts. Phys Rev 1961;124:1866–78.
[166] Giannini V, Francescato Y, Amrania H, Phillips CC, Maier SA. Fano resonances in nanoscale plasmonic systems, a parameter-free modeling approach. Nano Lett 2011;11: 2835–40.
[167] GE Healthcare Life Sciences. Available at: https://proteins.gelifesciences.com/products-for-proteins/spr-systems/. Accessed: April 2018.
[168] LambdaGen Corporation. Available at: http://lamdagen.com/products/LSPR-biosensors/. Accessed: April 2018.

[169] Horiba Scientific. Available at: http://www.horiba.com/scientific/products/surface-plasmon-resonance-imaging-spri/. Accessed: April 2018.
[170] Gao Y, Xin Z, Zeng B, Gan Q, Chengc X, Bartoli FJ. Plasmonic interferometric sensor arrays for high performance label-free biomolecular detection. Lab Chip 2013;13:4755–64.
[171] Vincenti MA, Grande M, De Ceglia D, et al. Experimental demonstration of plasmonic-grating-assisted optical biosensor. In: Proc. SPIE Plasmonics, Metal Nanostr. & Optical Prop X, 2012:8457;84573T.
[172] Bog U, Huska K, Maerkle F, Nesterov-Mueller A, Lemmer U, Mappes T. Design of plasmonic grating structures towards optimum signal discrimination for biosensing applications. Opt Express 2012;20:11357–69.
[173] Cetin AE, Altug H. Fano resonant ring/disk plasmonic nanocavities on conducting substrates for advanced biosensing. ACS Nano 2012;6:9989–95.
[174] Sreekanth KV, Alapan Y, ElKabbash M, et al. Extreme sensitivity biosensing platform based on hyperbolic metamaterials. Nat Mater 2016;15:621.
[175] Sieger M, Mizaikoff B. Toward on-chip mid-infrared sensors. Anal Chem 2016;88:5562–73.
[176] Chen YB. Development of mid-infrared surface plasmon resonance-based sensors with highly-doped silicon for biomedical and chemical applications. Opt Express 2009;17:3130–40.
[177] DiPippo W, Lee BJ, Park K. Design analysis of doped-silicon surface plasmon resonance immunosensors in mid-infrared range. Opt Express 2010;18:19396–406.
[178] Ghosh S, Ray M. Performance analysis of semiconductor based surface plasmon resonance structures. Sens Actuators B Chem 2014;205:298–304.
[179] Ghosh S, Ray M. Analysis of silicon based surface plasmon resonance sensors with different amoni acids. Silicon 2015;7:313–22.
[180] Cleary JW, Medhi G, Peale RE, Buchwald WR, Edwards O, Oladeji I. Infrared surface plasmon resonance biosensor. Proc SPIE 2010;7673:767396.
[181] Sachet E, Losego MD, Guske J, Franzen S, Maria JP. Mid-infrared surface plasmon resonance in zinc oxide semiconductor thin films. Appl Phys Lett 2013;102:051111.
[182] Hartstein A, Kirtley JR, Tsang JC. Enhancement of the infrared absorption from molecular monolayers with thin metal overlayers. Phys Rev Lett 1980;45:201–4.
[183] Novotny L. Strong coupling, energy splitting, and level crossings. A classical perspective. Am J Phys 2010;78: 1199–202.
[184] Adato R, Artar A, Erramilli S, Altug H. Engineered absorption enhancement and induced transparency in coupled molecular and plasmonic resonator systems. Nano Lett 2013;13:2584.
[185] Fan S, Suh W, Joannopoulos JD. Temporal coupled-mode theory for the Fano resonance in optical resonators. J Opt Soc Am A 2003;20:569–72.
[186] Verslegers L, Yu Z, Ruan Z, Catrysse PB, Fan S. From electromagnetically induced transparency to superscattering with a single structure, a coupled-mode theory for doubly resonant structures. Phys Rev Lett 2012;108:083902.
[187] Neuman T, Huck C, Vogt J, et al. Importance of plasmonic scattering for an optimal enhancement of vibrational absorption in SEIRA with linear metallic antennas. J Phys Chem C 2015;119:26652.
[188] Neubrech F, Beck S, Glaser T, Hentschel M, Giessen H, Pucci A. Spatial extent of plasmonic enhancement of vibrational signals in the infrared. ACS Nano 2014;8:6250.
[189] Adato R, Yanik AA, Amsden JJ, et al. Ultra-sensitive vibrational spectroscopy of protein monolayers with plasmonic nanoantenna arrays. Proc Natl Acad Sci U.S.A. 2009;106:19227–32.
[190] Pucci A, Neubrech F, Weber D, Hong S, Toury T, Lamy de la Chapelle M. Surface enhanced infrared spectroscopy using gold nanoantennas. Phys Stat Sol B 2010;247:2071–4.
[191] Neubrech F, Weber D, Katzmann J, et al. Infrared optical properties of nanoantenna dimers with photochemically narrowed gaps in the 5 nm regime. ACS Nano 2012;6:7326–32.
[192] Brown LV, Zhao K, King N, Sobhani H, Nordlander P, Halas NJ. Surface-enhanced infrared absorption using individual cross antennas tailored to chemical moieties. J Am Chem Soc 2013;135:3688–95.
[193] Vogt J, Huck C, Neubrech F, Toma A, Gerbert D, Pucci A. Impact of the plasmonic near- and far-field resonance-energy shift on the enhancement of infrared vibrational signals. Phys Chem Chem Phys 2015;17:21169.
[194] Zuloaga J, Nordlander P. On the energy shift between near-field and far-field peak intensities in localized plasmon systems. Nano Lett 2011;11:1280.
[195] Brown LV, Yang X, Zhao K, Zheng BY, Nordlander P, Halas NJ. Fan-shaped gold nanoantennas above reflective substrates for surface-enhanced infrared absorption (SEIRA). Nano Lett 2015;15:1272–80.
[196] Dong L, Yang X, Zhang C, et al. Nanogapped Au antennas for ultrasensitive surface enhanced infrared absorption spectroscopy. Nano Lett 2017;17:5768–74.
[197] Huck C, Toma A, Neubrech F, et al. Gold nanoantennas on a pedestal for plasmonic enhancement in the infrared. ACS Photonics 2015;2:497.
[198] Liu HW, Lin FC, Lin SW, et al. Single-crystalline aluminum nanostructures on a semiconducting GaAs substrate for ultraviolet to near-infrared plasmonics. ACS Nano 2015;9:3875.
[199] Milla MJ, Barho F, González-Posada F, et al. Surface-enhanced infrared absorption with Si doped InAsSb/GaSb nano-antennas. Opt Express 2017;25:26651.
[200] Georgiou G, Tyagi HK, Bauhuis GJ, Schermer JJ, Gómez Rivas J. Photo-generated THz antennas. Sci Rep 2014;4:3584.
[201] Georgiou G, Tserzekis C, Schaafsma MC, Aizpurua J, Gómez Rivas J. Active loaded plasmonic antennas at terahertz frequencies, optical control of their capacitive-inductive coupling. Phys Rev B 2015;91:125443.
[202] Georgiou G, Shen NH, Gómez Rivas J, Koschny T, Soukoulis CM. Photoimprinted controllable Fano resonance in the terahertz regime. ACS Photonics 2017;4:1785–9.
[203] Yang Y, Kamaraju N, Campione S, et al. Transient GaAs plasmonic metasurfaces at terahertz frequencies. ACS Photonics 2017;4:15.
[204] Padilla WJ, Taylor AJ, Highstrete C, Lee M, Averitt RD. Dynamical electric and magnetic metamaterial response at terahertz frequencies. Phys Rev Lett 2006;96:107401.
[205] Chen HT, O'Hara JF, Azad AK, et al. Experimental demonstration of frequency-agile terahertz metamaterials. Nat Photonics 2008;2:295–8.

[206] Bühler J, Allerbeck J, Fitzky G, Brida D, Leitenstorfer A. Terahertz shockwaves generated by a precise subcycle cut of the electric field. Optica 2018;5:821–4.
[207] Chen HT, Padilla WJ, Zide JMO, Gossard AC, Taylor J, Averitt RD. Active terahertz metamaterial devices. Nature 2006;444: 597–600.
[208] Chen HT, Lu H, Azad AK, et al. Electronic control of extraordinary terahertz transmission through subwavelength metal hole arrays. Opt Express 2008;16:7641.
[209] Dyakonov MI, Shur MS. Shallow water analogy for a ballistic field effect transistor. New mechanism of plasma wave generation by dc current. Phys Rev Lett 1993;71:2465.
[210] Dyakonov MI, Shur MS. Plasma wave electronics, novel terahertz devices using two dimensional electron fluid. IEEE Trans Electron Devices 1996;43:380.
[211] Knap W, Deng Y, Rumyantsev S, Shur MS. Resonant detection of subterahertz and terahertz radiation by plasma waves in submicron field-effect transistors. Appl Phys Lett 2002;81:4637.
[212] Tsui DC, Gornik E, Logan RA. Far infrared emission from plasma oscillations of Si inversion layers. Solid State Commun 1980;35:875.
[213] Dyer GC, Aizin GR, Preu S, et al. Inducing an incipient terahertz finite plasmonic crystals in coupled two dimensional plasmonic cavities. Phys Rev Lett 2012;109:126803.
[214] Dyer GC, Aizin GR, Allen SJ, et al. Induced transparency by coupling of Tamm and defect states in tunable terahertz plasmonic crystals. Nat Photonics 2013;7:925–30.
[215] Delteil A, Vasanelli A, Todorov Y, et al. Gate controlled coupling of intersubband plasmons. Appl Phys Lett 2013;102:031102.
[216] Woessner A, Lundeberg MB, Gao Y, et al. Highly confined low-loss plasmons in graphene-boron nitride heterostructures. Nat Mater 2015;14:421–5.
[217] Ni GX, McLeod AS, Sun Z, et al. Fundamental limits to graphene plasmonics. Nature 2018;557:530–3.
[218] Rodrigo D, Limaj O, Janner D, et al. Mid-infrared plasmonic biosensing with graphene. Science 2015;349:165.
[219] Alonso-González P, Nikitin AY, Gao Y, et al. Acoustic terahertz graphene plasmons revealed by photocurrent nanoscopy. Nat Nanotechnol 2017;12:31–5.
[220] Ni GX, WangL, Goldflam MD, et al. Ultrafast optical switching of infrared plasmon polaritons in high-mobility graphene. Nat Photonics 2016;10:244.
[221] Goossens S, Navickaite G, Monasterio C, et al. Broadband image sensor array based on graphene-CMOS integration. Nat Photonics 2017;11:366–71.
[222] Li D, Ning CZ. All-semiconductor active plasmonic system in mid-infrared wavelengths. Opt Express 2011;19:14594.
[223] Bhatnagar K, Caro MP, Rojas-Ramirez JS, et al. Integration of broken-gap heterojunction InAs/GaSb Esaki tunnel diodes on silicon. J Vac Sci Technol B 2015;33:062203.
[224] Larsen K, Austin D, Sandall IC, et al. Electrical modulation of the optical properties of mid-infrared metamaterials. Appl Phys Lett 2012;101:251109.
[225] Shaner EA, Cederberg JG, Wasserman D. Electrically tunable extraordinary optical transmission gratings. Appl Phys Lett 2007;91:181110.
[226] Wasserman D, Shanera EA, Cederberg JG. Midinfrared doping-tunable extraordinary transmission from sub-wavelength gratings. Appl Phys Lett 2007;90:191102.
[227] Passmore BS, Allen DG, Vangala SR, Goodhue WD, Wasserman D, Shaner EA. Mid-infrared doping tunable transmission through subwavelength metal hole arrays on InSb. Opt Express 2009;17:10223.
[228] Benz A, Montano I, Klem JF, Brener I. Tunable metamaterials based on voltage controlled strong coupling. Appl Phys Lett 2013;103:263116.
[229] Benz A, Campione S, Liu S, et al. Strong coupling in the sub-wavelength limit using metamaterial nanocavities. Nat Commun 2013;4:2882.
[230] Lee J, Jung S, Chen PY, et al. Ultrafast electrically tunable polaritonic metasurfaces. Adv Opt Mater 2014;2:1057.
[231] Dionne JA, Diest K, Sweatlock LA, Atwater HA. PlasMOStor, a metal-oxide-Si field effect plasmonic modulator. Nano Lett 2009;9:897–902.
[232] Prade B, Vinet JY. Guided optical waves in fibers with negative dielectric constant. J Lightwave Technol 1994;12:6–18.
[233] Novotny L, Hafner C. Light propagation in a cylindrical waveguide with a complex, metallic, dielectric function. Phys Rev E 1994;50:4094–106.
[234] Takahara J, Yamagishi S, Taki H, Morimoto A, Kobayashi T. Guiding of a one-dimensional optical beam with nanometer diameter. Opt Lett 1997;22:475–7.
[235] Stockman MI. Nanofocusing of optical energy in tapered plasmonic waveguides. Phys Rev Lett 2004;93:137404.
[236] Schnell M, Alonso-González P, Arzubiaga L, et al. Nanofocusing of mid-infrared energy with tapered transmission lines. Nat Photonics 2011;5:283–7.
[237] Schwarz B, Reininger P, Ristanić D, et al. Monolithically integrated mid-infrared lab-on-a-chip using plasmonics and quantum cascade structures. Nat Commun 2014;5:4085.
[238] Sirtori C, Kruck P, Barbieri S, et al. GaAs/AlxGa1-xAs quantum cascade lasers. Appl Phys Lett 1998;73:3486.
[239] Ohtani K, Fujita K, Ohno H. Room-temperature InAs/AlSb quantum-cascade laser operating at 8.9 μm. Electron Lett 2007;43:520–2.
[240] Teissier R, Barat D, Vicet A, et al. InAs/AlSb quantum cascade lasers operating at 6.7 μm. Electron Lett 2003;39:1252–4.
[241] Soref R, Hendrickson J, Cleary JW. Mid to long-wavelength IR plasmonic-photonics using heavily doped n-Ge/Ge and n-GeSn/GeSn heterostructures. Opt Express 2012;20:3814.
[242] Gamal R, Ismail Y. Silicon waveguides at the mid-infrared. J Lightwave Technol 2015;33:3207–14.
[243] Biagioni P, Frigerio J, Samarelli A, et al. Group-IV midinfrared plasmonics. J Nanophot 2015;9:093789.
[244] Zhu F, Li X, Shen L. Subwavelength guiding of channel plasmon polaritons in a semiconductor at terahertz frequencies. Appl Opt 2014;53:5896.
[245] Chang YC, Paeder V, Hvozdara L, Hartmann JM, Herzig HP. Low-loss germanium strip waveguides on silicon for the mid-infrared. Opt Lett 2012;37:2883–5.
[246] Ramirez JM, Liu Q, Vakarin V, et al. Graded SiGe waveguides with broadband lowloss propagation in the mid infrared. Opt Express 2018;26:870.
[247] Gallacher K, Millar RW, Griškevičiūtė U, et al. Low loss Ge-on-Si waveguides operating in the 8–14 micron atmospheric transmission window. Opt Express 2018;26:25667–75.
[248] Mu J, Soref R, Kimerling LC, Michel J. Silicon-on-nitride structures for mid-infrared gap-plasmon waveguiding. Appl Phys Lett 2014;104:031115.

[249] Zektzer R, Desiatov B, Mazurski N, Bozhevolnyi SI, Levy U. Experimental demonstration of CMOS-compatible long-range dielectric-loaded surface plasmon-polariton waveguides (LR-DLSPPWs). Opt Express 2014;22:22009.
[250] Aouani H, Navarro-Cia M, Rahmani M, et al. Multiresonant broadband optical antennas as efficient tunable nanosources of second harmonic light. Nano Lett 2012;12:4997–5002.
[251] Celebrano M, Wu X, Baselli M, Großmann S, et al. Mode matching in multiresonant plasmonic nanoantennas for enhanced second harmonic generation. Nat Nanotechnol 2015;10:412–7.
[252] Hentschel M, Utikal T, Giessen H, Lippitz M. Quantitative modeling of the third harmonic emission spectrum of plasmonic nanoantennas. Nano Lett 2012;12:3778–82.
[253] Danckwerts M, Novotny L. Optical frequency mixing at coupled gold nanoparticles. Phys Rev Lett 2007;98:026104.
[254] Kim S, Jin J, Kim YJ, Park IY, Kim Y, Kim SW. High-harmonic generation by resonant plasmon field enhancement. Nature 2008;453:757–60.
[255] Pfullmann N, Waltermann C, Noack M, et al. Bow-tie nano-antenna assisted generation of extreme ultraviolet radiation. N J Phys 2013;15:093027.
[256] Zhang J, Cassan E, Zhang XL. Efficient second harmonic generation from mid-infrared to near-infrared regions in silicon-organic hybrid plasmonic waveguides with small fabrication-error sensitivity and a large bandwidth. Opt Lett 2013;38:2089–91.
[257] Lee J, Tymchenko M, Argyropoulos C, et al. Giant nonlinear response from plasmonic metasurfaces coupled to intersubband transitions. Nature 2014;511:65–9.
[258] Hon NK, Soref R, Jalali B. The third-order nonlinear optical coefficients of Si, Ge, and Si1-xGex in the midwave and long-wave infrared. J Appl Phys 2011;110:11301.
[259] Silveirinha M, Engheta N. Tunneling of electromagnetic energy through subwavelength channels and bends using e-near-zero materials. Phys Rev Lett 2006;97:157403.
[260] Ziolkowski RW. Propagation in and scattering from a matched metamaterial having a zero index of refraction. Phys Rev E 2004;70:046608.
[261] Schwartz T, Hutchison JA, Genet C, Ebbesen TW. Reversible switching of ultrastrong light-molecule coupling. Phys Rev Lett 2011;106:196405.
[262] Vassant S, Archambault A, Marquier F, et al. Epsilon-near-zero mode for active optoelectronic devices. Phys Rev Lett 2012;109:237401.
[263] Pradhan AK, Mundle RM, Santiago K, et al. Extreme tunability in aluminum doped zinc oxide plasmonic materials for near-infrared applications. Sci Rep 2014;4:6415.
[264] Kinsey N, Devault C, Kim J, Ferrera M, Shalaev VM, Boltasseva A. Epsilon-near-zero Al-doped ZnO for ultrafast switching at telecom wavelengths. Optica 2015;2:617.
[265] Adams DC, Inampudi S, Ribaudo T, et al. Funneling light through a subwavelength aperture with epsilon-near-zero materials. Phys Rev Lett 2011;107:133901.
[266] Wang M, Pan N. Predictions of effective physical properties of complex multiphase materials. Mater Sci Eng R 2008;63:1–30.
[267] Hoffman AJ, Alekseyev L, Howard SS, et al. Negative refraction in semiconductor metamaterials. Nat Mater 2007;6:946–50.
[268] Leon J, Taliercio T. Large tunable photonic band gaps in nanostructured doped semiconductors. Phys Rev B 2010;82:195301.
[269] Pendry JB. Negative refraction makes a perfect lens. Phys Rev Lett 2000;85:3966–9.
[270] Melville DOS, Blaikie RJ, Wolf CR. Appl Phys Lett 2004;84:4403–5.
[271] Fehrenbacher M, Winnerl S, Schneider H, et al. Plasmonic superlensing in doped GaAs. Nano Lett 2015;15:1057–61.
[272] Li T, Khurgin JB. Hyperbolic metamaterials, beyond the effective medium theory. Optica 2016;3:1388–96.
[273] Moreau A, Ciracı C, Mock JJ, et al. Controlled-reflectance surfaces with film-coupled colloidal nanoantennas. Nature 2012;492:86.
[274] Law S, Roberts C, Kilpatrick T, et al. All-semiconductor negative-index plasmonic absorbers. Phys Rev Lett 2014;112:017401.
[275] Smaali R, Omeis F, Moreau A, Centeno E, Thierry Taliercio T. Miniaturizing optical antennas using hyperbolic metamaterial wires. Phys Rev B 2017;95:155306.
[276] Omeis F, Smaali R, Gonzalez-Posada F, Cerutti L, Taliercio T, Centeno E. Metal-insulator-metal antennas in the far-infrared range based on highly doped InAsSb. Appl Phys Lett 2017;111:121108.
[277] Wang S, Wang Y, Zhanga S, Zheng W. Mid-infrared broadband absorber of full semiconductor epi-layers. Phys Lett A 2017;381:1439–44.
[278] Smaali R, Omeis F, Moreau A, Taliercio T, Centeno E. A universal design to realize a tunable perfect absorber from infrared to microwaves. Sci Rep 2016;6:32589.
[279] Smaali R, Taliercio T, Centeno E. Photo-generated metasurfaces for resonant and high modulation of terahertz signals. Opt Lett 2016;41:3900.
[280] Gunter G, Anappara AA, Hees J, et al. Sub-cycle switch-on of ultrastrong light-matter interaction. Nature 2009;458:07838.
[281] Delteil A, Vasanelli A, Todorov Y, et al. Charge-induced coherence between intersubband plasmons in a quantum structure. Phys Rev Lett 2012;109:246808.
[282] Ando T, Fowler AB, Stern F. Rev Mod Phys 1982;54:437.
[283] Askenazi B, Vasanelli A, Delteil A, et al. Ultra-strong light-matter coupling for designer Reststrahlen band. N J Phys 2014;16:043029.
[284] Sarma R, Campione S, Goldflam M, et al. Low dissipation spectral filtering using a field-effect tunable III–V hybrid metasurface. Appl Phys Lett 2018;113:061108.
[285] Sarma R, Campione S, Goldflam M, et al. A metasurface optical modulator using voltage-controlled population of quantum well states. Appl Phys Lett 2018;113:201101.
[286] Huppert S, Vasanelli A, Laurent T, et al. Radiatively broadened incandescent sources. ACS Photonics 2015;2:1663.
[287] Laurent T, Todorov Y, Vasanelli A, et al. Superradiant emission from a collective excitation in a semiconductor. Phys Rev Lett 2015;115:187402.